COLD SINTERING OF LEAD-FREE FERROELECTRIC PEROVSKITES

Samir Salmanov

Doctoral Dissertation
Jožef Stefan International Postgraduate School
Ljubljana, Slovenia

Supervisor: Asst. Prof. Dr. Mojca Otoničar, Jožef Stefan Institute, Ljubljana, Slovenia
Co-Supervisor: Prof. Dr. Danjela Kuščer Hrovatin, Jožef Stefan Institute, Ljubljana, Slovenia

Evaluation Board:
Prof. Dr. Andraž Kocjan, Chair, Jožef Stefan Institute, Ljubljana, Slovenia
Prof. Dr. Srečo Davor Škapin, Member, Jožef Stefan Institute, Ljubljana, Slovenia
Prof. Dr. Jurij Koruza, Member, Institute for Chemistry and Technology of Materials, TU Graz, Austria

MEDNARODNA PODIPLOMSKA ŠOLA JOŽEFA STEFANA
JOŽEF STEFAN INTERNATIONAL POSTGRADUATE SCHOOL

Samir Salmanov

COLD SINTERING OF LEAD-FREE FERROELECTRIC PEROVSKITES

Doctoral Dissertation

HLADNO SINTRANJE FEROELEKTRIČNIH PEROVSKITOV BREZ VSEBNOSTI SVINCA

Doktorska disertacija

Supervisor: Asst. Prof. Dr. Mojca Otoničar

Co-Supervisor: Prof. Dr. Danjela Kuščer Hrovatin

Ljubljana, Slovenia, April 2025

Acknowledgments

This thesis would not have been completed and submitted without the invaluable assistance of my colleagues from the Electronic Ceramics Department (K5) of Jožef Stefan Institute.

I extend my deepest gratitude to Asst. Prof. Dr. Mojca Otoničar for her guidance, patience, and support throughout my PhD study. I am also immensely thankful to Prof. Dr. Danjela Kuščer Hrovatin for her critical evaluation of my work and insightful discussions on the obtained results. Their contributions were invaluable in the publication of papers.

I would also like to acknowledge Prof. Barbara Malič for providing me with the opportunity to work at the K5 department, and express my appreciation to the Slovenian Research and Innovation Agency for funding the PhD project. Special thanks go to Jena Cilenšek, Silvo Drnovšek, Brigita Kmet, and Maja Koblar for their invaluable assistance in the laboratory.

Last but not least, I am profoundly grateful to my family for their unwavering support throughout my PhD study and my life in Slovenia.

Abstract

Fabrication of electroceramics usually requires high sintering temperatures of 800 to 1400 °C, which can unintentionally lead to problems such as volatilization of species, formation of secondary phases and excessive grain growth. These problems can cause inhomogeneous microstructures, non-stoichiometric chemical compositions and limited material functionality. Therefore, there is a need to develop processes that significantly reduce sintering temperatures.

In this dissertation, I present a low-temperature sintering process, the Cold Sintering Process (CSP), which enables the processing of ferroelectric perovskite ceramics at temperatures as low as 300 °C. Uniaxial pressures of up to 650 MPa and the incorporation of liquid phase additives are used to improve sintering. The focus of this research is primarily on two ferroelectric ceramic systems, $BiFeO_3$-based (BFO) and $(K_{0.5}Na_{0.5})NbO_3$-based (KNN) ceramics, which are environmentally friendly alternatives to conventional lead-based ferroelectrics, but are difficult to produce as single-phase and with homogeneous microstructure using conventional sintering methods.

Initially, I explored cold sintering of the BFO and KNN materials with different liquid-phase components. The best results were obtained with a NaOH/KOH mixture in a 1:1 molar ratio dissolved in water, which led to the most uniform microstructure and improved materials properties. The results regarding the influence of NaOH/KOH ratio and the quantity of additives on the microstructure and properties of BFO-based material are described in detail in the first article of the thesis. The article suggests the optimal additive ratio and concentration, leading to high remanent polarization and strain responses to the electric field. The second article summarizes the effects of processing conditions such as pressure, temperature, additive's amount, and post-annealing on KNN-based ceramics properties. Under optimal CSP conditions, KNN exhibited a high relative density of up to 98%, although it required elevated pressure, which led to significant structural deformation.

Research of the two cold-sintered ceramics systems showed that the electrical conductivity of BFO was 100 times lower than that of its conventionally sintered counterpart, effectively reducing leakage currents — a common undesired effect with conventional BFO. It is noteworthy that the cold-sintered BFO did not require post-annealing, while KNN had to be post-annealed at 500 °C in an O_2 environment to reduce the electrical conductivity. Furthermore, CSP enabled to successfully mitigate excessive grain growth and porosity in KNN, eliminating a major limitation in obtaining dense ceramics with conventional sintering. Both, BFO and KNN exhibited remarkable dielectric breakdown strength, with above 200 kV/cm for BFO and up to 170 kV/cm for KNN, making both materials systems promising candidates for energy storage applications.

My last research part was on cold sintering of KNN-BFO multiferroic composites. These composites exploit the functional advantages of both phases by adopting a high dielectric constant of KNN and increased remanent polarization of BFO, overcoming the limitations of the individual phases. The results are summarized in the third published article of this thesis.

Povzetek

Izdelava elektrokeramike običajno zahteva visoke temperature sintranja, od 800 do 1400 °C, kar lahko nenamerno povzroči težave, kot so hlapnost elementov, tvorba sekundarnih faz in prekomerna rast zrn. Te težave lahko povzročijo nehomogeno mikrostrukturo, nestohiometrično matrično sestavo in omejeno funkcionalnost materiala. Zato je potrebno razviti tehnologije, ki bistveno znižajo temperaturo sintranja in hkrati prispevajo k znižanju porabe energije.

V tej disertaciji obravnavam nov proces sintranja pri nizkih temperaturah, t. i. postopek hladnega sintranja (CSP), ki omogoča obdelavo feroelektrične perovskitne keramike. Postopek poteka pri temperaturah pod 300 °C, ob uporabi enoosnega tlaka do ~650 MPa in z vključevanjem aditivov v tekoči fazi za omogočanje sintranja. Osredotočil sem se na sintranje dveh feroelektričnih sestav, keramiko na osnovi $BiFeO_3$ (BFO) in keramiko na osnovi $(K_{0.5}Na_{0.5})NbO_3$ (KNN), ki sta okolju prijazni alternativi vsesplošno uporabljenim feroelektrikom na osnovi svinca. Keramiki sta sicer težavni za pripravo s konvencionalnim visokotemperaturnim sintranjem, saj pogosto izkazujeta neželeno večfazno sestavo in nehomogeno mikrostrukturo.

Sprva sem raziskoval hladno sintranje materialov BFO in KNN z dodatkom različnih komponent v tekoči fazi. Najboljši rezultati so bili doseženi z mešanico NaOH/KOH v molskem razmerju 1:1, raztopljeno v vodi, kar je pripeljalo do najbolj homogene mikrostrukture in izboljšanih lastnosti materialov. Rezultati glede vpliva razmerja NaOH/KOH in količine aditiva na mikrostrukturo in lastnosti materiala na osnovi BFO so podrobno opisani v prvem članku disertacije. Članek predlaga optimalno razmerje in koncentracijo aditiva, kar vodi do visoke remanentne polarizacije pod vplivom zunanjega električnega polja. Drugi članek povzema učinke pogojev hladnega sintranja, kot so tlak, temperatura, količina aditiva in kasnejše žganje na lastnosti keramike na osnovi KNN. Pod optimalnimi pogoji CSP, predvsem povišanega tlaka sintranja, KNN izkazuje visoko relativno gostoto keramike (do 98 %), kar pa sicer povzroči precejšnjo strukturno deformacijo keramike.

Raziskava obeh sistemov hladno sintranih keramik je pokazala, da je električna prevodnost BFO 100-krat nižja od tiste pri konvencionalno sintranem materialu, kar učinkovito zmanjša dielektrične izgube, ki so pogost neželen učinek pri konvencionalno sintranem BFO. Pomembno je, da hladno sintran BFO ne potrebuje kasnejšega žganja pri povišani temperaturi, medtem ko mora biti KNN dodatno žgan pri 500 °C v kisikovi atmosferi za znižanje električne prevodnosti. Poleg tega CSP omogoči uspešno zmanjšanje velikosti zrn in poroznosti pri KNN, ki predstavljata glavni problem klasičnega sintranja KNN keramike. Tako BFO kot KNN sta pokazala izjemno dielektrično prebojno trdnost, višjo od 200 kV/cm za BFO in do 170 kV/cm za KNN, zaradi česar sta obe hladno sintrani keramiki obetavni za uporabo v shranjevanju električne energije.

Moj zadnji del raziskav je obravnaval hladno sintranje večfaznih feroelektričnih kompozitov na osnovi KNN in BFO keramik. Tak kompozit izkorišča prednosti funkcijskih lastnosti obeh faz, torej visoke dielektrične konstante KNN in višje remanentne polarizacije

BFO, kar omogoča premagovanje omejitev posameznih faz. Rezultati so povzeti v tretjem objavljenem članku te disertacije.

Contents

List of Figures

Abbreviations

BFO	. . .	bismuth ferrite, $BiFeO_3$
BFOCo	. . .	Co-doped bismuth ferrite
BT	. . .	$BaTiO_3$
CSP	. . .	cold sintering process
DW	. . .	domain wall
EDS	. . .	energy-dispersive X-ray spectroscopy
FTIR	. . .	Fourier-transform infrared spectroscopy
IFFT	. . .	inverse fast Fourier transform
KNN	. . .	potassium sodium niobate, $K_{0.5}Na_{0.5}NbO_3$
KNNSr	. . .	Sr-doped potassium sodium niobate
LPS	. . .	liquid phase sintering
NBT	. . .	$Na_{0.5}Bi_{0.5}TiO_3$
P-E loop	. . .	polarization vs. electric field hysteresis loop
PMN-PT	. . .	$(1\text{-}x)Pb(Mg_{1/3}Nb_{2/3})O_3\text{-}xPbTiO_3$
PT	. . .	lead titanate
PZT	. . .	lead zirconate titanate
SEM	. . .	scanning electron microscope
S-E loop	. . .	strain vs. electric field hysteresis loop
SPS	. . .	spark plasma sintering
STEM	. . .	scanning transmission electron microscopy
TEM	. . .	transmission electron microscopy
TLP	. . .	transient liquid phase
XRD	. . .	X-ray powder diffraction

Symbols

d_{33} . . . direct longitudinal piezoelectric coefficient
d_{50} . . . 50$^{\text{th}}$ percentile of the particle size limit
E_C . . . coercive field
P_r . . . remanent polarization
P_S . . . spontaneous polarization
E_d . . . depolarizing field
S . . . strain
$tan\delta$ . . . dielectric losses
T_c . . . Curie temperature
T . . . temperature
T_{room} . . . room temperature
ΔT . . . temperature change
U_{loss} . . . energy-loss density
U_{rec} . . . recoverable energy density
$V_O^{\bullet\bullet}$ . . . oxygen vacancy
η . . . energy-storage efficiency
ε_r . . . relative dielectric constant

Chapter 1

Introduction

In the introduction of this thesis, the conventional sintering processes for ferroelectric perovskite ceramic materials are presented, with a focus on the effects of different processing approaches on the microstructure and properties of the materials. Attention is given to the sintering of lead-free ferroelectric ceramics, potassium sodium niobate (KNN) and bismuth ferrite (BFO). Finally, the cold sintering process (CSP) is described and critically evaluated, emphasizing the mechanisms of the process during consolidation and the success of its implementation to the sintering of oxides.

1.1 Introduction to Ferroelectric Ceramics

In recent decades, humanity has experienced rapid progress of high technologies in various industries. This progress requires the development of specialized electronic devices, e.g., sensors, memory devices, transducers, actuators, that empower us to leverage the diverse functionalities of materials in our everyday lives. To manufacture such devices, materials with specific properties, such as ferroelectric properties, are required [1].

In the past, solid ceramic materials (like pottery) were produced by heating the green bodies at elevated temperatures. The early development of furnaces was aimed at achieving higher firing temperatures for better materials densities. Still today, most ferroelectric ceramics are processed at high temperatures ranging from 800 to 1400 °C, depending on the material composition, requiring high energy consumption. Consequently, researchers have been exploring approaches to reduce energy consumption during processing while at the same time maintaining the desired functional responses of materials, in particular for those materials that fail to be sintered at high temperatures [2]. Other sources of energy input, for example, high pressure (as in hot-press sintering method), electricity (in flash sintering) or microwaves (in microwave sintering) have been employed to shorten the duration or decrease the temperature of sintering. In the last five years, low-temperature sintering techniques have been developed, for example the room temperature fabrication (RTF) method [3] or the cold sintering process (CSP). These methods attract attention as approaches to significantly decrease the sintering temperature and thus reduce energy consumption. Figure 1 illustrates the progression of sintering methods over time, from paleolithic to date.

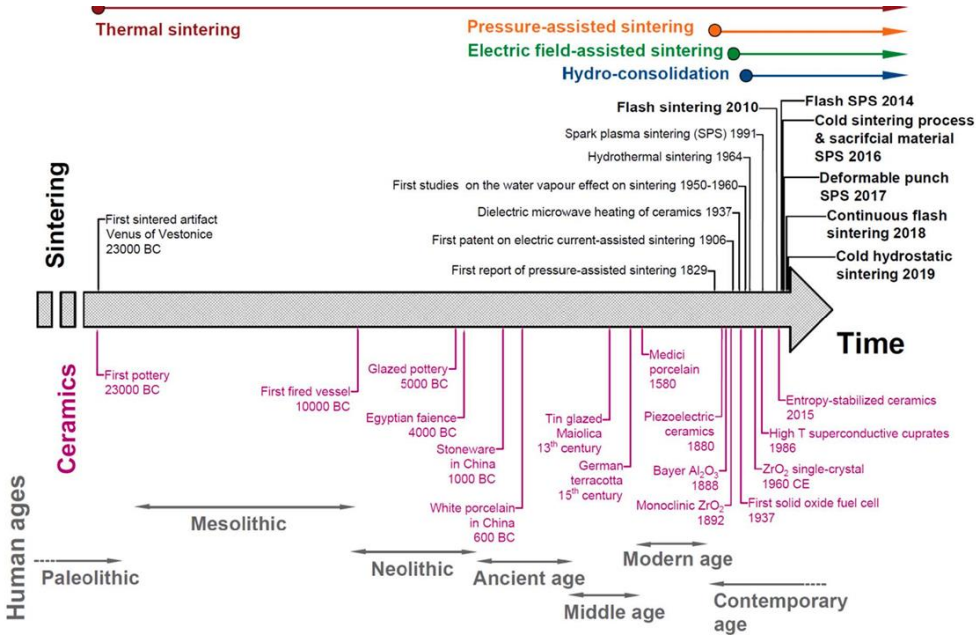

Figure 1: The history of processing ceramics from paleolithic to date. Reprinted from [2] with permission from Elsevier.

1.1.1 Basics of ferroelectricity

Ferroelectric properties are associated with the ability to switch the direction of spontaneous polarization by applying an electric field. The spontaneous polarization of oxides is strongly linked to the crystal lattice and symmetry of the materials, and depends on their chemical composition. Ferroelectric properties are also found in organic materials (e.g., PVDF-TrFE), where they are connected to the structure of molecules. However, this dissertation focuses on electroceramic materials, specifically oxides with perovskite structures formulated as ABO_3.

Among different electroceramic materials, the lead containing compositions, i.e., $Pb(Zr_xTi_{1-x})O_3$ (PZT) or $(1-x)Pb(Mg_{1/3}Nb_{2/3})O_3$-$xPbTiO_3$ (PMN-PT) have been widely used due to their good performances, relatively simple synthesis and attractive cost of production. On the other hand, mining of lead-containing raw minerals from ores and their usage in material production up to the incorporation into a device is harmful to the environment and the human body. Therefore, regulations and legislations from the European Commission dictate elimination of lead in production. This forced researchers to find lead-free alternatives, also in the field of electroceramics, such as $K_{0.5}Na_{0.5}NbO_3$ (KNN), $Na_{0.5}Bi_{0.5}TiO_3$ (NBT), $BaTiO_3$ (BT) and $BiFeO_3$ (BFO) perovskite materials [4], [5].

The primary characteristic of the ferroelectric perovskite structure is its noncentrosymmetric nature, which is a result of displacement of cations from their centrosymmetric position inside its oxygen cage, inducing a dipole (Figure 2) [6]. This results in spontaneous polarization (P_S). The temperature at which the structure transitions from centrosymmetric to noncentrosymmetric, or, in other words, from paraelectric to ferroelectric, is referred to as the Curie temperature, denoted as T_c. At T_c, the dielectric permittivity reaches its peak value and then begins to decrease, following the Curie–Weiss law [7]. Some materials, such as $BaTiO_3$, can undergo several phase transitions to lower symmetry phases below T_c, resulting in multiple peaks in dielectric properties.

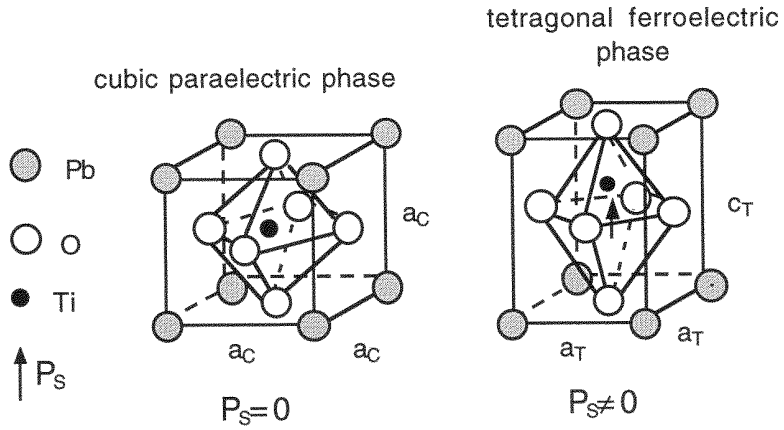

Figure 2: Cubic and tetragonal structures of $PbTiO_3$. Reproduced with permission from [6] from © IOP Publishing. All rights reserved.

The displacements of atoms from their centrosymmetric position are coupled with lattice distortion and strain, causing shrinkage and expansion of the crystal lattice in the symmetry-defined directions. The coupling of strain and polarization in response to applied external electric or mechanical field is termed the piezoelectric effect. Changes in polarization are also coupled with temperature properties, leading to the release/absorption of heat and altering the temperature of the material upon applied electric field (pyroelectric/electrocaloric property). The coupling of electrical, mechanical and thermal properties enables the use of piezoelectric materials in diverse fields of energy conversion.

When processing ferroelectric ceramics, it is important to design materials of desired composition and functionality. The latter largely depends on the symmetry of the perovskite structure in the operational temperature range, which strongly influences the domain structure, but also on the microstructure of the ceramics, i.e., the grain size and porosity. Ferroelectric domains are defined by a set of unit cells with uniformly oriented spontaneous polarization. Neighboring domains adopt a different orientation of spontaneous polarization (within the same symmetry) and are separated by domain walls (Figure 3), where the type of domains is defined by the angle between spontaneous dipoles from each domain, e.g., 180°, 90°, 71°, etc. Several domains merge into a grain where domain walls can be observed. Domains in polycrystalline materials form primarily due to the influence of internal strain of the lattice from spontaneous dipole formation when crossing the phase transition from a cubic to a non-cubic symmetry [6], and the fact that grains in ceramics are constrained by adjacent grains in the bulk, limiting their contraction/expansion with lattice distortion.

When an external electric field is applied to the ferroelectric material, the dipoles start to reorient and align with the field, followed by switching and movement of the domain walls, resulting in remanent polarization P_r when the field is removed.

Several factors influence the ease of dipoles switching and the domain wall movement, for example, the reduction/oxidation of atoms during the sintering process, the accumulation of stresses and the formation of dislocations, atomic substitutions, etc. This is particularly important when the ferroelectric material is prepared with dopants of different valence states [8], [9].

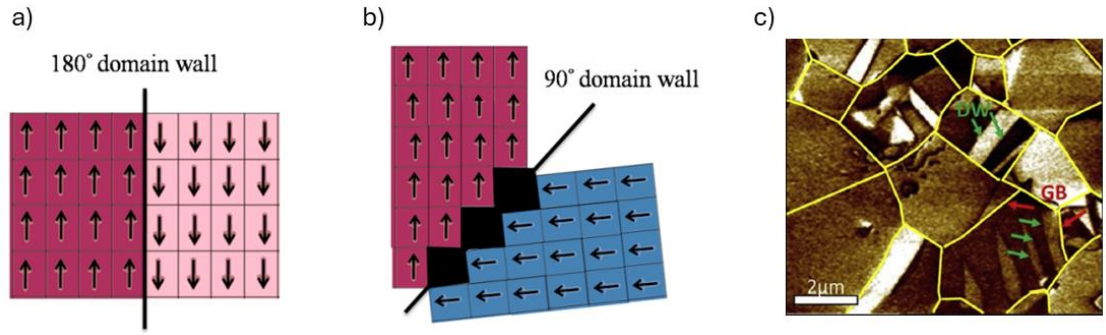

Figure 3: Schematics of a domain wall separating two domains with dipoles oriented at: a) 180°, b) 90° towards each other. Reproduced with permission from [10]. c) PFM image of polycrystalline ceramics with grains separated by yellow lines and domain walls marked by green arrows. Reprinted from [11] with permission from Elsevier.

1.2 Importance of Grain Sizes, Domain Walls and Defects

Domain structure in ferroelectrics depends primarily on the crystal symmetry, but there exists also an intimate relationship between domain structure and size and the grain size in polycrystalline ceramics [12]. The configuration of grains, domain walls, and defect morphology plays a crucial role in determining the functional properties of dense electroceramics. Various sintering approaches and techniques aim to influence the grain size and domain structure, potentially affecting the sintering mechanism and altering functional properties significantly.

1.2.1 Effect of grain/domain size on ferroelectric properties

The ferroelectric and piezoelectric properties of bulk electroceramics are influenced by both intrinsic and extrinsic effects. Intrinsic contribution to the electromechanical response relates to the lattice deformation as the external field is applied. This response dominates when the grain's surface area is large compared to the grain volume and the domains are not well developed. Extrinsic effects, on the other hand, are usually associated with domain wall or interface dynamics and prevail when the grain's surface to volume ratio is reduced [13]–[15]. Notably, the extrinsic effects (domain wall or phase-boundary motion) can contribute up to 60-70% of the total dielectric and piezoelectric properties of PZT and BT [16]–[18]. The extrinsic contributions to the electromechanical response can be limited by two main factors: the concentration of domains, which is directly related to the grain size, and the mobility of domain walls, which is influenced by domain structure complexity and defects that can pin the domain walls.

Small grains (< 1 μm; for BT it can reach ~ 40 nm [19]) may turn into a single domain [12], [19], [20]. *Ghosh et al.* showed that the domain wall motion of BT is significantly suppressed for ceramics with <0.3 μm grain size, while the ceramics with 2 μm grain sizes exhibits 90° domain switching, linked to its tetragonal symmetry at room temperature [21]. For nano-sized grains, no domain walls are observed, and consequently, there is no domain wall motion and only the intrinsic effects contribute to the electromechanical response.

Although ferroelectric properties are suppressed at the nanoscale, ferroelectricity can be induced by applying an external force. Nano-sized powders typically have a cubic structure, however, the surface of nano-powder particles (after milling) can stabilize the ferroelectric state and strains can form a tetragonally distorted layer as shown for $PTiO_3$ (PT) [22]. A similar strain-induced effect was observed for BT, where it was demonstrated

that powder with a size of 10 nm possesses a permanent dipole moment [23]. All of the above-mentioned ferroelectric properties in nano-sized grains are associated with accumulated stresses and space charges on the grain surfaces [22], [23]. If this stress is eliminated, for example, through post-annealing, without a significant change in grain size, the ferroelectric properties may disappear [24]. This can be explained by the cubic structure of nano-sized grains, where the critical grain size for switching from ferroelectric to non-ferroelectric behavior is between 5-15 nm [14], [25], [26]. Thus, the ferroelectric properties are linearly dependent on grain size: the smaller the grain size, the less ferroelectric the material is.

However, the dependence of dielectric permittivity on grain size is not linear (Figure 4). In particular, there is a noticeable increase in the permittivity of BT (Figure 4) with a grain size around 1 µm [27]–[29]. *Arlt et al.* explained this peak as due to an increase in the extrinsic contribution to the response, including a higher density of mobile 90° domain walls and an increased number of grain boundaries [30]. The steep decline of permittivity in the region < 1 µm is explained by the brick-wall theory, according to which the nano-sized grains have a core with a high value of permittivity (for example, in the case of BT it can reach ~4600) that is surrounded by the grain-boundary layer, which has a very low permittivity (in the case of BT it can reach ~130) [31], [32]. As a result, the total value of permittivity is decreased by the increased contribution of the grain-boundary effect.

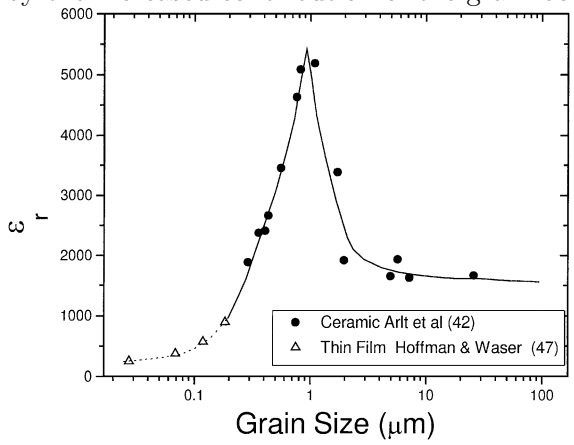

Figure 4: Impact of grain size of $BaTiO_3$ on the permittivity. Reprinted from [14] with permission from Annual Reviews.

The grain size effect is also important for T_c. It was shown that the T_c of BT nanowires with diameter ~ 10 nm was significantly dropped, to ~ 70 °C, while for bulk BT it is 120 °C [33]. Furthermore, the temperature range of the phase transition becomes broader by decreasing the grain size and the permittivity is suppressed [34].

1.2.2 Formation of defects and charge compensation through vacancies

An efficient technique for influencing the functional properties of ferroelectric materials is to add an element to the ferroelectric structure in low concentration, a dopant. Dopants are incorporated into the perovskite lattice, replacing atoms with different valence states and creating various defects, such as vacancies and defect dipoles. Depending on the valence state of the dopant that replaces a cation at a certain lattice position, the dopant can act as an acceptor or a donor of electrons. In the case of PZT, the doped materials are classified as soft (acceptor) or hard (donor). Softening of PZT is caused by replacing the Ti^{4+} or Zr^{4+} on B-site of the perovskite lattice by element with higher valence state, such as Nb^{5+}, while hardening is achieved by replacing Ti^{4+} or Zr^{4+} with lower-valence state element, such as

Fe^{3+}. The polarization-electric field (P-E) response of doped materials is significantly different compared to undoped materials. Soft PZT has a square-like open hysteresis loop with a high P_r and relatively low coercive field (E_c) (Figure 5) [35], while hard PZT shows a pinched and canted P-E loop with zero P_r. The latter is caused by the formation of defect dipoles segregated at the domain walls, acting as pinning centers and decreasing their mobility. As a result, the P_r in hard materials is significantly suppressed and the switching field, E_c, is increased.

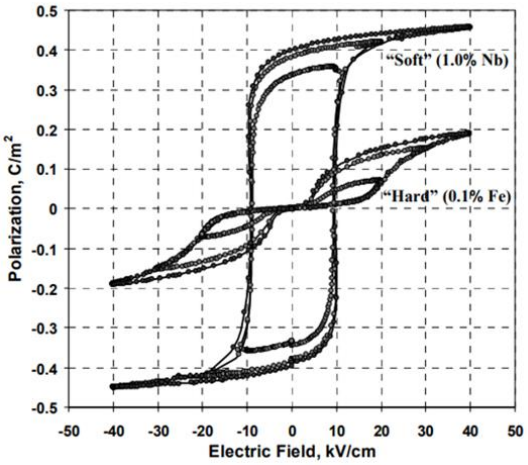

Figure 5: The influence of doping on hysteresis loops in PZT – softening vs. hardening of the ferroelectric response. Reprinted from [35] with permission.

Beside doping strategies, conditions of conventional sintering such as temperature, atmosphere (partial pressure) and time can also induce the formation of defects. Typically, these are vacancies that form due to reduced vapor pressure of oxygen surrounding the sample, and volatility of species, further causing changes in the valence state of atoms, which are charge-compensating defects. Furthermore, stresses associated with temperature-induced defects and lattice deformation can cause dislocations in the crystal structure.

Vacancies commonly exist in sintered materials and can present thermodynamically stable defects that increase disorder and thus the entropy of the system. Quite often, however, the formation of vacancies is linked to the evaporation of volatile species during sintering, most commonly involving the loss of oxygen atoms as O_2, depending on its the partial pressure surrounding the body. In some cases, oxygen atoms evaporate along with cations, leading to the volatilization of metal oxides. For example, during BFO sintering, Bi_2O_3 volatilization has been observed [11]. This volatilization further affects charge distribution in the crystal lattice, and may result in additional cation reduction. Such accumulation of positively and negatively charged vacancies, i.e., electrons and holes, can in some cases couple and create defect dipole pairs. For instance, BFO sintering in reducing (N_2) atmosphere can lead to segregation of Bi and O vacancies at domain walls and the formation of Fe^{2+} [11]. This further causes pinching of the P-E loop. Similarly, when BT is processed in O_2-deficient environments, oxygen vacancies form, and associated cation reductions occur (Ti^{3+}) to balance the positive charge of holes, creating defect dipoles [36].

Changes in the valence states of atoms directly affect dielectric and ferroelectric properties. It has been shown that bismuth and oxygen vacancies, as well as Fe^{4+}, accumulate at the domain walls, inducing high electrical conductivity [11], [37], [38]. In order to decrease conductivity, dopants can be used (for example, Ti^{4+}, Ca^{2+}) [39]–[42] or an oxygen-lean environment (N_2), to suppress the formation of Fe^{4+} [11], [37]. Therefore, electrical conductivity measured in insulating materials can serve as a sign of accumulated defect states. The formed defects in BFO can accumulate at the domain walls, and act as

pinning centers, preventing domain wall movement [11]. As a result, the measured P-E loop appears pinched (Figure 6), with suppressed remanent polarization (P_r). This can be mitigated by annealing BFO in oxygen-rich atmosphere.

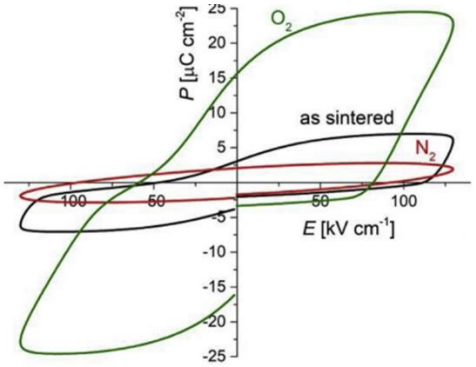

Figure 6: P-E loops of as-sintered BFO (black) and BFO post annealed in oxygen (green) and nitrogen (red).

Point defects can also arise from the chemical interaction between the sample and environment. Bein et al. [43] demonstrated that water adsorbed on the surface of BFO samples can act as an electron donor, inducing electrochemical reduction. As a result, Fe^{2+} and metallic bismuth (Bi^0) can be formed. Such interactions can occur when samples are exposed to humidity, or other liquid/water-based agents during processing or storage.

1.2.3 Dislocation defects induced by mechanical stresses

Dislocations are line defects in the crystal structure that can form either due to stresses induced by evaporation and diffusion of species at high temperature during annealing, repulsion forces from excess of local charge, or due to external stresses imposed onto the sintered material [44]. The latter is a matter of discussion herein. Two main types of dislocations are schematically presented in Figure 7, edge and screw dislocation, which differ in distribution of stress exerted on the bulk lattice, and the direction of the atomic plane sliding.

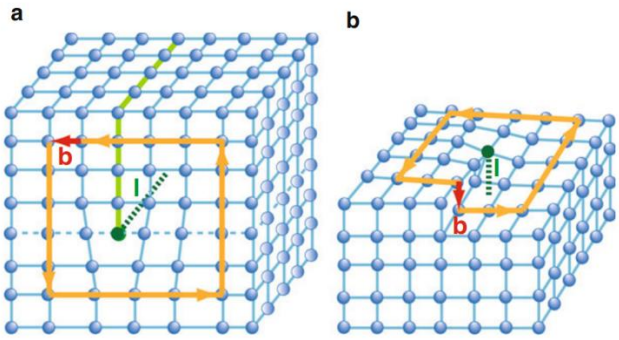

Figure 7: Two major types of dislocations in the crystal structure: (a) edge; (b) screw dislocation. Reproduced from [45] with permission from Springer Nature.

Dislocation formation and existence is important as it may alter material's properties, both the mechanical properties, as well as electromechanical response. Upon external stress

fields applied, dislocation movement can cause permanent deformation in the material, i.e., plastic deformation, through its ductility via a continuous lattice and dislocation creep. While such plastic deformation is usually observed in metals, which are considered to be ductile due to the nature of the metallic bonds, oxides were also shown to plastically deform under uniaxial stress, despite being considered brittle due to their stronger ionic and covalent bonds. It does, however, indicate that ceramics normally deform elastically more than metals before entering the plastic deformation regime. Dislocations can also severely influence the distribution of charges, and can significantly affect the domain wall movement by pinning the walls, and thus the electromechanical response. It was shown that the critical stress to induce permanent deformation, i.e., plastic deformation, in the case of $KNbO_3$ perovskite up to 400 °C was 30-45 MPa, while at temperatures above 400 °C, in the cubic phase, it was reduced to 10-15 MPa (Figure 8a) [46], [47]. This reduction can be explained by phase symmetry: cubic symmetry has fewer available slip planes compared to orthorhombic symmetry, which is why the stress required to induce defects at temperatures above 400 °C is lower than at temperatures below 400 °C [48].

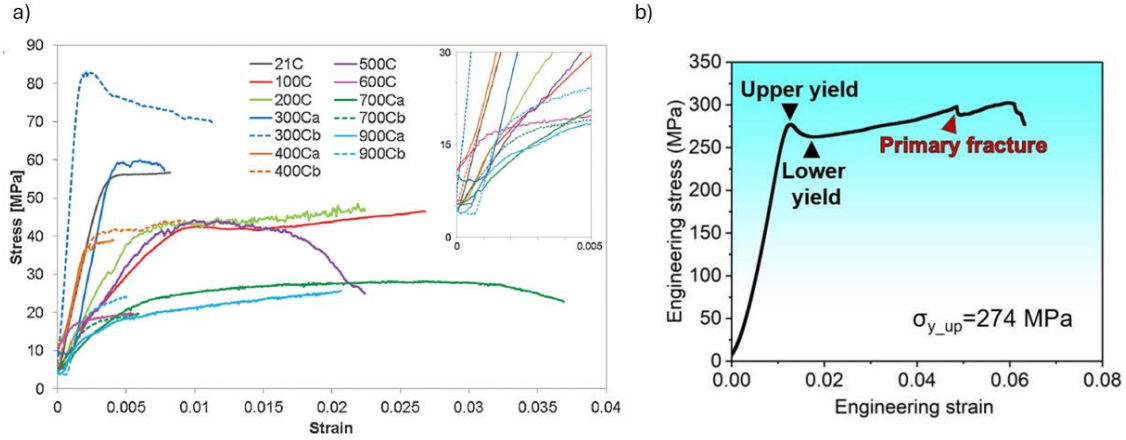

Figure 8: (a) Stress-strain responses of $KNbO_3$ in the temperature range 21 °C - 900 °C. Reprinted from [46] with permission from Elsevier; (b) stress-strain responses of $KTaO_3$ at room temperature [49], indicating yield strength of the two perovskites.

Wang et al. [50] demonstrated how crystal symmetry affects the value of applied stress, needed to induce dislocations and creep. In particular, the creep strength in orthorhombic perovskite symmetry is higher than that of cubic symmetry. The detailed analysis of uniaxial compression of $KTaO_3$ revealed that the stress-strain curve exhibits both upper and lower yield points (Figure 8b), attributed to dislocation multiplication, which causes a stress drop [49] but keeps the material from total failure. *In-situ* analysis with stress on the crystal applied along <001> pseudocubic direction showed that dislocation slip plane occurs at 45° to the loading axis, on the {110} planes, with a lattice friction stress for dislocation glide at room temperature of 137 MPa. *Klomp et al.* [51] identified different origins of dislocations in $SrTiO_3$: one resulting from easy gliding along the {110} planes, induced by mechanical stress, and another from dislocation splitting into partial dislocations, attributed to the ionic structure of $SrTiO_3$, which suppresses the movement of charges close to each other. Such dislocations can also be influenced by the presence of vacancies and the density oxygen ions on specific planes.

Crystal symmetry not only influences the conditions for the formation of dislocations, but also affects the nucleation of domains at dislocated regions. It has been shown that in deformed regions of $KNbO_3$ in the tetragonal phase, domain density was higher compared to the same regions in the orthorhombic or cubic phases [47]. Furthermore, according to results obtained by *Hu et al.* [52], these domains (pinned to the dislocated regions) are the

last to disappear during heating and transitioning from the ferroelectric to the paraelectric phase. During cooling, these domains were shown to form first. This yields dislocations as stabilizing the ferroelectric state. Therefore, one of the main consequences of the presence of dislocations in ferroelectrics is their strong influence on domain wall mobility and thus on the ferroelectric properties of perovskite materials. In the case of PZT thin films, measurements of the piezoelectric properties using atomic piezoresponse force microscopy further revealed depolarizing fields around the dislocations, induced by misfit strain at the substrate interface [53]. This could be related to the influence of misfit strains in dislocated regions, contributing to depolarizing fields and influencing the intrinsic polarization.

New techniques that enable the production of dense bulk electroceramics at reduced sintering temperatures using externally applied fields/forces can also influence formation of defect. For example, during the cold sintering process where uniaxial pressure, additives, and temperatures below 300 °C are applied, the obtained ceramic samples may contain defects such as point defects caused by chemical interactions of additives with the perovskite structure, or line and plane defects caused by pressure. These can severely affect the response of ferroelectrics. The influence of cold sintering conditions on the electromechanical responses of the ferroelectrics is described in chapter 1.4.

1.3 Sintering Methods

This subchapter describes the main sintering techniques used in the processing of ferroelectrics, with a focus on the influence of sintering temperature on grain growth and porosity. The common and contrasting features between the well-known sintering approaches, i.e., conventional sintering, liquid-phase assisted sintering and spark plasma sintering are reviewed. These are taken as reference to compare to the recently developed cold sintering process (CSP), which is the major topic of this PhD, and is described in the next chapter.

1.3.1 Conventional sintering techniques

The primary goal of sintering is to promote the binding of loose particles and their densification to form a coherent ceramic body. The solid-state sintering depends on thermally-induced diffusion of species. In classical solid-state sintering, initial powders are heated in air or selected atmosphere to elevated temperatures, i.e., 900–1400 °C, maintained at the desired temperature for few to several hours, and then cooled to room temperature [54]. This process involves three main stages: (1) neck formation (initial stage), (2) densification (intermediate stage), and (3) grain growth as a final stage (Figure 9). In the first stage of sintering, necks between particles grow due to material transport (surface diffusion) and grain boundaries start to form. In the second stage, a strong interconnected porous microstructure starts to densify via lattice diffusion and grain boundary diffusion. This can be observed as pore closure and shrinkage of the material. The relative density during this stage usually increases to above 90 % and isolation of pores occurs (closed pores). In the final stage of sintering, closed pores start to shrink and densification slows down. Material transport is driven by lattice diffusion. This step is accompanied by grain growth: the larger grains grow at the expense of smaller ones.

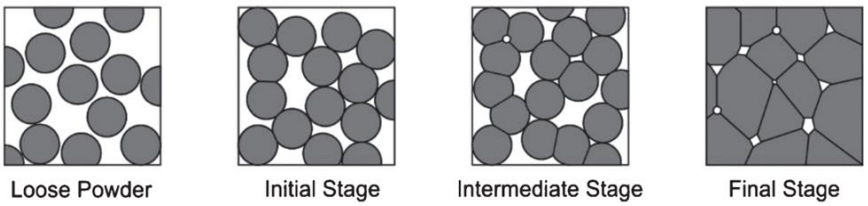

Figure 9: Stages of sintering. Reprinted from [55] with permission from Wiley Materials.

The kinetics of solid-state sintering is therefore driven by diffusion, as the stages in the solid-state sintering are strongly related to the migration of atoms. The sintering temperature is commonly determined to be at 2/3 of the ΔT between the temperature of start of volume shrinkage and the melting temperature. This temperature is defined as the optimal temperature for lattice diffusion and densification.

One of the strategies to influence the sintering process and the microstructure is to sinter the material in the presence of the liquid phase [56] [56],[57], [58]. In this case, a compound in concentration as low as a mole percent with a lower melting point than the ceramic is mixed with a ceramic powder. During the sintering of ceramic compacts this compound melts, impacting the densification process in terms of lowering the sintering temperature, increasing grain boundary mobility and grain growth rate.

Figure 10 illustrates an A-B binary phase diagram describing liquid phase sintering. When liquid phase is present between the ceramic particles during the sintering, enhanced densification can be achieved. Figure 11 shows grain boundary contacts during solid-state and liquid-phase sintering and corresponding densification as a function of time at constant temperature. During liquid-phase sintering, the following stages are in effect (Figure 11c): (1) better rearrangement of ceramic particles and (2) enhanced material transport through the liquid phase (i.e., dissolution-precipitation) and, in the final stage, (3) solid-state sintering proceeds with strongly reduced rate of densification. Thus, the liquid phase contributes to enhanced diffusion of species and reduced porosity, which in the final stage also diffuses into the matrix and is not detected in the microstructure after LPS is complete. When liquid is present, the main parameter that controls the diffusion at the grain boundaries is the diffusion coefficient of the solute atoms in the liquid and the thickness of the liquid bridge [56].

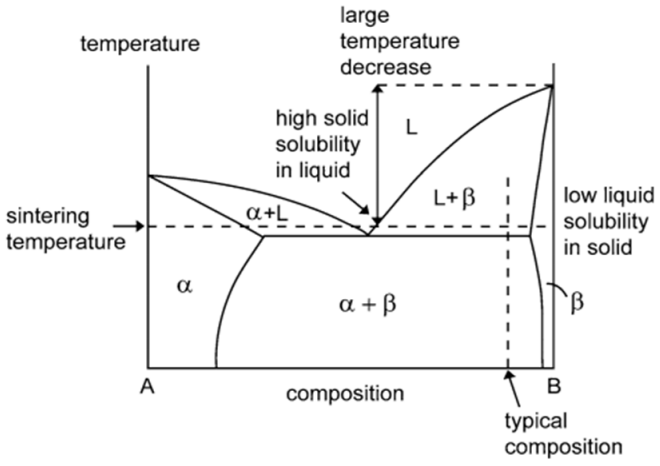

Figure 10: A-B phase diagram for liquid phase sintering [57]

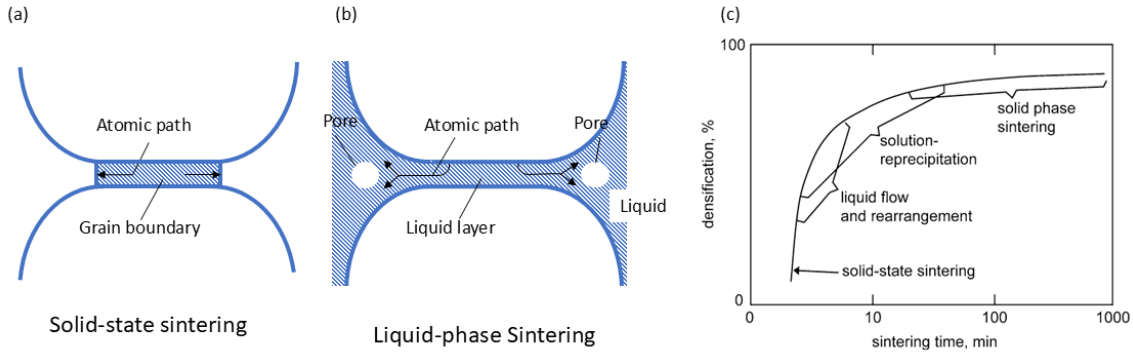

Figure 11: Comparison of grain contacts and atomic path for diffusion in (a) solid-state sintering and (b) liquid-phase sintering. Redrawn from [56]. (c) A schematic of the overlapping events in LPS; densification is very rapid at early sintering stage with rapid chemical diffusion; as liquid forms with time, solution-reprecipitation occurs and eventually slows down the densification [57].

Sintering of material in the presence of the liquid phase results in a denser material processed at lower sintering temperature than in solid-state sintering. A disadvantage of liquid-phase sintering could be undesirable abnormal grain growth [59], and remaining of a glassy intergranular phase in the ceramic, which can degrade functional and mechanical properties of ceramics, such as creep and fatigue resistance [11].

Another technique to limit grain growth is the Spark Plasma Sintering (SPS) [60]. The principle of SPS is based on pulsing direct current through the powder compact with additionally applied uniaxial pressure. Thus, heat is delivered to the entire powder via low voltage, producing high currents, up to 10000 A. Thanks to this, it is possible to increase the temperature very rapidly, for example with a rate of 1000 °C/min [61] while the applied current and uniaxial pressure promote the densification process. The entire process is commonly performed in vacuum. The advantage of SPS is to sinter material to high densities within a short time period, typically a few minutes. The drawback of this technique is that the material can be locally exposed to very high temperatures, which can melt the material at the grain boundaries, causing an electrically conductive path. Also, the grain size derived by this technique is more or less limited to the initial particle size as fast heating rates and short sintering times limit the diffusion. In the case of sintering nano-sized powders, small particle size may pose a problem to obtain good functional response of ferroelectric materials. The problem could be also the fact that the chemical species in the sample may be reduced during SPS, which requires re-oxidation of the samples via a post-annealing step at elevated temperatures and oxidizing atmospheres [62].

1.3.2 Mitigation strategies to sintering problems in KNN and BFO

It may be challenging to process dense and homogeneous ceramic with targeted functional response from chemically and structurally complex materials. In this chapter we explain some of the mitigation strategies for sintering lead-free ferroelectric perovskites that contain volatile species.

Among the lead-free ferroelectric perovskites, BFO, KNN, BT and NBT-based compositions are considered to replace lead-containing electroceramics. KNN and BFO are ferroelectrics that attracted special attention since they have a relatively high Curie

temperature (T_c), making their ferroelectric properties accessible in a wide temperature range. KNN is vastly studied for its highest piezoelectric response among lead-free compositions, while BFO is considered for its multiferroic and high-temperature ferroelectric properties. In particular, the T_c of KNN is 410 °C [63]–[65], while BFO has a T_c at 825 °C [66], [67], which makes BFO interesting for high-temperature applications. The remanent polarization (P_r) of BFO can reach 60 µC/cm^2 (thin films) [68] and even 100 µC/cm^2 (single crystal) [69], indicating a large intrinsic contribution to polarization. KNN, on the other hand, is considered the best lead-free material for piezoelectric applications, as it can reach up to 700 pC/N [70]. These properties make the two lead-free perovskite materials interesting for industry, however, the main difficulty remains the processing of dense, single-phase materials with reproducible properties.

In case of KNN, for example, exaggerated grain growth, volatilization of species, and low density of the ceramic all limit its use. Exaggerated grain growth leads to the formation of grains with size above 10 µm with trapped intragranular pores and large open porosity [71]. This is related to the diffusion processes at low temperatures, i.e., surface diffusion is favored over the lattice diffusion, triggering exaggerating grain growth. To suppress this process, especially in KNN, the hot-pressing method has been used. Therein, uniaxial pressure is applied to the powder compact together with a fast heating rate to reach the final temperature as fast as possible [72]. The exaggerated grain growth, limited densification and volatility of species can also be limited by fast sintering techniques such as SPS [62], [73], [74], by doping KNN (for example, low amount of Sr in KNN suppresses grain growth [75]–[77]), and the use of reducing sintering atmospheres causing point defects [78].

In the case of sintering BFO, on the other hand, one of the main problems is related to the thermodynamic instability of BFO, which can be described by the following equation:

$$1/49Bi_{25}FeO_{39} + 12/49Bi_2Fe_4O_9 \rightleftharpoons BiFeO_3 \quad (1)$$

The reaction in equation (1) indicates a delicate balance in the temperature range of 447 – 767 °C between BFO and a two-phase system, formed of the Bi-rich sillenite and Fe-rich mullite phases [79]. It has been shown that the first product forming during BFO calcination or reactive sintering is the Bi-rich phase ($Bi_{25}FeO_{39}$) [79]–[82], which at sintering temperature should transform to BFO. In cases of incomplete BFO formation, the sillenite phase may remain and begin to melt through peritectic decomposition at temperatures >790 °C [83], [84]. This process leads to the evaporation of Bi_2O_3 and the segregation of the liquid phase [79]. Additional Bi_2O_3 losses can be observed at temperatures >820 °C [85]. Thus, there is a narrow temperature window of 767-790 °C where BFO can be sintered from a thermodynamic perspective, however, it is still challenging to achieve significantly densified ceramics. To overcome this, researchers have employed fast heating rates to quickly pass through the critical BFO instability temperature range of 447 - 767 °C. Another possibility is to immerse the pressed BFO pellet in Bi_2O_3 powder to suppress Bi_2O_3 loss [79] at a higher sintering temperature. The volatilization of Bi_2O_3 also impacts the valence state of Fe, changing it to Fe^{2+}/Fe^{4+}, creating defect dipoles that can make BFO conductive, as mentioned in chapter 1.2.2. To address this issue, sintering in an oxygen-free (reducing) environment can help. However, even with techniques such as SPS which allow for an extremely fast approach to the sintering temperature, limiting volatility and obtaining bulk ceramics without secondary phases [86], it remains challenging to eliminate electrical conductivity in BFO, necessitating a post-annealing step [87].

The problem with relatively low relative densities of conventionally sintered BFO, i.e., between 90–95% of the theoretical density, is caused by grain coarsening with entrapped pores and open porosity [88]. To avoid the coarsening process in BFO, approaches such as

the use of dopants [89], hydrothermal microwave-assisted synthesis [89], and mechano-chemical activation prior to sintering were employed [79].

Since the above-described issues related to the densification of KNN and BFO mainly result from the high-temperature processing of ceramics, significant reduction of the sintering temperature could potentially help to avoid these difficulties. I therefore aimed in this dissertation to apply the cold sintering process (CSP) to sinter the BFO and KNN ceramics at temperatures as low as 300 °C. The CSP processing parameters such as uniaxial pressure and chemical reactions between additives (chemical compounds promoting the process of sintering) and ceramics, however, may introduce new challenges, which I investigated in this work. The basic mechanisms of CSP and literature survey on cold-sintered perovskites are described in Chapter 1.4. Furthermore, details on the impact of liquid phase on cold-sintering of BFO, optimization of pressure during cold-sintering of KNN and introducing cold sintering to obtain perovskite-perovskite BFO-KNN composites were investigated and are presented in the herein presented articles.

1.4 Cold Sintering Process

The cold sintering process emerged in the last decade as a viable energy saving and environment friendly technique for processing oxides. While conventional sintering methods with high-temperature processing consume substantial amounts of energy, techniques like CSP offer a budget solution, which, however, is still not at the upscaling readiness level. A comparison of the cost and saved energy for different processing techniques was conducted by *Ibn-Mohammed et al.* [90] for cold sintering of zinc oxide (ZnO), barium titanate (BT), and lead zirconate titanate (PZT). It was shown that the SPS technique saves a lot of energy but requires significant investment, while the lowest investment was calculated for CSP.

We describe here the operation protocols and mechanisms of the cold sintering process, its benefits and limitations for processing different materials, the importance of the liquid phase and pressure used, and finalize with an overview of so-far sintered perovskite materials, since the main perspective of this thesis is to study the viability of cold-sintering of ferroelectrics.

1.4.1 Mechanism of cold sintering process

The term "cold sintering" was initially introduced in the field of metallurgy, where the authors densified a green metallic body to nearly theoretical density through the plastic deformation of metallic powders by squeezing/compression [91]. In 2016, researchers used the same terminology in relation to ceramic materials [92], when trying to densify oxides by applying pressure.

CSP is a technique that allows the production of dense ceramic materials (with relative density >90 %) at temperatures between room temperature and 300 °C. The technique requires uniaxial pressure, which can reach 650 MPa, and a small amount of liquid phase (solution) that moistens the powder and during sintering squeezes through the inter-grain region. The duration of CSP can range from several minutes to several hours. The main processes that occur during CSP are dissolution, diffusion, precipitation, and plastic deformation [93] (Figure 12): the first three contribute to surface etching of ceramic grains, their interpenetration with applied pressure and cementation of the pores with precipitated matter, respectively, while the last step contributes to densification of ceramics through dislocation formation and lattice dislocation creep.

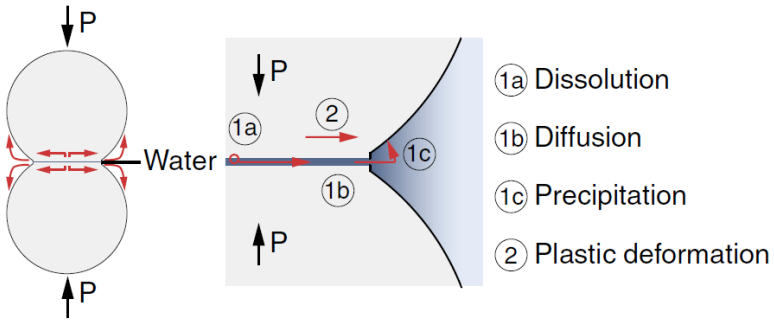

Figure 12: Processes during CSP (black arrows mark the direction of applied uniaxial pressure; red arrows represent the direction of matter transport) [93].

The mechanisms of CSP during densification are presumably very similar to the conditions of carbonate rock formation during geological processes [93], [94]. In the process of lithification of carbonates, mineralized geothermal water constantly washes the carbonates, serving as a source of calcium, which together with high lithostatic pressure aids the pressure-dissolution process. After the solution saturates, growth of carbonates under high lithostatic pressure starts in the form of cement, limiting the fluid migration and further dissolution. This **pressure-dissolution-precipitation process** can take a long time in geological conditions. Combination of uniaxial pressure and migrating liquid phase, triggering the pressure-dissolution process is considered the driving force for the lithification of carbonates [95]–[98]. The CSP is thus far understood as a process similar to formation of carbonates and takes the basic understanding of pressure-solution creep as the crucial mechanism in the densification of ceramics. Therefore, the pressure-solution creep is a mechanism where the driving forces are dissolution, diffusion, and precipitation, which are linked to the gradients of chemical potential in the liquid phase covering the grain surfaces [94], and to the applied stress. The chemical potential gradient $\Delta\mu$ can be expressed as:

$$\Delta\mu \sim (\sigma_n - P_f)\Omega \quad (2)$$

where σ_n is the normal compressive stress at the grain-to-grain contact, P_f is pressure of fluid in the open pores and Ω is molar volume of stressed solid. Open pores allowing liquid phase migration are crucial here. Factors impacting the chemical gradient include the particle size of the initial powder, volumetric strain, initial green porosity, diffusivity of ions in the liquid phase close to the grain boundary, solubility of the solid phase, and the thickness of the liquid phase film on the grain boundary [94]. If $\Delta\mu > 0$, mass diffusion is directed from the contact point toward the open pores, enabling dissolution. If $\Delta\mu < 0$, mass diffusion is directed from the open pores toward the contact points/grain surfaces, resulting in cementation. Consequently, the grain boundaries and pores become covered by the precipitated phase that cements the material, ending the pressure dissolution process, allowing only the plastic deformation to continue compaction.

Following the densification process when $\Delta\mu > 0$, with the crucial parameter being the dissolution process, high densities can be achieved by selecting an appropriate liquid phase [95]–[100]. In particular, the relative density of cold-sintered carbonates can significantly change depending on the selected liquid phase with different polarity and dissolution potential (Figure 13). As shown in Figure 13, even a small amount of carbonate solubility in water plays a significant role in promoting CSP. In contrast, in oil, where carbonates are not soluble at all, CSP is entirely inhibited.

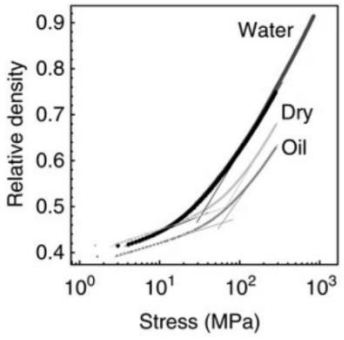

Figure 13: Impact of water and oil as a liquid phase on CSP of carbonate (dry means without any liquid phase) [93].

The dissolution process during CSP can be viewed not just as a physical process where molecules of the liquid phase surround the molecules of the matrix matter and transport it in solubilized form to another site. It can also proceed as the chelation of matrix matter by organic molecules [101]. In this case, the organic molecule can create separate coordinate bonds with species of matrix matter molecules.

In the mechanism of CSP, it is also crucial to have an open system; otherwise, the liquid will not be able to squeeze out between particles of matrix matter, and the diffusion process will be suppressed [92]. Due to the liquid phase's ability to squeeze out between particles under uniaxial pressure, it is often referred to as the transient liquid phase (TLP). If the liquid phase becomes trapped in closed pores, it saturates, leading to the onset of precipitation.

The particle size distribution of the solid powder also plays an important role in CSP. It has been shown that Na_2WO_4 powders with average particle sizes of 0.63, 2.52, and 4.48 µm were successfully cold-sintered, while powder with an average size of 17.83 µm showed a significant decline in density [102]. This decline can be attributed to the difficulty of particle rearrangement and the lower surface energy of larger particles.

1.4.2 Cold sintered oxides

A prerequisite condition to cold-sinter oxide ceramic materials is their partial solubility in the added liquid. Initial studies on cold-sintering were done on inorganic salts that are soluble in water. Specifically, materials such as Li_2MoO_4, $Na_2Mo_2O_7$, $K_2Mo_2O_7$, KH_2PO_4, $NaNO_2$, Li_2MoO_4 and $CaCO_3$ were cold-sintered at 100-200 °C for 15-60 minutes [92], [103]–[105]. High relative densities were achieved in these cases (more than 90% of the theoretical density) via CSP by using water as the transient liquid phase sintering agent. Among non-water-soluble materials like simple binary metal-oxides, the use of organic acids to form chelate complexes with metal ions was utilized, as well as a combination of different inorganic additives. For instance, ZnO and MnO were successfully cold-sintered with acetic acid, dimethyl sulfoxide, acetate of Zn and Mn at room temperature up to 300 °C for 1-5 hours under 300-500 MPa [106]–[108]. The purpose of using Zn and Mn acetates is to break the metal-oxide bonds and fill the inter-grain spaces with ZnO precipitates/cement, thereby increasing the density.

1.4.3 Cold sintered perovskites

The development of the CSP technique for ferroelectric perovskite began in 2016 when Prof. Randall, head of the materials research group at Pennsylvania State University in

the USA, highlighted the potential to achieve dense bulk (~ 93%) $BaTiO_3$ using a $Ba(OH)_2/TiO_2$ aqueous suspension. This was achieved under 430 MPa pressure at 180 ℃ for 1–3 hours, followed by annealing at 700–900 ℃ [109]. In Figure 14, it can be seen that after CSP, the intergranular spaces are filled with a glassy amorphous phase, while annealing at 700 ℃ results in a more crystallized microstructure, with no amorphous phase observed after annealing at 900 °C. The primary goal was to obtain the $BaTiO_3$ phase via a reaction between $Ba(OH)_2$ and TiO_2 - in other words, reactive cold sintering. This involves forming a perovskite structure through precursor reactions under CSP conditions: applied uniaxial pressure, use of TLP, and temperatures below 300 °C. Typically, the precursors are similar to those in conventional reactive sintering and include hydroxides and/or oxides of the metals involved.

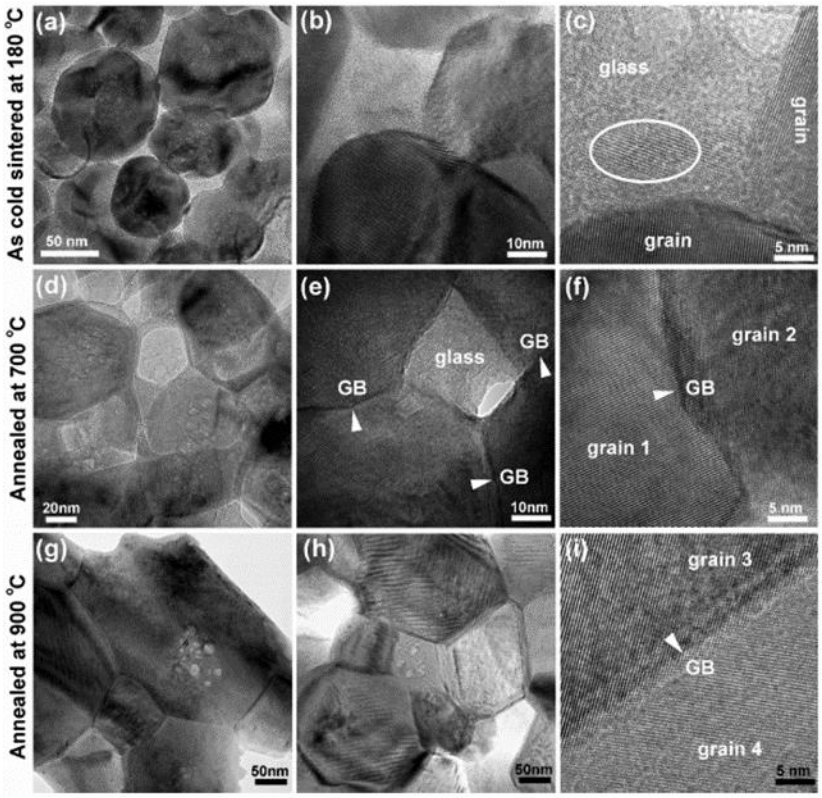

Figure 14: SEM images of cold-sintered $BaTiO_3$ with $Ba(OH)_2/TiO_2$ suspension (a)-(c) without postannealing and after postannealing at 700 ℃ and 900 ℃. Reprinted with permission from [109]. Copyright 2025 American Chemical Society.

In an attempt to cold sinter other perovskites like NBT [110], STO [111], BTO [109] and PZT [112], researchers tried to fill the inter-grain spaces by transient liquid suspensions of $Bi(NO_3)_3$/NaOH, $SrCl_2$, $Ba(OH)_2$ and TiO_2 nanoparticles in water, lead nitrate, respectively. This resulted in the formation of a cement of the same composition as the matrix phase during CSP, however, such cement most often remained amorphous. Due to the amorphous phase covering the grain surfaces, the dielectric properties were significantly reduced, making a post-annealing step necessary. Thus, the main purpose of post-annealing after CSP is to: 1) crystallize the amorphous or semi-glassy phases gluing the particles and 2) to promote reactive sintering. The post annealing step was required after CSP of $SrTiO_3$ [113], $Ca_3Co_4O_9$ [114], $Sr_{0.7}Bi_{0.2}TiO_3$ [115], PZT [112], $NaNbO_3$ [116], KNN [117]–[119], $0.9K_{0.5}Na_{0.5}NbO_3$-$0.1LiBiO_3$ [120].

The use of $Ba(OH)_2 \cdot 8H_2O$ and $Sr(OH)_2 \cdot 8H_2O$, along with H_2TiO_3, for the reactive cold-sintering of BTO, STO, $Ba_{0.5}Sr_{0.5}TiO_3$ and $Ba_{0.9}Sr_{0.1}TiO_3$ relates to the structure of hydrated hydroxides [121]. During CSP heating, the hydrates released water, which was crucial for the sintering of BTO and STO. It was suggested that the released water could partially dissolve $Ba(OH)_2$ or $Sr(OH)_2$ and H_2TiO_3, creating a saturated solution, and when supersaturation was achieved, the appropriate perovskite structure formed. The limitation of such reactive CSP is linked to the necessity of released water. Furthermore, the authors also used nano-sized powder and observed grain growth from approximately 30 nm up to 70 nm after CSP. However, as previously mentioned, this size range produces grains with a cubic structure. As a result, the final sample has a dense microstructure, but its ferroelectric properties are fully suppressed. Therefore, a post-annealing stage is necessary to reach micro-sized grains, where cubic symmetry can be transformed into tetragonal. These results provide a good example of how CSP does not significantly promote grain growth, and the final grain size remains almost the same as the initial particle size. Thus, CSP enables control of grain size in dense ferroelectric samples by controlling the particle size. Depending on the situation, this characteristic of CSP can be seen as either a feature or a limitation. Similarly, $BaZrO_3$ was cold sintered based on $Ba(OH)_2 \cdot 8H_2O$ and $Zr(OH)_4$ [122].

Aside from the post-annealing step after reactive cold sintering, issues such as matrix decomposition may also arise. In particular, researchers found that during the CSP of $BaZrO_3$ and $BaCeO_3$ composition (BZCY) the secondary phases like $Ba(OH)_2$, $BaCO_3$, and CeO_2 formed due to BZCY decomposition [123]

As seen, a drawback of reactive cold sintering is the necessity of a post-annealing stage at conventional sintering temperatures. This is why researchers have continued to explore cold-sintering of ferroelectric perovskites without the post-annealing step (single-step CSP). But the difficulty of single-step cold sintering is caused by inertness of ferroelectric perovskite materials to most solvents, making it challenging to find appropriate compounds serving as TLPs.

The first successful demonstration of single-step CSP for BTO involved using a eutectic mixture of NaOH and KOH in a 1:1 molar ratio, dissolved in water as a TLP. This approach enabled to achieve a relative density of 92–96 % within 3 hours at 300 °C under 400 MPa pressure [124]. The key feature of the NaOH+KOH mixture is that the eutectic molar ratio of 1:1 has a melting point around 170 °C [125]. During the CSP, this molten mixture fills the inter-grain spaces, and the applied uniaxial pressure promotes the sintering process. Figure 15 clearly shows the absence of secondary phases at the grain boundaries.

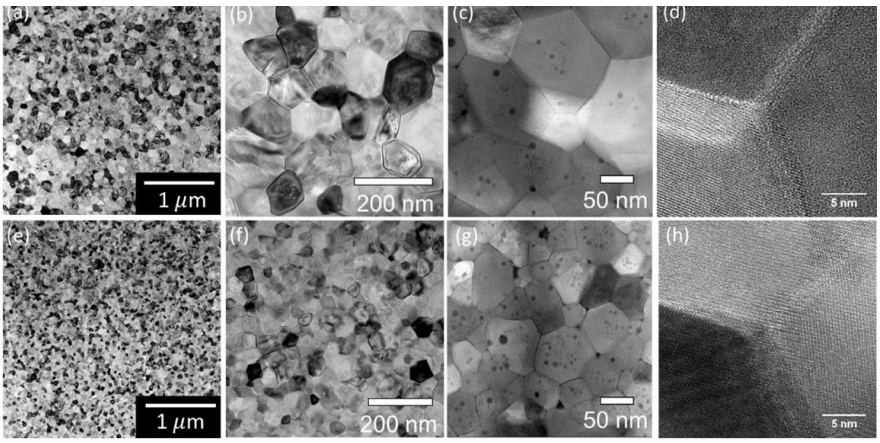

Figure 15: TEM images of cold-sintered $BaTiO_3$ without post-annealing (single-step) at different magnification. Reprinted from [124] with permission from Elsevier.

It is important to note that the authors used BTO nanopowder, and the cold-sintered sample retained a similar grain size as the initial particle size. However, they were able to measure the ferroelectric properties, suggesting that the sharp grain boundaries may have minimized the suppression of ferroelectric properties. Some studies even suggest that nano-sized grains could enhance ferroelectric properties [126], [127].

Although the use of a transient liquid phase utilizing the eutectic mixture of NaOH and KOH in solution is not specific to its use in cold sintering BTO ceramics, the liquid could serve as a universal transient liquid phase for CSP of various perovskites. However, only a few materials with perovskite structures, such as KNN and BFO (examined in the current dissertation), have been successfully cold-sintered via this single-step method. Despite the chemical inertness of most perovskites to a wide range of chemicals, electrochemical interactions remain possible. These interactions, especially if promoting incongruent dissolution of the matrix, may lead to the formation of secondary phases. For example, the electrochemical interaction of water with the surface of BFO can promote surface decomposition processes and the formation of Bi- and Fe-rich secondary phases [43], which may hinder the charge and strain transfer upon external field application, limiting the materials functionality.

1.4.4 Cold sintering of particulate composites

CSP has also been utilized for sintering particulate composites, although a post-annealing step was still necessary, for example in $0.3CaCeNbWO_8$-$0.7LaMnO_3$ [128] and $(1\text{-}2x)K_{0.5}Na_{0.5}NbO_3$-$xBaTiO_3$-$xBiFeO_3$ composites [129]. *Coutinho et al.* [130] were able to cold-sinter the $BaTiO_3$-ZnO particulate composite, where ZnO served as the matrix. The importance of CSP for the processing of particulate composites is more relevant since conventional sintering (cosintering) faces various issues. These include the volatilization of species and the diffusion of perovskite species into the lattice of the other phase, which can be caused by significant differences in sintering temperature and/or species ready to diffuse at the sintering T from one phase to another. For example, cosintering of KNN and $BaFe_{12}O_{19}$ at 1125 °C lead to volatilization of K and Na species [131], while cosintering of PZT and cobalt ferrite lead to diffusion of Fe^{3+} and Ti^{4+} ions, segregating, resulting in an increase in electrical conductivity [132]–[134]. Furthermore, the combination of several ferroelectric perovskites for cosintering of particulate composites can lead to the formation of cracks and laminated layers, as observed in the cosintering of cobalt ferrite and PZT [135], [136], and BFO and $Ni_{0.5}Co_{0.5-x}Zn_xFe_2O_4$ [137]. Such a phenomena is explained by the difference in thermal expansion coefficients of used perovskites.

CSP can also be applied to combinations of polymers with ceramics. To date, primarily oxides that are partially soluble in water, such as $Li_2Mo_4O_4$ (LM) [138], ZnO [139], $Li_{1.5}Al_{0.5}Ge_{1.5}(PO_4)_3$ (LAGP) [140], [141], $Na_2Mo_2O_7$ (NM) [142], and others, have been cold sintered with polytetrafluoroethylene (PTFE), poly(vinylidene fluoride-hexafluoropropylene) (PVDF-HFP), and polyetherimide (PEI), using water (or acetic acid in the case of ZnO) as the transient liquid phase at 120-300 °C under 100-750 MPa. Polymers can potentially contribute by increasing the dielectric breakdown strength as they generally exhibit higher strength than insulating ceramics. For instance, incorporating 10-20 vol % of PEI doubled the dielectric breakdown strength of NM-PEI composite compared to pure NM [142]. Additionally, LM-PTFE demonstrated good resonant frequency properties, making it a promising candidate for microwave applications [138].

1.4.5 Perspectives of CSP for industrial applications

The potential for upscaling CSP was first demonstrated with polymer-ceramic composite multilayers [143] by using tape-casting and lamination, a procedure that is common in industrial production of capacitors. The ceramic-polymer layers were tape-casted, cut and stacked, as schematically shown in Figure 16. After heating to burn out the binder, the stacked pellet was placed in a closed container with high water vapor content to adsorb water molecules at the surface and intergranular spaces. The adsorbed water was meant to act as the transient liquid phase, promoting sintering in the next step, when the stacked layers were placed in a die and cold-sintered. This procedure could be made continuous, which would make cold-sintering industrially interesting. However, at this stage, such a process could only be successful in the case when the ceramic material can be etched (and thus sintered) with water alone. When the additive, acting as a liquid-phase sintering aid, is not volatile up to water volatilization temperature, the sintering aid will not vaporize and enter the ceramic layers, which will prevent ceramics to be cold-sintered.

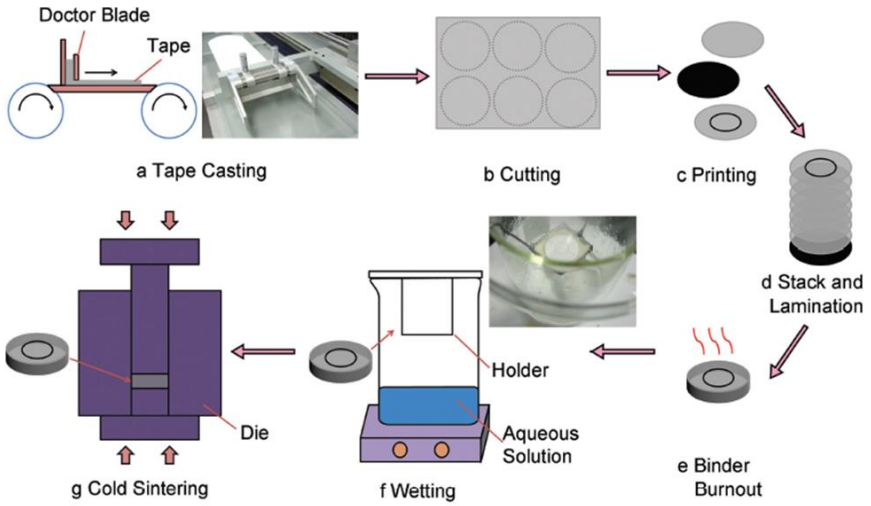

Figure 16: The possible scheme of CSP upscale. Reprinted (adapted) with permission from [142]. Copyright 2025 American Chemical Society.

Another direction towards upscaling the CSP was proposed later for the case of ZnO that can be cold-sintered with acids and Zn acetates. *Jabr et al.* [144] proposed stacking multiple pellets in a die to be sintered simultaneously within a single cylinder and pressing procedure (Figure 17). In this case they demonstrated that, while up to 5 pellets could be sintered at the same time, several parameters like the flatness of the die punch used for pressing, along with the heating rate, strongly influence the final density of the ZnO samples.

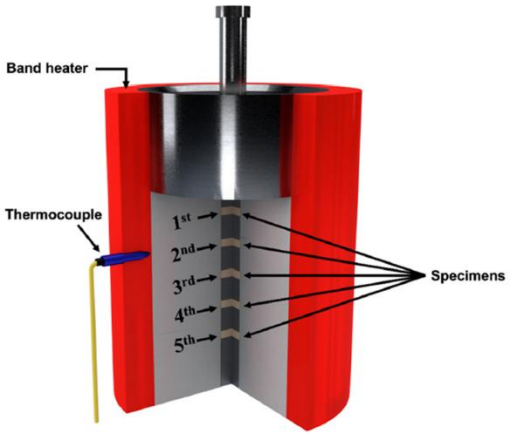

Figure 17: The possible upscale of CSP of ZnO [144].

Finally, it appears that CSP upscaling is feasible when certain conditions are met, e.g., when only water as a transient liquid phase is used in the case of tape-casting upscaling procedure of the ceramic, limiting the process to simple oxides. For cases involving perovskite materials, on the other hand, which require specific liquids that are able to dissolve the materials surface, sufficient pressure and temperature applied, the upscaling process becomes considerably more challenging and new pathways remain to be discovered and proposed.

1.5 Aims and Hypotheses of the Dissertation

Aims of the dissertation are:

1. To utilize the cold sintering process (CSP) to fabricate dense BFO ceramics with a relative density of above 90%, reaching a level comparable to conventionally sintered samples without the need for post-annealing. The objective is to obtain a similar remanent polarization to conventionally sintered samples while ensuring that the conductivity does not exceed that of the conventionally processed ceramic. Various transient liquids will be utilized, starting by common mineralizers that are used in hydrothermal synthesis, chelate complexes, and the hydroxide eutectic mixtures. Additionally, the duration (up to 15 hours), temperature (up to 300 ℃), uniaxial pressure (up to 670 MPa), heating rate (up to 20 ℃/min) of the CSP, and most importantly, the particle size and distribution will be varied to investigate their impacts on the microstructure and functional properties of the cold-sintered BFO ceramics.

2. The fabrication of dense KNN ceramics by CSP and evaluating the materials' energy storage efficiency. With a relative density target of above 90%, the objective is to achieve a non-pinched and saturating polarization-electric field loop at high applied electric fields (up to 200 kV/cm) in the KNN ceramic, without reaching a dielectric breakdown. This will be accomplished through cold sintering of KNN using the hydroxide mixture as the transient liquid and by optimizing the applied pressures and, especially, heating rates, since the material undergoes a phase transition when heated to 300 °C, imposing stresses within the compact. Additionally, the particle size distribution of the KNN powder will be modified to achieve the best functional results, with one batch having particles approximately 2-5 times larger than another, in order to explore the impact of particle size on the density and energy storage properties of the KNN ceramics.

3. Co-sintering of KNN and BFO ceramics to achieve a homogeneous distribution of both phases in a particulate composite without their inter-miscibility. The microstructure and functional properties will be evaluated and the possible application of the composites foreseen.

The hypotheses of the dissertation are as follows:

1. BFO ceramics can be successfully cold sintered using the NaOH-KOH mixture. By sintering at temperatures up to 300 ℃, volatilization of Bi_2O_3 and creation of oxygen vacancies should be minimized, leading to dense BFO samples with reduced conductivity and enhanced ferroelectric properties. The parameters of the cold sintering process will be varied to achieve high density.

2. As hydroxides are hygroscopic, we anticipate that the cold-sintered ceramic may be sensitive to moisture, potentially increasing the dielectric losses. To address this issue, we hypothesize that drying the ceramics under vacuum and measuring their ferroelectric properties in protective liquid (oil) will mitigate the moisture-induced impact on dielectric losses.

3. For KNN ceramics, we expect that the grain size will not undergo significant enlargement during the cold sintering process. This means that the size of the grains will remain within the same range as the size of the powder particles used, which should influence the following: dielectric breakdown to occur at higher electric fields than in large-grain ceramics; slim P-E hysteresis loop (indicating low losses) and low remanent polarization. Such a material is anticipated to be suitable for energy storage applications. We further hypothesize that oxidizing cold-sintered KNN will improve the functional response by unpinching the P-E loop, similar to what has been reported for KNN samples processed using spark plasma sintering [33].

Chapter 2
Impact of Transient Liquid Phase on the Cold Sintering of Multiferroic $BiFeO_3$

We have investigated the influence of different compounds used as transient liquid phases (TLP) on the microstructure and functional properties of $BiFeO_3$ (BFO) ceramics.

First, we present a detailed analysis of the secondary phases formed in BFO during cold sintering (CSP) using NaOH, KOH and urea dissolved in water and ethanol in different ratios. Urea was chosen as it was previously shown that under hydrothermal conditions it promotes mineralization of BFO, while ethanol, as an organic solvent, was used as it evaporates easily, leaving only hydroxides which subsequently melt above 170 °C. When using carbonaceous solvents (urea and ethanol), we observed the formation of secondary phases, bismuth carbonate and iron oxide. The secondary phases are predominantly located at the grain boundaries of BFO and limit the densification of the ceramic. The results indicate that the dissolution of the surface of the perovskite grains is limited or terminated when the secondary phases precipitate, resulting in lower relative densities and poor contacts between the matrix grains.

Second, we show how the presence of secondary phases degrades the functional properties of BFO. In particular, cold sintered BFO with secondary phases is electrically conductive and has high dielectric losses. We also investigated the influence of the frequency and sequence of the applied electric field during the polarization electric field measurement of cold-sintered BFO on the evolution of the P-E loop. The P-E loops of CSP and conventionally sintered BFO ceramics were compared and discussed.

We investigated how the type of defects in the cold-sintered ceramics affect the existence and movement of the domain walls. We found that larger fields are required for switching domains and increasing remanent polarization in cold-sintered ceramics. On the other hand, cold-sintered BFO showed significantly higher dielectric breakdown strength, reaching up to 220 kV/cm, compared to about 150 kV/cm for conventionally sintered samples.

This chapter addresses thesis objective 1.

Published in: Salmanov, S., Yao, M., Žiberna, K., Lachhab, M., Dkhil, B., Malič, B., Rojac, T., Kuščer, D. and Otoničar, M., Impact of transient liquid phase on the cold sintering of multiferroic $BiFeO_3$. Journal of the European Ceramic Society, 45(1) (2025) p.116846.
https://doi.org/10.1016/j.jeurceramsoc.2024.116846

My contribution: I synthesized the starting powders that I used for cold sintering, cold-sintered all samples under different conditions, prepared samples for SEM and EDS analyses, measured densities, and performed the measurements of dielectric and ferroelectric properties. I also performed the necessary calculations, interpreted the results, and developed the manuscript together with co-authors.

Journal of the European Ceramic Society 45 (2025) 116846

Contents lists available at ScienceDirect

Journal of the European Ceramic Society

journal homepage: www.elsevier.com/locate/jeurceramsoc

Impact of transient liquid phase on the cold sintering of multiferroic $BiFeO_3$

Samir Salmanov [a,b], Minghai Yao [c,d], Katarina Žiberna [a,b], Meryem Lachhab [a,b,d], Brahim Dkhil [d], Barbara Malič [a,b], Tadej Rojac [a,b], Danjela Kuščer [a,b], Mojca Otoničar [a,b,*]

[a] Electronic Ceramics Department, Jožef Stefan Institute, Jamova cesta 39, Ljubljana 1000, Slovenia
[b] Jožef Stefan International Postgraduate School, Jamova cesta 39, Ljubljana 1000, Slovenia
[c] Huazhong University of Science and Technology, Wuhan, Hubei, China
[d] Université Paris-Saclay, CentraleSupélec, CNRS-UMR8580, Gif-sur-Yvette 91190, France

ARTICLE INFO

Keywords:
Cold sintering process
bismuth ferrite
Ferroelectric ceramics
Etched grain boundaries
Secondary phases
Hydroxide mixture

ABSTRACT

Cold sintering of perovskite materials is still, despite years of research, challenging. The key objective when cold-sintering oxide materials is finding an appropriate liquid phase that triggers pressure-dissolution process and mechano-chemical compaction and densification of ceramics. In this study, cold sintering of the multiferroic $BiFeO_3$ perovskite is reported for the first time. When organic additives or solvents are used, these effectively sinter the compound, but cause precipitation of secondary phases that impede grain-to-grain contacts and the polarization coupling, and result in electrically conductive samples. We found that it is critical to carefully select the sintering additives based on their reactivity, decomposition temperature and products, while ensuring a significant level of wettability and matrix solubility. NaOH/KOH mixture was found to be the best sintering aid, resulting in remanent polarization and strain responses of cold-sintered BFO comparable to those reported for conventionally sintered ceramics.

1. Introduction

$BiFeO_3$ (BFO) is a multiferroic perovskite material that couples ferroelectric and antiferromagnetic properties. Its intrinsically high spontaneous polarization (predicted to be up to 100 $\mu C/cm^2$ along [111]) [1,2] and a high Curie temperature of ~825 °C make it interesting for the use in diverse applications [3]. However, in ceramics its potential values of polarization are often not reached, which likely stems from high electrical conductivity at the local (domain wall) scale [4,5], leading to high dielectric permittivity and dielectric relaxation of so-called Maxwell-Wagner origins in the low-frequency (Hz-to-kHz) range. Nevertheless, it offers possibilities to combine polarization, strain and spins in a single phase, which makes BFO highly investigated for applications such as multifunctional devices, nanoelectronics, high-temperature sensors, or for piezo-photocatalysis [6–8].

Studies on ceramics processing have shown that obtaining dense, single-phase BFO ceramics is a challenge. Secondary phases such as $Bi_{25}FeO_{39}$ and $Bi_2Fe_4O_9$ often form during calcination or reactive sintering at ~800 °C due to a delicate thermodynamic balance of the reaction converting BFO to the secondary phases in their overlapping stability regions [9–11]. Volatility of bismuth can also cause undesired effects, such as creation of bismuth and oxygen vacancies and charge compensation on the B-site in the perovskite, with changed valence states of iron [12]. Such defects can create defect complexes that segregate at the domain walls, causing domain-wall conductivity and pinning effects [13,14], which may significantly impair the ferroelectric properties of BFO. Therefore, advanced sintering techniques are being utilized, from annealing in different atmospheres [15], to spark plasma sintering [16,17] or flash sintering [18], with the idea to limit the elemental losses, secondary phase formations, exaggerated grain growth, or porosity. The latest achievements in ceramics processing are related to the novel sintering technique called the cold sintering process (CSP), which allows to obtain dense ceramics at temperatures below 300 °C, thus tackling the main drawbacks of conventional sintering (e.g., volatilization and uncontrolled diffusion) [19–21].

During the CSP, applied pressure (up to 650 MPa) and added liquid phase drive the pressure-dissolution process, which is the main driving force for sintering [22,23]. For the activation of this process, one of the key challenges is to identify an appropriate compound that can act as a transient liquid phase (TLP) promoting dissolution of the particle/grain surface, chemical reactions, or formation of chelate complexes, and subsequent densification. Since materials with the perovskite ABO_3

* Corresponding author at: Electronic Ceramics Department, Jožef Stefan Institute, Jamova cesta 39, Ljubljana 1000, Slovenia.
E-mail address: mojca.otonicar@ijs.si (M. Otoničar).

https://doi.org/10.1016/j.jeurceramsoc.2024.116846
Received 22 April 2024; Received in revised form 15 August 2024; Accepted 15 August 2024
Available online 23 August 2024

oxide structure are mostly inert to solvents, this poses a challenge for their successful sintering. Several perovskites have been thus far attempted to be cold sintered [24–33], but only few publications report successful sintering without the need to post-anneal to significantly densify the material [34–40]. The transient liquids that resulted in sufficiently dense perovskites rely on hydroxide compounds, where two arguments can be considered for pressure-dissolution being effective: (1) strongly basic environment with solutions of dissolved hydroxides (i.e., low pH), and (2) liquid phase formed by melting of hydroxides at elevated temperatures (e.g., eutectic point of NaOH/KOH at ~170 °C [41]). $BaTiO_3$ nanopowders, for example, were densified to above 95 % relative density by cold sintering with NaOH/KOH eutectic mixture at 520 MPa and 300 °C [34], as well as with $Ba(OH)_2$*8 H_2O, which forms a solution above ~80 °C upon crystal-bound water release, at 350 MPa and >150 °C [36]. Utilizing a mixture of $Ba(OH)_2$ and TiO_2 nanoparticles, cementation of $BaTiO_3$ powders was also reported, with the need to post-anneal the ceramics [24], and tests of reactive cold sintering with $Ba(OH)_2$*8 H_2O and H_2TiO_3 nanoparticles as the source of $BaTiO_3$, yielded the formation of nanograined ceramics [38]. In some of these cases, $BaCO_3$ secondary phase had formed during sintering [36]. Attempts with other added compounds as transient liquids were published for different perovskite compounds, e.g., $Pb(NO_3)_2$ for $PbZrTiO_3$ [25], $Bi(NO_3)_3$, NaOH and TiO_2 for $Na_{0.5}Bi_{0.5}TiO_3$ [26], $SrCl_2/TiO_2$ for $SrTiO_3$ [27], CH_3COOH for $K_{0.5}Na_{0.5}NbO_3$ [31], $Sr(OH)_2$*8 H_2O for Sr-doped $BaTiO_3$ [35], $Ba(OH)_2$*8 H_2O–$Zr(OH)_4$ mixture for $BaZrO_3$ [39], or just water for $Na_{0.5}Bi_{0.5}TiO_3$- and $K_{0.5}Na_{0.5}NbO_3$-based solid solutions [32,33]. However, in all these examples only the cementation happened with no pressure-dissolution process, resulting in too low densities and/or limited functional properties, so the samples had to be additionally annealed at temperatures above ~900 °C for several hours.

While different procedures and transient liquids were tested so far for perovskites, it seems that molten hydroxides (NaOH/KOH) yield the most effective pressure-dissolution process, causing etching of the particles' surface, facilitating particle cohesion and densification of ceramics. To date, however, it remains unclear how exactly the hydroxide melts aid the sintering of perovskites beside etching their surface, how they recombine the perovskite surface bonds, whether they dissociate and form complexes, promote surface reactions, and/or diffuse into the matrix [42]. The latter may lead to undesired impurities in the materials, thus, there is a need to test and understand the effects of other possible compounds as sintering aids.

This study aims at understanding the influence of different TLP compounds on the CSP of the BFO perovskite, which to our knowledge was not attempted before. We utilized alkali hydroxides (KOH and/or NaOH) and urea (CH_4N_2O), which either leach out the metallic ions from the powder, or act as mineralizers [43,44]. It is anticipated that leaching further allows migration of metallic species from matrix to the inter-grain regions where they tend to precipitate, aid in adhesion of the BFO particles and thereby promote the sintering process. We studied how early precipitation of species in the form of secondary phases impedes densification and influences materials' functionality. By utilizing the eutectic mixture of NaOH/KOH in aqueous solution, similar to the studies performed on $BaTiO_3$ [34], we expect to efficiently sinter the material by dissolving the grains' surface and squeezing out the dissolved species from the system, limiting any secondary phase precipitation and promoting the densification process. We thus anticipate to obtain high-density and high-quality single-phase BFO with above-micron size grains and decent ferroelectric properties in comparison to conventionally sintered ceramics.

2. Experimental

The initial BFO powders, synthesized with 0.1 wt% of Co to limit conductivity, were prepared as described in reference;[4] particle size distributions of two BFO powder batches utilized for this study are given in Figure S1 of the Supplementary information. To carry out the cold sintering of BFO powders, we used as the TLP different additives and solvents, as specified in Table 1. For comparison to the cold-sintered samples, a conventionally-sintered BFO ceramics was prepared from the same calcined powder, sintered at 800 °C for 4 h.

Solutions were prepared from raw pellets of NaOH from Merck (97+% purity) and KOH from Alfa Aesar (85+% purity), dried prior to weighing. Mixing of 0.6 g of the BFO powder and the added solutions was carried out manually in a mortar for 3–5 minutes. The actual solvent concentrations in samples 1–3 were higher than reported in Table 1 as the ethanol partially evaporated during mixing. The moist powders were placed into pressing/heating dies. After increasing the uniaxial pressure to 635 MPa, the powders were subsequently heated with a heating rate of 17 °C/min to 300 °C for 3 hours. After sintering in an 8 mm diameter die, the pellets dimensions were 8 mm x ~1.8 mm thickness. For materials characterization, the sintered samples were dried in vacuum drier at 80 °C for 12 hours.

Structure and composition of the cold-sintered BFO samples were analysed by X-ray powder diffraction (XRD; X'Pert PRO MPD, PANalytical, Almelo, The Netherlands), Fourier-transform infrared spectroscopy (FTIR; Perkin Elmer Spectrum 100, Waltham, MA, USA), and scanning electron microscopy at 5 kV in backscattered mode (SEM; for imaging Jeol ltd., Tokyo, Japan was used; and for energy-dispersive X-ray spectroscopy (EDS) studies, Verios 4 G HP, Thermo Fisher Scientific, Waltham, USA, equipped with EDS Aztec Live Ultim Max SDD, Oxford Instruments, High Wycombe, UK was used). Polarization and strain with applied AC electric field at 1, 10 and 100 Hz were measured by the Aixacct measurement system (AixACCT Systems GmbH, Aachen, Germany) with a laser interferometer (model SP-S, SIOS Messtechnik GmbH, Ilmenau, Germany). The protocol of measurement was such that the field was gradually increased (sine waveform applied every 10 kV/cm until sample breakdown), with changing frequency from 100 Hz to 10 Hz to 1 Hz at each field. For comparison to the conventionally-sintered sample measurements at fixed frequency of 10 Hz with increasing field were performed. The permittivity and dielectric losses versus frequency were measured by LCR meter (Hewlett Packard, Tokyo, Japan). The current density was measured within the range ±1 kV/cm using a Keithley 237 high voltage source measuring unit (Keithley Instruments, Ohio, USA). The specific DC electrical conductivity was determined from the slope of trendline of the current-density-electric-field response.

3. Results and discussion

We present herein a detailed microstructural analysis of the BFO ceramics (with 0.1 wt% of Co), cold-sintered at 300 °C and 635 MPa with different additives (Table 1), and discuss the effects of the TLPs added or formed during sintering on the quality of sintered ceramics. Fig. 1 shows SEM images of ceramics obtained from the BFO powder with added solutions of NaOH-ethanol (Fig. 1a), KOH-ethanol (Fig. 1b), NaOH-KOH-ethanol (Fig. 1c), NaOH-urea-water (Fig. 1d), KOH-urea-water (Fig. 1e), NaOH-KOH-urea-water (Fig. 1f), NaOH-water (Fig. 1g), KOH-water (Fig. 1h), and NaOH-KOH-water (Fig. 1i). The results demonstrate that undesired secondary phases formed in the samples with added ethanol and urea. Two types of secondary phases, grown in the inter-grain spaces are observed: Bi-rich phase with plate-like morphology (bright-grey colour, indicated by black arrows in Fig. 1a-f), and numerous nm-sized Fe-rich precipitates (dark-grey colour; see also enlarged view and composition analysis of both types of secondary phases in Figure S2 of Supplementary information). No significant secondary phases were observed in the samples cold-sintered using aqueous solution with hydroxides (Fig. 1g-i).

The relative densities of samples in Fig. 1 were measured and calculated based on several SEM micrographs to be between 80 % and 90 % for samples with NaOH and/or KOH and ethanol, and for the sample with NaOH-urea-water. Slightly higher densities of ~92 % were observed for samples with KOH-urea and KOH-NaOH-urea dissolved in

Table 1
Specifications of additives and solvents added to the calcined BFO powders for the presented cold sintering study. The given liquid quantities are for 0.6 g of BFO powder per pellet.

Sample №	Sample name	Additive concentration	Solvent (ratio in ml)	Liquid volume	wt% of OH^-	wt% of additives	vol% of OH^-	vol% of additives
1	NaOH-EtOH	0.78 mol/l NaOH	EtOH:H_2O = 5:1	0.64 ml	3.2 %	3.2 %	11.5 %	11.5 %
2	KOH-EtOH	0.5 mol/l KOH	EtOH:H_2O = 5:1	0.59 ml	2.8 %	2.8 %	10.0 %	10.0 %
3	NaOH-KOH-EtOH	0.62 mol/l NaOH:KOH=1:1	EtOH:H_2O = 5:3	0.48 ml	2.3 %	2.3 %	8.4 %	8.4 %
4	NaOH-urea	4.8 mol/l NaOH:urea=1:1	H_2O	0.06 ml	0.9 %	2.3 %	3.3 %	11.4 %
5	KOH-urea	4.2 mol/l KOH:urea=1:1	H_2O	0.06 ml	1.1 %	2.3 %	4.0 %	11.0 %
6	NaOH-KOH-urea	4.5 mol/l NaOH:KOH: urea=1:1:1	H_2O	0.06 ml	1.4 %	2.3 %	5.2 %	10.4 %
7	NaOH-water	18.0 mol/l NaOH	H_2O	0.05 ml	5.7 %	5.7 %	19.0 %	19.0 %
8	KOH-water	12.9 mol/l KOH	H_2O	0.05 ml	5.7 %	5.7 %	19.1 %	19.1 %
9	NaOH-KOH	7.6 mol/l NaOH:KOH=1:1	H_2O	0.05 ml	3.0 %	3.0 %	10.7 %	10.7 %

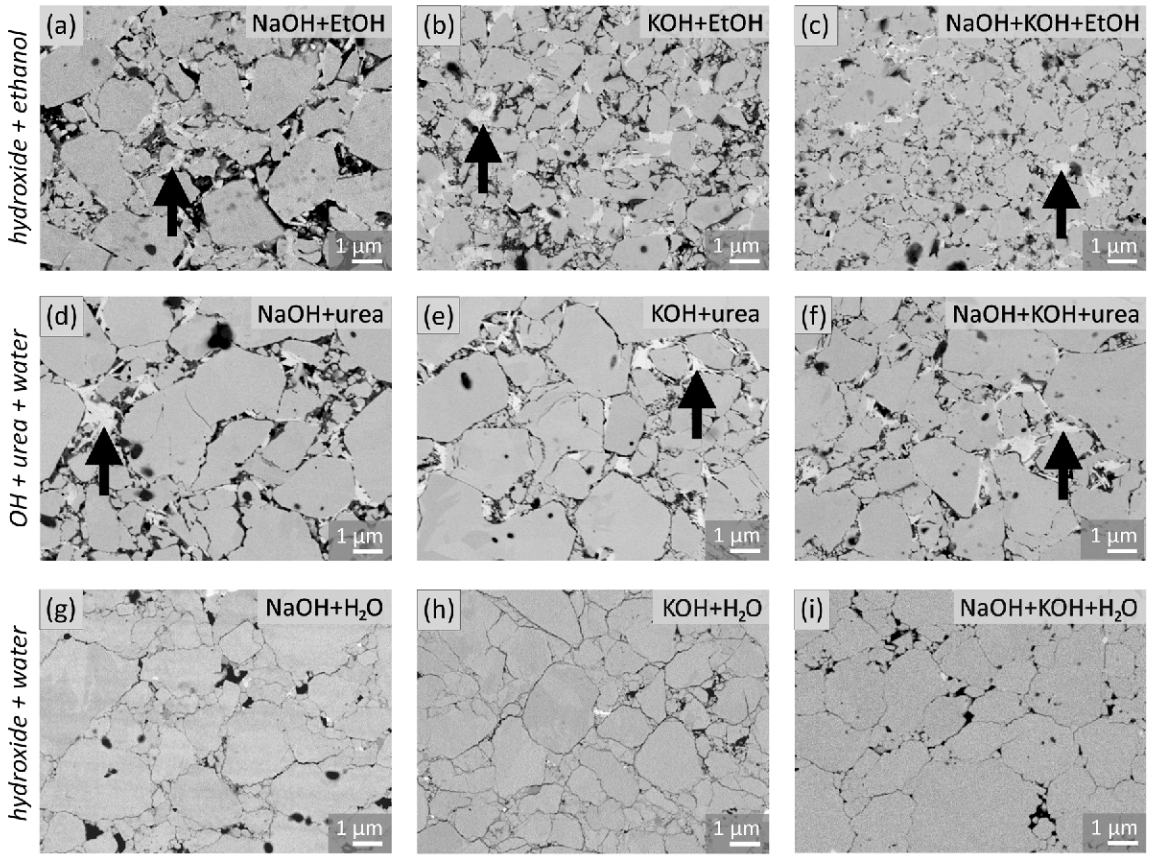

Fig. 1. Backscattered-electron SEM images of BFO ceramics, cold-sintered at 300 °C and 635 MPa for 3 h, using different solutions as sintering aids: (a) NaOH-ethanol; (b) KOH-ethanol; (c) NaOH-KOH-ethanol; (d) NaOH-urea-water; (e) KOH-urea-water; (f) NaOH-KOH-urea-water; (g) NaOH-water; (h) KOH-water; (i) NaOH-KOH-water. Black arrows indicate Bi-rich secondary phases at inter-grain space that mainly appear as plates or rods. Black regions are either pores, remains of additives or Na/K-based phases grown on the surface, or Fe-rich precipitates at grain boundaries (dark-grey).

water. Samples with hydroxides and water showed the highest relative densities of 93–96 %. While the matrix grains in samples with secondary phases (Fig. 1a-f) show little direct contacts with the neighbouring grains, mainly due to pores and secondary phases at the grain boundaries, we can still observe curved and interlocking grain boundaries, which directly indicate an effective pressure-dissolution process required for the chemical compaction of ceramics [22]. These microstructural features are more obvious in samples with both NaOH and KOH added (Fig. 1c and f; see also enlarged view of etched boundaries in Figure S3 of Supplementary information). The best compaction process, however, is achieved in samples with hydroxides and water, primarily due to no secondary phases formed, especially with higher amounts of NaOH in water (Fig. 1g), as well as the eutectic mixture of NaOH and KOH (Fig. 1i). The sample with just KOH-water (Fig. 1h) is also well compacted, but the boundaries are less etched and the grains appear to have some unhealed cracks. All three samples with added aqueous solution of hydroxides (Fig. 1g-i) show etched grain boundaries which allows better compaction due to strong interlocking grain-boundary contacts and interpenetrated grains, indicating a more efficient pressure-dissolution compaction process than with samples that possess secondary phases. Microstructural parameters of the samples in Fig. 1, along with some functional properties, are summarized in Table S1 of the Supplementary information.

We next analysed the secondary phases to understand the chemical

processes underway during the CSP. The plate-like Bi-rich phase (appearing as rods in cross-section in Fig. 1) was identified by SEM, XRD and FTIR analyses as the bismuth carbonate phase ($(BiO_2)CO_3$). Results of XRD, FTIR and EDS on selected samples are presented in Fig. 2. Reflections in XRD (Fig. 2a) and FTIR (Fig. 2b) that are marked by dashed lines point to the carbonate phase. FTIR spectrum of a pure Bi-carbonate (purchased from Alfa Aesar) is added for reference. Minor amounts of Bi_2O_3 or the Bi-rich sillenite phase (arrows in XRD, Fig. 2a) are unreacted remains from the BFO powder synthesis. The detailed EDS analysis of secondary phases, presented in Fig. 1c, was performed on the sample sintered with NaOH-ethanol (sample in Fig. 1a). The EDS mapping results confirmed that the Fe-rich phase is likely Fe-oxide (see green and cyan maps and arrows in the left panels in Fig. 2c, marking higher concentrations of Fe and O compared to the surrounding, respectively). This phase was not identified by XRD due to Fe being a lighter scatterer than Bi and its small quantities. Alternatively, the Fe-rich phase could also be goethite (FeO(OH)), similar to the formation of AlO(OH) [45], but we could not confirm it as hydrogen cannot be detected by EDS. Point spectra given in Figure S2 of Supplementary information further show remains of Na in the Fe-rich phase, indicating that NaOH decomposes and reacts with Fe, but the exact phase could not be determined. Substantial amounts of carbon were detected in the bright plate-like crystals (see magenta and red maps and arrows in the right panels in Fig. 2c, marking slightly higher concentrations of Bi and C compared to the surrounding, respectively), linking the bright-grey phase with Bi-carbonate, as confirmed by XRD. The Fe- and Bi-rich phases are intergrown, which points to their simultaneous precipitation. However, growth of the Bi-carbonate crystals seems to be substantial compared to the nanosized Fe-precipitates.

The Bi-carbonate phase is suggested to form as a result of leaching of ions from the BFO matrix, and their subsequent reaction with carbon-containing compounds, the source being organic compounds – ethanol and urea. It was observed that the strong bases act corrosively on the BFO particles/grains (see in Figure S4 of Supplementary information the microstructures of ceramics with increasing NaOH–EtOH content, leading to the dissolution of whole matrix grains and increased porosity, and the formation of significant amounts of the Bi-rich phase that eventually floods the grains). It is further anticipated that at the sintering temperature a thin layer of ethanol adsorbed on the particles forms hydrogen carbonate ions (HCO_3^{1-}) that during sintering bind with the leached metal cations from the matrix (Bi^{3+}, Fe^{3+}), causing an irreversible formation of Bi-carbonate and precipitation of Fe-oxide nanoparticles. It is also plausible that NaOH/KOH partially reacts with ethanol and forms Na/K ethoxide ($CH_3CH_2ONa^{1-}$), which decomposes around 300 °C, producing CO_2 [46,47] that stays trapped in the intergranular space, forming carbonates. Formation of secondary phases eventually stops the matrix dissolution process and with that the mechanical and chemical compaction of the ceramics [23], which leads to higher porosities of the ceramics with secondary phases, even up to 25 % in the case of NaOH content of 7.7 wt% (measured from microstructure images; this sample is presented in Fig. S4e of the Supplementary information).

Similar secondary-phase composition in BFO as with added hydroxides and ethanol was also observed when urea together with hydroxides was utilized as the TLP (Fig. 1d–f). This suggests that urea, which normally decomposes above 160–180 °C into ammonia and isocyanic acid and in contact with water releases CO_2, reacted with Bi^{3+} and formed the Bi-carbonate. Another possible path is via hydrolytic

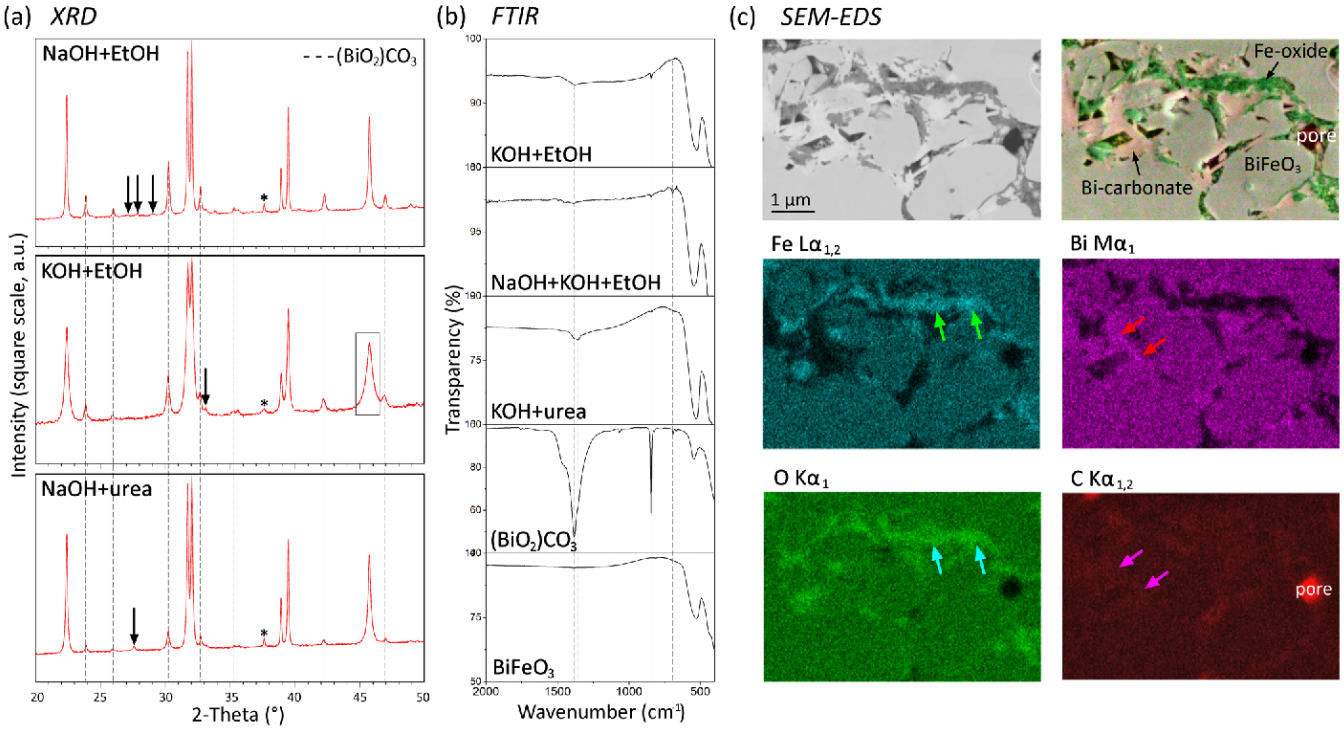

Fig. 2. XRD results (a), FTIR spectra (b) and SEM-EDS mapping (c) of selected cold-sintered BFO samples. (a) Comparison of XRD spectra of samples sintered with NaOH-ethanol (top), KOH-ethanol (middle) and NaOH-urea-water (bottom); all show four major reflections from the BFO matrix, including superstructure reflection marked with *, confirming the *R3c* perovskite symmetry. Dashed vertical lines connect reflections that were identified as Bi-carbonate ($(BiO_2)CO_3$). The black square indicates broadening of perovskite peaks in the sample with smaller grain size. Arrows point to unresolved peaks (Bi-rich phases). (b) FTIR spectra from three selected samples; Bi-carbonate powder and the initial BFO powder spectra are added for reference (bottom). The FTIR spectra confirm the presence of carbonate phases (follow vertical dashed lines). (c) EDS maps of BFO ceramics, cold-sintered with NaOH–EtOH solution. Three phases are observed in the backscattered SEM image (top left) which are identified from maps of emitted X-rays, characteristic of Fe (cyan, middle left), Bi (magenta, middle right), O (green, bottom left) and C (red, bottom right) as the BFO matrix, Bi-carbonate plates and Fe-oxide precipitates (marked and coloured in top right panel). Arrows point to areas of higher concentrations of each element.

decomposition of urea with BFO acting as a catalyst, again leading to CO_2 release and its reaction with Bi^{3+} [48].

The samples sintered with organic additives (ethanol/urea) that showed secondary phase formation and lower densities, as well as samples with higher quantities of added hydroxides contained trapped remains of hydroxides, which contributed to growth of crystals on the surface of pellets that were exposed to air (see dark grey/black patches in microstructures in Fig. 1; see also Figure S5 in Supplementary information with identified Na/K-carbonate crystals on the polished surfaces). This makes the samples highly hygroscopic and electrically conductive (when exposed to air for a longer time, droplets formed on the samples' surface).

Strongly etched grain boundaries, no secondary phases induced and relatively high densities were observed in the case of NaOH-water solution used (Fig. 1g). This proved that it was the organic compounds added in the solution that reacted with the dissolved matrix species and caused the formation of secondary phases in BFO ceramics. However, after a preliminary test with mixture of BFO powder and NaOH-water solution that was dried prior to sintering to see the effect of possible NaOH melt as an effective TLP rather than a strong base solution on the sintering process (NaOH melts at ~320 °C at ambient conditions), we again obtained secondary phases and relatively high porosity (see Figure S6 of the Supplementary material showing significant amounts of Fe-precipitates and Bi-oxide phase (rather than the carbonate), both also containing Na). This observation raised questions about the solubility versus melting of the surface of BFO in the presence of hydroxides during cold sintering. Regardless, it appears that sufficient amount of TLP present at the time of dissolution/melting is crucial to drive away the dissolved/molten species rather than their immediate precipitation. This in turn also limits any grain growth during sintering.

Since samples with NaOH-water and KOH-water were well sintered only at sufficiently high hydroxide quantities, causing problems with sintered samples becoming moist in air, our final sintering experiment was done with NaOH-KOH-water as a TLP (i.e., the eutectic mixture of NaOH:KOH = 1:1 dissolved in water). The effects of the molten hydroxides on the sintering and properties of other perovskite ceramics was already discussed previously [34,37,40]. Sintering with NaOH-KOH-water yielded a dense (~96 % relative density) single-phase BFO ceramics (Fig. 1i). This indicates high dissolution/melting strength of the eutectic mixture as TLP that likely acts as an etching agent and also transport medium, squeezing out of the dissolved/melted material by the applied pressure, rather than a reactive reagent forming complexes for precipitation of species.

We next compare in Fig. 3 the electrical and electromechanical properties of the BFO sample sintered with NaOH-KOH-water (presented in Fig. 1i) with the samples sintered with NaOH-ethanol (sample with 3.2 wt% NaOH, presented in Fig. 1a and Fig. S4b, and sample with 7.7 wt% NaOH, presented in Fig. S4e of the Supplementary information), to understand the influence of secondary phases induced during sintering. It is observed that high NaOH-ethanol content, which leads to secondary phase formation and high porosity, contributes to lower dielectric permittivity, higher dielectric losses and increased current density (follow the grey lines in Fig. 3a-c) compared to samples sintered with low NaOH-ethanol content (orange lines) and NaOH-KOH-water (black lines). While the latter two samples seem comparable, current density appears higher in the NaOH-ethanol sample (see orange dots and trendline compared to black in Fig. 3c inset), which could potentially be attributed to the secondary phase content, lower relative density, and/or point defects created by chemical reactions between the NaOH-ethanol solvent and BFO.

Comparison of the polarization–electric-field (*P*–*E*) loops measured at 190 kV/cm and frequencies of 100 Hz, 10 Hz and 1 Hz (Fig. 3d) of the two samples indicate that there is a larger contribution from electrical conductivity to the measured polarization in the NaOH-ethanol sample (see orange loops with rounded loop tips and strongly enhanced remanent polarization at lower frequencies; i.e., opening of the loops)

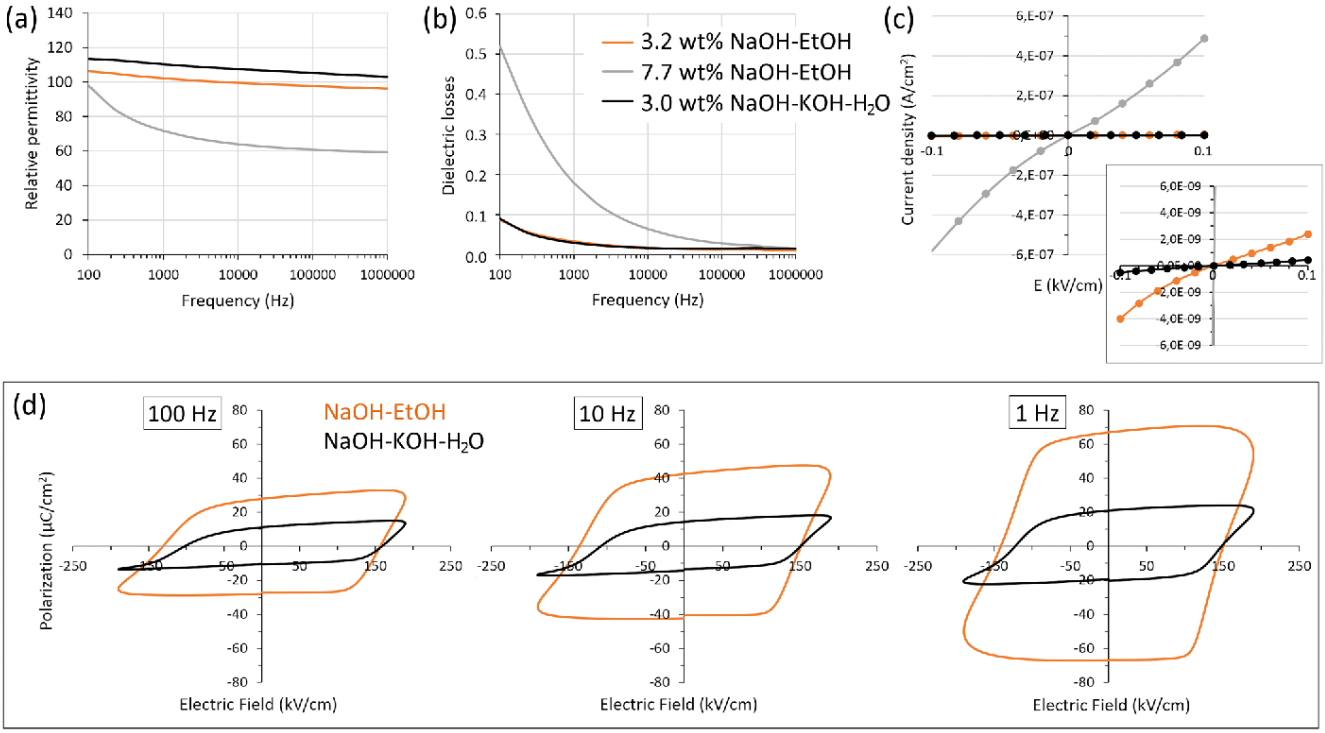

Fig. 3. (a) Relative permittivity vs. frequency, (b) dielectric losses vs. frequency, and (c) current density vs. electric field plots of BFO ceramics cold-sintered with 3.2 wt% NaOH-ethanol (orange lines), 7.7 wt% NaOH-ethanol (grey lines), and 3 wt% NaOH-KOH in aqueous solution (black). Inset in (c) shows an increased scale of current density so present differences between 3.2 and 7.7 wt% NaOH-ethanol BFO samples. (d) Polarization versus electric field loops of BFO samples cold-sintered with 3.2 wt% NaOH-ethanol (orange) and with 3 wt% NaOH-KOH-water (black), measured at 190 kV/cm at 100, 10 and 1 Hz.

compared to the NaOH-KOH-water sample (black loops), which is consistent with the dielectric and current-density–electric-field behaviour. While strong frequency dependence of the response is characteristic for conventionally-sintered BFO, attributed to the defect–domain-wall interactions [49], it is much more pronounced in the NaOH-ethanol cold-sintered BFO, while fairly insignificant in the sample cold-sintered with NaOH-KOH-water. The difference is attributed to the higher level of conductivity of the NaOH-ethanol sample. Both samples clearly exhibit shifted *P–E* loops along the horizontal (field) axis, suggesting internal bias and thus the existence of preferentially aligned defects, acting as pinning centres for domain walls [50]. All measurements were obtained on the as-sintered BFO without any post-annealing step, which is needed in some cold-sintered samples for defect relaxation or perovskite re-oxidation [51].

We finally present in Fig. 4a comparison of the microstructures and the functional properties (polarization–electric field loops) of the BFO ceramics cold-sintered with NaOH-KOH-water (Fig. 4a-c; microstructure already presented in Fig. 1i) and the conventionally-sintered BFO ceramics from the same calcined powder (Fig. 4d-f). Grain size in cold-sintered ceramics is ~1 μm on average, while the conventionally-sintered ceramics possesses larger grains, with 5–10 μm size. Grain boundaries are observed to be significantly different in the two samples; strongly curved boundaries with interlocking grains are found in cold-sintered ceramics, while in the case of conventional BFO the boundaries are straight. The latter sample also shows some mullite and sillenite secondary phases, and intragranular trapped pores (marked in Fig. 4d). The electrical field was applied to the samples in two different ways (described in experimental) to emphasize the role of defects in both BFO ceramics. Figs. 4b and 4e show *P–E* loops at 10 Hz with increasing field and frequency cycling (subsequent measurements at 100, 10 and 1 Hz at each field), while Fig. 4c and f show loops at increasing field and fixed frequency of 10 Hz. With cycling the frequency both samples exhibit a square-shaped *P–E* loop, with the major difference being larger remanent polarization achieved in the conventional sample (P_r of ~32 μC/cm^2 at 150 kV/cm compared to P_r of ~19 μC/cm^2 at 200 kV/cm at 10 Hz). The larger remanent polarization could primarily be assigned to the larger grains in conventional ceramics. The *P–E* loops measured at fixed frequency of 10 Hz for both samples show significantly supressed remanent polarization, indicating the role of defects, pinning the domain walls. In all cases (Fig. 4b, c, e, and f) there is a threshold field that needs to be overcome to switch the dipoles, unpin the domain walls and open up the loops (~150 kV/cm for cold-sintered BFO and ~100 kV/cm for conventional BFO). The pinning centres in conventionally sintered BFO were previously identified as Bi and O vacancies, as well as *p*-type charges related to oxidized Fe^{4+} states [4,52]. Other pinning centres may also be present in cold-sintered samples, such as deformation defects caused by applied pressure (e.g., lattice dislocations), which were previously found in the cold-sintered KNN perovskite [40,51]. Comparing the magnitude of applied electric field in cold-sintered BFO (with NaOH-KOH-water) with that applied to conventional BFO ceramics we find significantly improved dielectric breakdown strength in cold-sintered ceramics (field applied without breakdown up to 200 kV/cm). This can be assigned to smaller grains in the cold-sintered ceramics with broad grain size distribution, strongly curved and interlocking grain boundaries, and mechanically deformed crystal lattice (as was previously observed in cold-sintered KNN perovskite [40,51] due to applied pressure during sintering) that may cause dislocation hardening [53]. Finally, the cold sintered sample exhibits a typical butterfly-shaped strain–electric-field loop with peak-to-peak strain $S_{p\text{-}p}$ of ~0.13 % (see Fig. 4b inset), which is comparable to conventional BFO ceramics [49].

Results presented in this paper led us to conclude that cold sintering by using appropriate TLPs is a viable way to obtain BFO ceramics at 300 °C with functional properties comparable or with additional tailoring even superior to the conventionally sintered BFO, with stable remanent polarization (less influence of electrical conductivity) and high

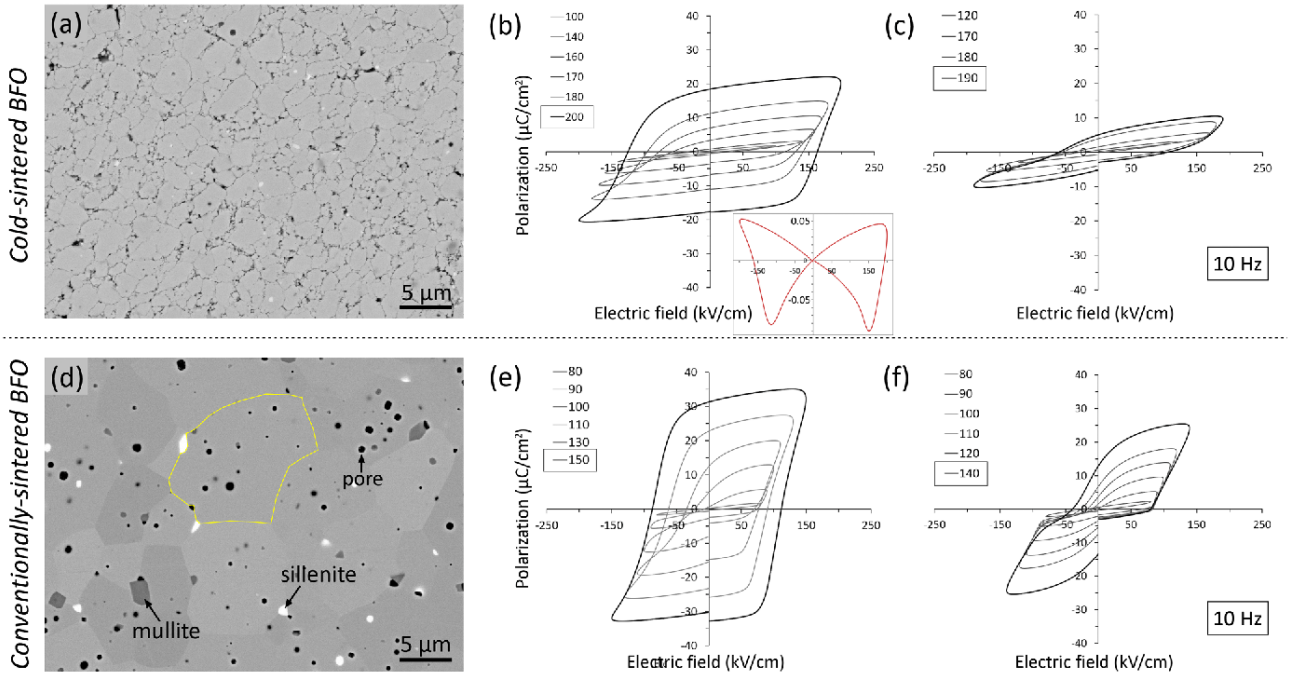

Fig. 4. Comparison of cold-sintered BFO with NaOH-KOH-water (a–c) with conventionally-sintered BFO ceramics (d–f). SEM images of typical microstructures of (a) cold-sintered BFO ceramics and (d) conventionally-sintered BFO ceramics show the differences in grain sizes and curvature of grain boundaries. Secondary phases and trapped pores are pointed in (d); grain boundaries are marked with yellow lines. (b,e) Polarization versus electric-field loops, measured with increasing field and frequency-cycling at each field (at 100 Hz, 10 Hz and 1 Hz), are presented at 10 Hz for (b) cold-sintered BFO and (e) conventional BFO. Inset in (b) shows a strain versus electric-field loop of cold-sintered BFO, measured at 0.1 Hz. (c,f) Polarization versus electric-field loops, measured with increasing field at fixed frequency of 10 Hz for (c) cold-sintered BFO and (f) conventional BFO, both showing significantly suppressed remanent polarization.

dielectric breakdown strength (samples sustaining applied field on the level of 200 kV/cm). Further improvements to the microstructure of BFO are foreseen to increase the currently obtained remanent polarization values, e.g., larger initial particle sizes. While NaOH-KOH mixture dissolved in water turned out to be the optimal sintering aid, we believe that other compounds are worth exploring as they can also contribute to high compaction and obtaining high quality ceramic samples.

4. Conclusions

In this contribution we provide insights into the chemical and phase composition of cold-sintered BFO ceramics and discuss the effects of various transient liquids added to the BFO powder to facilitate the cold sintering process. We found that decomposition of the additives prior or during the CSP leads to a reaction between the dissolved species from the matrix and the solvent-based decomposition products. This reaction results in secondary-phase formation, lower relative densities and poor ceramic properties, while still facilitating sintering. We have specifically observed the formation of Bi-carbonate and Fe-oxide when the additives and solvent are not appropriately selected and contain organic species. Our findings imply that congruent melting of the matrix material, the absence of decomposition of the sintering aids, and non-reactivity of the TLP with the leached-out species are crucial for obtaining single-phase cold-sintered perovskite ceramics, characterized by clean grain boundaries and good ferroelectric properties. We obtained BFO ceramics with remanent polarization P_r of ~19 μC/cm^2 from P–E loops measured at 200 kV/cm at 10 Hz, and a typical butterfly-shaped strain-electric field loop with peak-to-peak strain $S_{p\text{-}p}$ of ~0.13 %, without any post-annealing procedure. The presented results may serve as guidance for optimizing the cold sintering of similar perovskite materials.

CRediT authorship contribution statement

Samir Salmanov: Writing – original draft, Visualization, Validation, Methodology, Investigation, Formal analysis. **Katarina Žiberna:** Writing – review & editing, Investigation, Formal analysis. **Minghai Yao:** Writing – original draft, Investigation, Formal analysis. **Danjela Kuščer:** Writing – review & editing, Validation, Supervision, Conceptualization. **Tadej Rojac:** Writing – review & editing, Validation, Supervision. **Mojca Otoničar:** Writing – review & editing, Visualization, Validation, Supervision, Project administration, Methodology, Investigation, Funding acquisition, Formal analysis, Conceptualization. **Brahim Dkhil:** Writing – review & editing, Funding acquisition. **Meryem Lachhab:** Investigation, Formal analysis. **Barbara Malič:** Writing – review & editing, Supervision, Resources, Funding acquisition.

Declaration of Competing Interest

The authors declare that they have no known competing financial interests or personal relationships that could have appeared to influence the work reported in this paper.

Acknowledgements

This research was funded by the Slovenian Research Agency (grant numbers J2–2508, J2–50077, P2–0105, and young researcher's program). Slovenian-French Proteus mobility grant is acknowledged (PR-12702). Bor Arah from Center for electron microscopy and microanalysis at JSI is acknowledged for help with performing EDS mapping. Campus France is acknowledged for the Proteus mobility grant No. 50353YJ and ANR French Research Agency for Funding the project 23-CE05-0012.

Appendix A. Supporting information

Supplementary data associated with this article can be found in the online version at doi:10.1016/j.jeurceramsoc.2024.116846.

References

[1] V.V. Shvartsman, W. Kleemann, R. Haumont, J. Kreisel, Large bulk polarization and regular domain structure in ceramic BiFe O3, Appl. Phys. Lett. 90 (2007) 3–6, https://doi.org/10.1063/1.2731312.
[2] J.B. Neaton, C. Ederer, U.V. Waghmare, N.A. Spaldin, K.M. Rabe, First-principles study of spontaneous polarization in multiferroic BiFeO 3, Phys. Rev. B - Condens. Matter Mater. Phys. 71 (2005) 1–8, https://doi.org/10.1103/PhysRevB.71.014113.
[3] G. Catalan, J.F. Scott, Physics and applications of bismuth ferrite, Adv. Mater. 21 (2009) 2463–2485, https://doi.org/10.1002/adma.200802849.
[4] M. Makarovic, N. Kanas, A. Zorko, K. Ziberna, H. Ursic, D.R. Smabraten, S. M. Selbach, T. Rojac, Tailoring the electrical conductivity and hardening in BiFeO3 ceramics, J. Eur. Ceram. Soc. 40 (2020) 5483–5493, https://doi.org/10.1016/j.jeurceramsoc.2020.06.037.
[5] T. Rojac, M. Makarovic, J. Walker, H. Ursic, D. Damjanovic, T. Kos, Piezoelectric response of BiFeO3 ceramics at elevated temperatures, Appl. Phys. Lett. 109 (2016), https://doi.org/10.1063/1.4960103.
[6] G. Catalan, J. Seidel, R. Ramesh, J.F. Scott, Domain wall nanoelectronics, Rev. Mod. Phys. 84 (2012) 119–156, https://doi.org/10.1103/RevModPhys.84.119.
[7] N.A. Spaldin, R. Ramesh, Advances in magnetoelectric multiferroics, Nat. Mater. 18 (2019) 203–212, https://doi.org/10.1038/s41563-018-0275-2.
[8] W. Amdouni, M. Fricaudet, M. Otoničar, V. Garcia, S. Fusil, J. Kreisel, H. Maghraoui-Meherzi, B. Dkhil, BiFeO3 nanoparticles: the "holy-grail" of piezo-photocatalysts? Adv. Mater. 35 (2023) 1–10, https://doi.org/10.1002/adma.202301841.
[9] M. Valant, A.K. Axelsson, N. Alford, Peculiarities of a solid-state synthesis of multiferroic polycrystalline BiFeO3, Chem. Mater. 19 (2007) 5431–5436, https://doi.org/10.1021/cm071730.
[10] S.M. Selbach, M.A. Einarsrud, T. Grande, On the thermodynamic stability of BiFeO3, Chem. Mater. 21 (2009) 169–173, https://doi.org/10.1021/cm802607p.
[11] T. Rojac, A. Bencan, B. Malic, G. Tutuncu, J.L. Jones, J.E. Daniels, D. Damjanovic, BiFeO3 ceramics: processing, electrical, and electromechanical properties, J. Am. Ceram. Soc. 97 (2014) 1993–2011, https://doi.org/10.1111/jace.12982.
[12] T. Rojac, A. Bencan, G. Drazic, N. Sakamoto, H. Ursic, B. Jancar, G. Tavcar, M. Makarovic, J. Walker, B. Malic, D. Damjanovic, Domain-wall conduction in ferroelectric BiFeO 3 controlled by accumulation of charged defects, Nat. Mater. 16 (2017) 322–327, https://doi.org/10.1038/nmat4799.
[13] J. Seidel, L.W. Martin, Q. He, Q. Zhan, Y.H. Chu, A. Rother, M.E. Hawkridge, P. Maksymovych, P. Yu, M. Gajek, N. Balke, S.V. Kalinin, S. Gemming, F. Wang, G. Catalan, J.F. Scott, N.A. Spaldin, J. Orenstein, R. Ramesh, Conduction at domain walls in oxide multiferroics, Nat. Mater. 8 (2009) 229–234, https://doi.org/10.1038/nmat2373.
[14] A. Bencan, G. Drazic, H. Ursic, M. Makarovic, M. Komelj, T. Rojac, Domain-wall pinning and defect ordering in BiFeO3 probed on the atomic and nanoscale, Nat. Commun. 11 (2020) 1–9, https://doi.org/10.1038/s41467-020-15595-0.
[15] N. Masó, A.R. West, Electrical properties of Ca-doped BiFeO 3 ceramics: From p-type semiconduction to oxide-ion conduction, Chem. Mater. 24 (2012) 2127–2132, https://doi.org/10.1021/cm300683e.
[16] R. Mazumder, D. Chakravarty, D. Bhattacharya, A. Sen, Spark plasma sintering of BiFeO3, Mater. Res. Bull. 44 (2009) 555–559, https://doi.org/10.1016/j.materresbull.2008.07.017.
[17] Z. Brankovic, D.L. Golic, A. Radojkovic, J. Cirkovic, D. Pajic, Z.M. Stanojevic, J. Xing, M. Radovic, G. Li, G. Brankovic, Spark plasma sintering of hydrothermally synthesized bismuth ferrite, Process. Appl. Ceram. 10 (2016) 257–264, https://doi.org/10.2298/PAC1604257B.
[18] E. Gil-González, A. Perejón, P.E. Sánchez-Jiménez, M.J. Sayagués, R. Raj, L. A. Pérez-Maqueda, Phase-pure BiFeO3 produced by reaction flash-sintering of Bi2O3 and Fe2O3, J. Mater. Chem. A. 6 (2018) 5356–5366, https://doi.org/10.1039/c7ta09239c.
[19] H. Guo, A. Baker, J. Guo, C.A. Randall, Cold sintering process: a novel technique for low-temperature ceramic processing of ferroelectrics, J. Am. Ceram. Soc. 99 (2016) 3489–3507, https://doi.org/10.1111/jace.14554.
[20] J.P. Maria, X. Kang, R.D. Floyd, E.C. Dickey, H. Guo, J. Guo, A. Baker, S. Funihashi, C.A. Randall, Cold sintering: current status and prospects, J. Mater. Res. 32 (2017) 3205–3218, https://doi.org/10.1557/jmr.2017.262.
[21] A. Ndayishimiye, M.Y. Sengul, T. Sada, S. Dursun, S.H. Bang, Z.A. Grady, K. Tsuji, S. Funahashi, A.C.T. van Duin, C.A. Randall, Roadmap for densification in cold sintering: Chemical pathways, Open Ceram. 2 (2020) 100019, https://doi.org/10.1016/j.oceram.2020.100019.
[22] A. Ndayishimiye, S.H. Bang, C.J. Spiers, C.A. Randall, Reassessing cold sintering in the framework of pressure solution theory, J. Eur. Ceram. Soc. 43 (2022) 1–13, https://doi.org/10.1016/j.jeurceramsoc.2022.09.053.
[23] D. Croizé, F. Renard, J.P. Gratier, Compaction and Porosity Reduction in Carbonates: A Review of Observations, Theory, Exp. (2013), https://doi.org/10.1016/B978-0-12-380940-7.00003-2.
[24] H. Guo, J. Guo, A. Baker, C.A. Randall, Hydrothermal-Assisted Cold Sintering Process: A New Guidance for Low-Temperature Ceramic Sintering, ACS Appl.

Mater. Interfaces 8 (2016) 20909–20915, https://doi.org/10.1021/acsami.6b07481.
[25] D. Wang, H. Guo, C.S. Morandi, C.A. Randall, S. Trolier-McKinstry, Cold sintering and electrical characterization of lead zirconate titanate piezoelectric ceramics, APL Mater. 6 (2018), https://doi.org/10.1063/1.5004420.
[26] H.Q. Huang, J. Tang, J. Liu, Preparation of Na 0.5 Bi 0.5 TiO 3 ceramics by hydrothermal-assisted cold sintering, Ceram. Int. 45 (2019) 6753–6758, https://doi.org/10.1016/j.ceramint.2018.12.166.
[27] R. Boston, J. Guo, S. Funahashi, A.L. Baker, I.M. Reaney, C.A. Randall, Reactive intermediate phase cold sintering in strontium titanate, RSC Adv. 8 (2018) 20372–20378, https://doi.org/10.1039/c8ra03072c.
[28] S. Yang, C. Zuo, F. Du, L. Chen, W. Jie, X. Wei, Submicron Sr0.7Bi0.2TiO3 dielectric ceramics for energy storage via a two-step method aided by cold sintering process, Mater. Des. 225 (2023), https://doi.org/10.1016/j.matdes.2022.111447.
[29] L. Cong, W. Huajing, M. Jianzhang, D. Baoyu, W. Xiao, L. Tengfei, Z. Xinghua, Y. Xing, Effect of dwell time on cold sintering assisted sintering based highly transparent 0.9K0.5Na0.5NbO3-0.1LiBiO3 ceramics, J. Alloy. Compd. 826 (2020) 154249, https://doi.org/10.1016/j.jallcom.2020.154249.
[30] B. Deng, Y. Ma, T. Chen, H. Wang, J. Lin, C. Lin, X. Wu, C. Zhao, T. Lin, M. Gao, X. Zheng, C. Fang, Elevating electrical properties of (K, Na)NbO3 ceramics via cold sintering process and post-annealing, J. Am. Ceram. Soc. 105 (2022) 461–468, https://doi.org/10.1111/jace.18103.
[31] J. Jun Lan, X. Ming Chen, M. Dan Liu, L. Na Liu, H. Li Lian, K0.5Na0.5NbO3 ceramics fabricated by combining cold sintering with annealing in air atmosphere or low pO2 atmosphere, J. Am. Ceram. Soc. 106 (2023) 6826–6836, https://doi.org/10.1111/jace.19316.
[32] L. Liu, X. Chen, J. Ma, J.-B. Lu, H.-L. Lian, W. Deng, Fabrication, microstructure, dielectric, and ferroelectric properties of (Bi0.5Na0.5)0.94Ba0.06TiO3 nanograined ceramics via cold-sintering-assisted sintering, Ceram. Int. 49 (2023) 12796–12804, https://doi.org/10.1016/j.ceramint.2022.12.145.
[33] H. Zubairi, F. Hussain, S. Sheikh, A.A. Shaikh, D. Wang, I.M. Reaney, Comparative study of cold assisted and conventional sintering of (1-2x) K0.5Na0.5NbO3-xBaTiO3-xBiFeO3 multiferroic ceramics, Mater. Sci. Eng. B. 296 (2023) 1–9, https://doi.org/10.1016/j.mseb.2023.116632.
[34] K. Tsuji, A. Ndayishimiye, S. Lowum, R. Floyd, K. Wang, M. Wetherington, J. P. Maria, C.A. Randall, Single step densification of high permittivity BaTiO3 ceramics at 300 °C, J. Eur. Ceram. Soc. 40 (2020) 1280–1284, https://doi.org/10.1016/j.jeurceramsoc.2019.12.022.
[35] T. Sada, Z. Fan, A. Ndayishimiye, K. Tsuji, S.H. Bang, Y. Fujioka, C.A. Randall, In situ doping of BaTiO3 and visualization of pressure solution in flux-assisted cold sintering, J. Am. Ceram. Soc. 104 (2021) 96–104, https://doi.org/10.1111/jace.17461.
[36] T. Sada, K. Tsuji, A. Ndayishimiye, Z. Fan, Y. Fujioka, C.A. Randall, High permittivity BaTiO3 and BaTiO3-polymer nanocomposites enabled by cold sintering with a new transient chemistry: Ba(OH)2•8H2O, J. Eur. Ceram. Soc. 41 (2021) 409–417, https://doi.org/10.1016/j.jeurceramsoc.2020.07.070.
[37] K. Tsuji, Z. Fan, S.H. Bang, S. Dursun, S. Trolier-McKinstry, C.A. Randall, Cold sintering of the ceramic potassium sodium niobate, (K0.5Na0.5)NbO3, and influences on piezoelectric properties, J. Eur. Ceram. Soc. 42 (2022) 105–111, https://doi.org/10.1016/j.jeurceramsoc.2021.10.002.
[38] N. Guo, H.Z. Shen, P. Shen, One-step synthesis and densification of BaTiO3 by reactive cold sintering, Scr. Mater. 213 (2022) 114628, https://doi.org/10.1016/j.scriptamat.2022.114628.
[39] H. Shen, N. Guo, P. Shen, Journal of the European Ceramic Society Synthesis and densification of BaZrO 3 ceramics by reactive cold sintering of Ba (OH) 2 · 8H 2 O-Zr (OH) 4 powders, J. Eur. Ceram. Soc. 43 (2022) 1–9, https://doi.org/10.1016/j.jeurceramsoc.2022.10.016.
[40] S. Salmanov, M. Koblar, B. Kmet, B. Malič, T. Rojac, D. Kuščer, M. Otoničar, Structure and electrical properties of cold-sintered strontium-doped potassium sodium niobate, J. Eur. Ceram. Soc. (2023) 4–11, https://doi.org/10.1016/j.jeurceramsoc.2023.07.069.
[41] H.W. Otto, R.P. Seward, Phase Equilibria in the Potassium Hydroxide-Sodium Hydroxide System, J. Chem. Eng. Data. 9 (1964) 507–508, https://doi.org/10.1021/je60023a009.
[42] A. Ndayishimiye, M.Y. Sengul, D. Akbarian, Z. Fan, K. Tsuji, S.H. Bang, A.C.T. Van Duin, C.A. Randall, Dynamics of the Chemically Driven Densification of Barium Titanate Using Molten Hydroxides, Nano Lett. 21 (2021) 3451–3457, https://doi.org/10.1021/acs.nanolett.1c00069.
[43] C.J. Tsai, C.Y. Yang, Y.C. Liao, Y.L. Chueh, Hydrothermally grown bismuth ferrites: Controllable phases and morphologies in a mixed KOH/NaOH mineralizer, J. Mater. Chem. 22 (2012) 17432–17436, https://doi.org/10.1039/c2jm33859a.
[44] J. Zhang, K. Huang, L. Yuan, S. Feng, Mineralizer effect on facet-controllable hydrothermal crystallization of perovskite structure YbFeO3 crystals, CrystEngComm 20 (2018) 470–476, https://doi.org/10.1039/c7ce01827d.
[45] K. Yamaguchi, S. Hashimoto, Effect of phase transformation in cold sintering of aluminum hydroxide, J. Eur. Ceram. Soc. 44 (2024) 2754–2761, https://doi.org/10.1016/j.jeurceramsoc.2023.12.054.
[46] K. Chandran, M. Kamruddin, P.K. Ajikumar, A. Gopalan, V. Ganesan, Kinetics of thermal decomposition of sodium methoxide and ethoxide, J. Nucl. Mater. 358 (2006) 111–128, https://doi.org/10.1016/j.jnucmat.2006.07.003.
[47] D. Williams, R.W. Bost, Reaction Products of Ethyl Alcohol and Sodium Hydroxide, J. Chem. Phys. 4 (1936) 251–253, https://doi.org/10.1063/1.1749831.
[48] A.N. Alexandrova, W.L. Jorgensen, Why urea eliminates ammonia rather than hydrolyzes in aqueous solution, J. Phys. Chem. B. 111 (2007) 720–730, https://doi.org/10.1021/jp066478s.
[49] T. Rojac, M. Kosec, D. Damjanovic, Large electric-field induced strain in BiFeO3 ceramics, J. Am. Ceram. Soc. 94 (2011) 4108–4111, https://doi.org/10.1111/j.1551-2916.2011.04861.x.
[50] T. Rojac, M. Kosec, B. Budic, N. Setter, D. Damjanovic, Strong ferroelectric domain-wall pinning in BiFeO3 ceramics, 074107-1–8, J. Appl. Phys. 108 (2010), https://doi.org/10.1063/1.3490249.
[51] K. Nakagawa, M. Iwasaki, Z. Fan, J.I. Roscow, C.A. Randall, The unusual case of plastic deformation and high dislocation densities with the cold sintering of the piezoelectric ceramic K0.5Na0.5NbO3, J. Eur. Ceram. Soc. 43 (2023) 4015–4020, https://doi.org/10.1016/j.jeurceramsoc.2023.02.057.
[52] G.L. Yuan, S.W. Or, Y.P. Wang, Z.G. Liu, J.M. Liu, Preparation and multi-properties of insulated single-phase BiFeO 3 ceramics, Solid State Commun. 138 (2006) 76–81, https://doi.org/10.1016/j.ssc.2006.02.005.
[53] L. Porz, A.J. Klomp, X. Fang, N. Li, C. Yildirim, C. Detlefs, E. Bruder, M. Höfling, W. Rheinheimer, E.A. Patterson, P. Gao, K. Durst, A. Nakamura, K. Albe, H. Simons, J. Rödel, Dislocation-toughened ceramics, Mater. Horiz. 8 (2021) 1528–1537, https://doi.org/10.1039/d0mh02033h.

Supplementary information

Impact of transient liquid phase on the cold sintering process of multiferroic $BiFeO_3$

Samir Salmanov,[a,b] Minghai Yao,[c,d] Katarina Žiberna,[a,b] Meryem Lachhab,[a,b,d] Brahim Dkhil,[d] Barbara Malič,[a,b] Tadej Rojac,[a,b] Danjela Kuščer,[a,b] Mojca Otoničar[a,b,*]

[a] Electronic Ceramics Department, Jozef Stefan Institute, Jamova cesta 39, 1000 Ljubljana, Slovenia
[b] Jozef Stefan International Postgraduate School, Jamova cesta 39, 1000 Ljubljana, Slovenia
[c] Huazhong University of Science and Technology, Wuhan, Hubei, China
[d] Université Paris-Saclay, CentraleSupélec, CNRS-UMR8580, 91190 Gif-sur-Yvette, France
* Corresponding author: Mojca Otoničar (mojca.otonicar@ijs.si), Electronic Ceramics Department, Jožef Stefan Institute, Jamova cesta 39, 1000 Ljubljana, Slovenia

PART 1: Particle size analysis

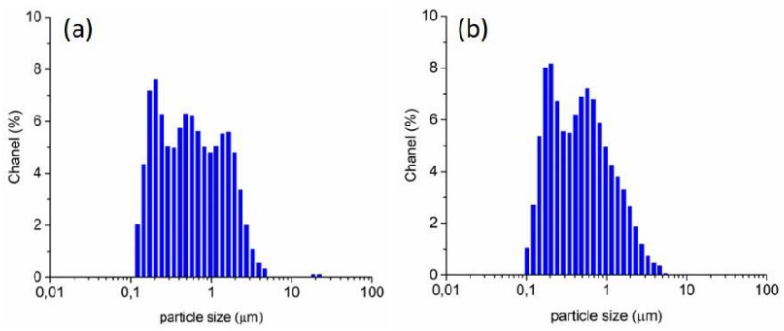

Figure S1: Particle size distribution of two batches of synthesized Co-doped $BiFeO_3$ (BFO) powders used for cold sintering. Higher amount of above-micron-sized particles from powder in (a) result in larger grains in the cold-sintered samples (see in Fig. 1a, 1d-1f of the main text), while powder presented in (b) gives cold-sintered samples with smaller grains on average (Fig. 1b, 1c).

PART 2: Microstructure and composition analysis

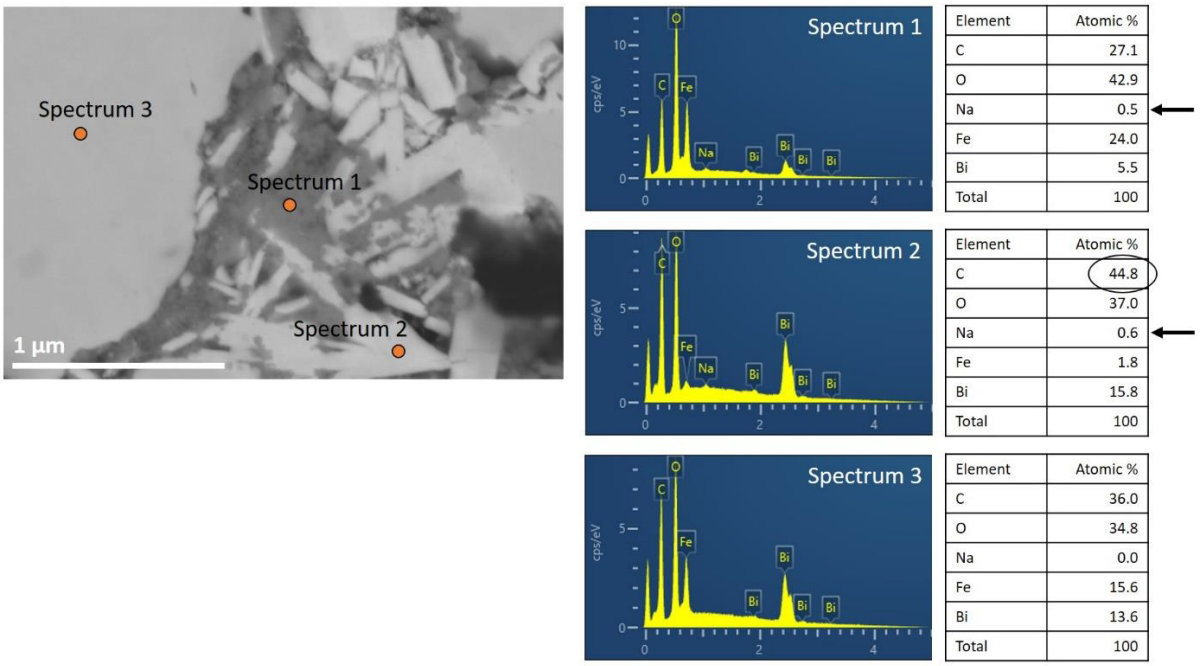

Element	Atomic %
C	27.1
O	42.9
Na	0.5
Fe	24.0
Bi	5.5
Total	100

Element	Atomic %
C	44.8
O	37.0
Na	0.6
Fe	1.8
Bi	15.8
Total	100

Element	Atomic %
C	36.0
O	34.8
Na	0.0
Fe	15.6
Bi	13.6
Total	100

Figure S2: SEM image of BFO ceramics cold-sintered with 4.8 wt% NaOH–EtOH solution (see Figure 1a and main text). EDS spectrums indicate secondary phases at the grain boundaries: Spectrum 1 = Fe-rich phase, Spectrum 2 = Bi-rich phase, Spectrum 3 = BFO. Arrows point to small quantities of Na in the secondary phases. Circled in Spectrum 2 is higher quantity of carbon in the Bi-rich phase, pointing to Bi-carbonate (see XRD in Fig. 2a and EDS maps in Fig. 3, main text). The Fe-rich phase in Spectrum 1 is likely Fe_2O_3 (carbon is included here for comparison to the carbonate phase in Spectrum 2, and is present due to carbon sputtering of the SEM sample to avoid charging; the same for Spectrum 3). The smaller amount of Bi compared to Fe in Spectrum 3 that corresponds to the BFO is assigned to the analysis being performed at 5 kV, which was chosen in order to properly detect light elements.

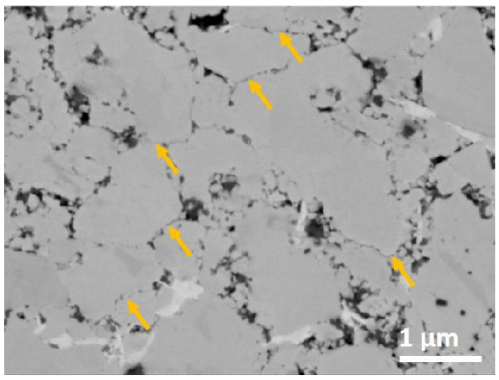

Figure S3: SEM image of BFO ceramics cold-sintered with NaOH–KOH–EtOH solution (see Figure 1a and main text); orange arrows point out curved (etched) grain boundary contacts, indicating successful pressure-dissolution process and compaction during sintering. At grain boundaries, intermediate nm-

sized dark spots are seen, representing either pores or secondary precipitates. The bright-grey areas are Bi-rich secondary phases.

Table S1: Summary of microstructural parameters and functional properties of BFO samples, cold sintered with different transient liquids.

Cold-sintered sample with	**Relative density** (%)	**Secondary phases**	**Specific electrical conductivity** (A/cm^2)	**Relative permittivity** at 1 kHz	**Dielectric losses** at 1 kHz	**Remanent polarization** at 10 Hz ($\mu C/cm^2$)	**Coercive electric field** at 10 Hz (kV/cm)
OH^- + EtOH	80 – 90 %	$(BiO_2)CO_3$ + Fe-oxide	~ $2 * 10^{-7}$	~ 130	~ 0.15	~ 40	~ 150
OH^- + urea + H_2O	90 – 92 %	$(BiO_2)CO_3$ + Fe-oxide	~ $3 * 10^{-9}$	~ 80	~ 0.10	/	/
OH^- + H_2O	93 – 96 %	No sec. phase	~ $5 * 10^{-11}$	~ 100	~ 0.05	~ 20	~ 150

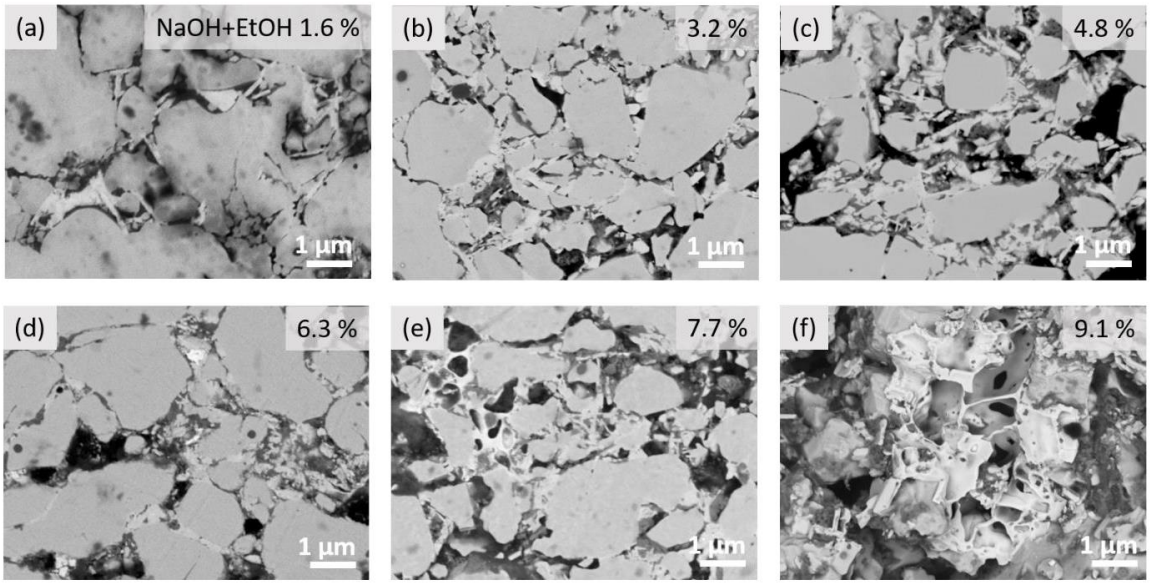

Figure S4: SEM images of polished cold-sintered BFO samples with increasing amount of the NaOH-EtOH solution mixed with 0.1 ml of water, resulting in increasing solution concentration (due to ethanol evaporation) and increasing final amounts of added solid NaOH per 0.6 g of BFO powder: (a) 1.6 wt%, (b) 3.2 wt%, (c) 4.8 wt%, (d) 6.3 wt%, (e) 7.7 wt%, (f) 9.1 wt%. Brighter grey phase is the Bi-rich phase (carbonate or Bi_2O_3) in the inner-grain space, alongside dark grey Fe-rich precipitates. Black regions are pores; their amount significantly increases when >6 wt% NaOH is added. In (a) surface grown secondary phases appear as darker shadows. At higher NaOH–EtOH amounts (e and f) the Bi-rich phase appears partially as hardened liquid phase, flooding the grains. The matrix grains within the Bi-rich 'boxwork' are partially missing (f), likely indicating a stronger dissolution process during sintering, leading to larger porosity. In (f) some residual NaOH phase is seen in dark grey in pores.

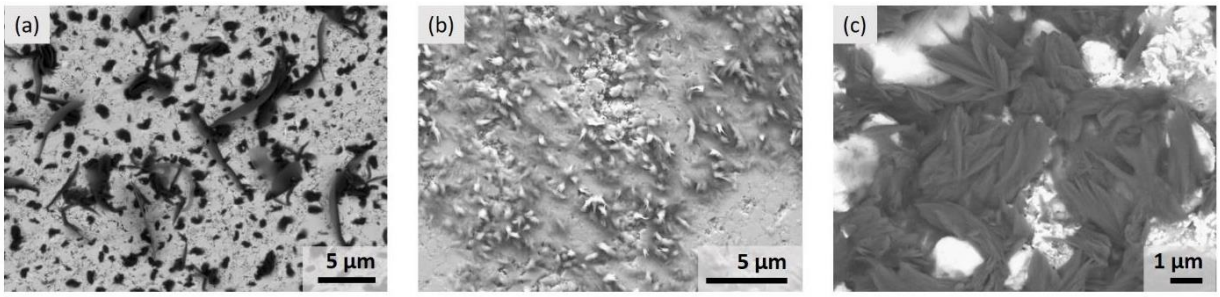

Element	Atomic %
C	64.7
O	27.6
K	7.7
Total	100

Element	Atomic %
C	59.0
O	33.1
Na	7.9
Total	100

Element	Atomic %
C	13.0
O	68.1
Na	18.9
Total	100

Figure S5: Secondary phases grown on the surface of polished samples that were not vacuum dried after sintering and polishing: (a) backscattered-electron SEM image with dark grey crystals of K-carbonate; (b) secondary-electron SEM image of crystals of Na-carbonate; (c) backscattered image of crystals of a Na-rich phase (Na-oxide or NaOH). Below the images are tables with elemental composition of secondary phases obtained by EDS; note that excess C comes from carbon sputtering of the samples' surface.

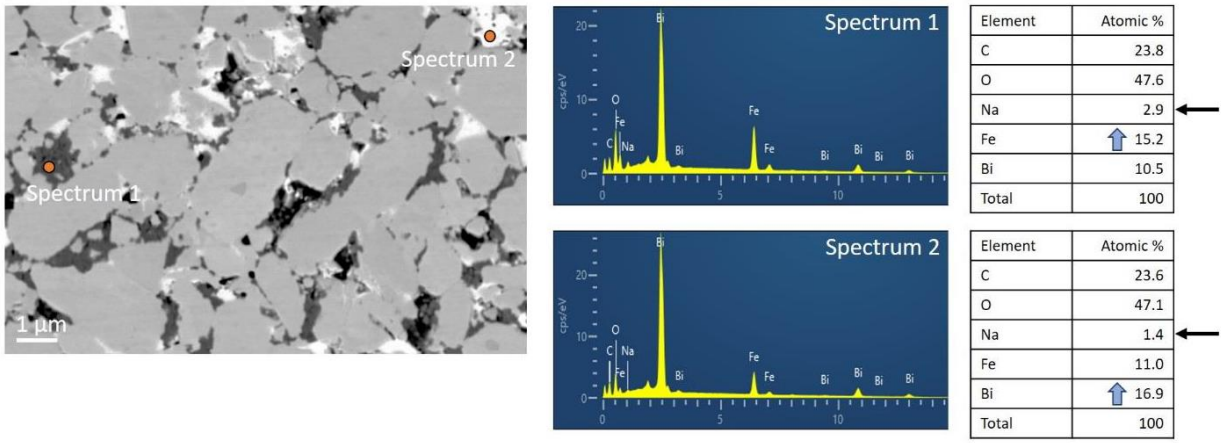

Element	Atomic %
C	23.8
O	47.6
Na	2.9
Fe	⇧ 15.2
Bi	10.5
Total	100

Element	Atomic %
C	23.6
O	47.1
Na	1.4
Fe	11.0
Bi	⇧ 16.9
Total	100

Figure S6: SEM image of BFO ceramics cold-sintered with 5.7 wt% NaOH–water solution. The powder-liquid mixture was dried in vacuum drier prior to cold sintering at 300 °C for 3h. EDS spectrums taken at 20 kV indicate secondary phases at the grain boundaries: Spectrum 1 = Fe-rich phase (dark grey), Spectrum 2 = Bi-rich phase (white). Higher levels of Fe and Bi in the respective Fe-rich and Bi-rich phases are indicated by blue arrows. Due to the high voltage used and thus the high interaction volume of each EDS measurement, the Spectra show significant amounts of all elements. Black arrows point to Na content present in both secondary phases. Carbon is included to confirm lower levels than they would appear in the case of a carbonate phase.

PART 3: Structure analysis

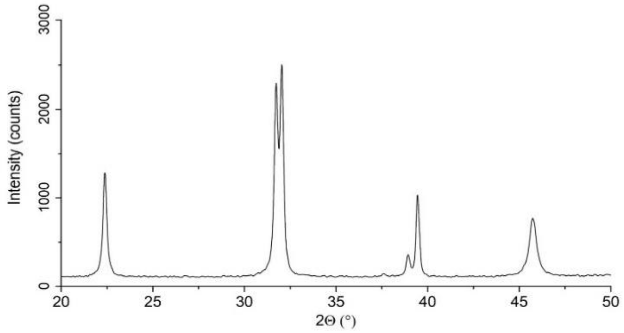

Figure S7: XRD of BFO ceramics cold-sintered with aqueous solution of NaOH–KOH (microstructure of the sample is shown in Fig.4 of the main paper). Minor reflection at ~37.5° marks the anti-phase tilt superstructure reflection from the rhombohedral *R*3*c* perovskite symmetry. Relatively broad peaks at their root indicate the presence of nanosized grains or crystallites, which are likely a result of grain fragmentation and lattice gliding and twisting due to high pressure applied during cold sintering.

Chapter 3
Structure and Electrical Properties of Cold - Sintered Strontium - Doped Potassium Sodium Niobate

In this study, we demonstrated that an aqueous solution of NaOH-KOH mixture in a 1:1 molar ratio can be effectively used as a transient liquid in cold sintering of KNN. The such-obtained KNN ceramics exhibits a relative density greater than 95%. Sr-doping of KNN is used for better control of particle growth during calcination giving more uniform particle size distribution.

First, we showed that the magnitude of uniaxial pressure impacts pore formation, which in turn influences the ferroelectric and dielectric properties. Specifically, KNN samples cold-sintered under 200 MPa exhibited large segregated pores, leading to increased dielectric losses. In contrast, KNN sintered under 675 MPa had significantly lower dielectric losses (< 0.05 in the frequency range of 100 Hz to 1 MHz) and a higher dielectric constant (up to 1000) compared to conventionally sintered KNN. However, atomic resolution images revealed that high uniaxial pressure has a significant effect on perovskite structure, causing distorted lattice of the grains and lattice dislocations.

Second, measurements of ferroelectric properties on as-sintered samples revealed that samples exhibited high dielectric losses, suggesting that oxygen vacancies may form during the cold sintering process of KNN. The properties improved under annealing the sample at 500 °C in oxygen. The polarization vs. electric field measurements of cold-sintered KNN, compared to conventionally sintered KNN, showed a higher dielectric breakdown strength, reaching 170 kV/cm, but with a lower remanent polarization of around 10 $\mu C/cm^2$. It was demonstrated that the remanent polarization of KNN is improved when using an initial powder with a larger particle size, increasing polarization due to the stronger intrinsic (lattice) and extrinsic (domain wall) contribution to the response.

Third, due to the high dielectric breakdown strength and low remanent polarization of bulk cold-sintered KNN, this material can be used as energy storage capacitor. We calculated the energy storage efficiency and recoverable energy density, yielding values of 47 % and 1.13 J/cm^3, respectively, which is a promising value for further optimization.

This chapter addresses thesis objective 2.

Published in: Salmanov, S., Koblar, M., Kmet, B., Malič, B., Rojac, T., Kuščer, D., & Otoničar, M.. Structure and electrical properties of cold-sintered strontium-doped potassium sodium niobate. Journal of the European Ceramic Society, 43(16) (2023) 7516-7523.
https://doi.org/10.1016/j.jeurceramsoc.2023.07.069

My contribution: I cold-sintered all samples under different conditions, prepared samples for SEM and other microstructure analyses, measured densities, and performed the measurements of dielectric and ferroelectric properties. I also performed the necessary calculations, interpreted the results, and developed the manuscript together with co-authors.

Journal of the European Ceramic Society 43 (2023) 7516–7523

Contents lists available at ScienceDirect

Journal of the European Ceramic Society

journal homepage: www.elsevier.com/locate/jeurceramsoc

Structure and electrical properties of cold-sintered strontium-doped potassium sodium niobate

Samir Salmanov [a,b], Maja Koblar [a,b], Brigita Kmet [a,b], Barbara Malič [a,b], Tadej Rojac [a,b], Danjela Kuščer [a,b], Mojca Otoničar [a,b,*]

[a] Electronic Ceramics Department, Jožef Stefan Institute, Ljubljana, Slovenia
[b] Jožef Stefan International Postgraduate School, Ljubljana, Slovenia

ARTICLE INFO

Keywords:
Cold sintering
Potassium sodium niobate
Lead-free perovskite
Energy storage

ABSTRACT

Cold sintering is an attractive method for sintering ferroelectric ceramics at temperatures at or below 300 °C. While we can practically obtain bulk samples by introducing a transient liquid and applied pressure, the mechanisms of sintering and final functional properties of cold-sintered ceramics are far from being understood. Here, we investigate the influence of grain size and sintering parameters on the microstructure and ferroelectric properties of 0.5 % Sr-doped $K_{0.5}Na_{0.5}NbO_3$ ceramics. By comparing with the conventionally-sintered samples, we find that cold-sintered ceramics have higher dielectric permittivity and lower dielectric losses, which we attribute to smaller grains and higher relative density. Using atomic-scale analysis, we point out the presence of numerous lattice dislocations that likely act as pinning sites and thus inhibit any significant polarization-switching behaviour. Due to the slim P–E loop and high dielectric breakdown fields of the cold-sintered ceramics we consider its potential for energy storage applications.

1. Introduction

One of the main requirements for piezoceramic materials in the EU has been the replacement of lead-containing ceramics with lead-free alternatives [1]. Potassium sodium niobate – $K_{0.5}Na_{0.5}NbO_3$ (KNN) is one of the perovskite materials with piezoelectric properties that meet this requirement. However, the synthesis and sintering of KNN are associated with several problems, such as exaggerated grain growth, volatilization of alkali species, and a narrow temperature range for sintering [2]. Since surface diffusion dominates the initial stage of sintering (above ~ 600 °C) and coarsening is preferred over densification, this contributes to an inhomogeneous microstructure with large grains and intragranular porosity, resulting in low-density ceramics. Volatilization of alkali species occurs at the sintering temperature (~1100 °C) and can lead to non-stoichiometry and formation of secondary phases. The narrow temperature range of solid-state sintering, which is close to the melting point (~ 1150 °C), requires control of temperature and limits the success of the sintering process [2]. These problems deteriorate the functional properties of the KNN material. To overcome the above issues and obtain dense single-phase ceramics with good functional properties, various approaches have been attempted, such as changing the chemical composition, varying the processing conditions, adding low-melting point additives and utilizing different sintering techniques. In particular, excessive grain growth can be avoided by changing the sintering atmosphere: a reducing atmosphere was shown to cause oxygen vacancies that suppressed grain growth [3,4]. High density can also be achieved by the use of additives, for example CuO [5], which promotes liquid-phase sintering. Spark plasma sintering (SPS) allows to obtain dense KNN with small grain size. This is possible thanks to the fast heating rate that favours the lattice diffusion, the uniaxial pressure that contributes to the grain rearrangement, and the short duration of the sintering process that minimizes the volatilization of alkali species [6–10]. Doping with an A-site donor of KNN is another method to overcome the above problems [11]. In particular, Sr as the dopant was reported to reduce the grain size in KNN [12,13].

Compared to conventional sintering, the cold sintering process (CSP) is a technique that allows ceramics to be sintered at drastically lower temperatures, even below 300 °C [14–18]. Under such conditions, excessive grain growth and alkali volatilization are not expected, which makes the CSP highly suitable for producing KNN ceramics. The CSP enables sintering of ceramics under uniaxial pressure at up to 300 °C, with the participation of additional compounds (e.g., water, organic

* Correspondence to: Electronic Ceramics Department, Jožef Stefan Institute, Jamova cesta 39, 1000 Ljubljana, Slovenia.
E-mail address: mojca.otonicar@ijs.si (M. Otoničar).

https://doi.org/10.1016/j.jeurceramsoc.2023.07.069
Received 21 March 2023; Received in revised form 17 July 2023; Accepted 27 July 2023
Available online 28 July 2023

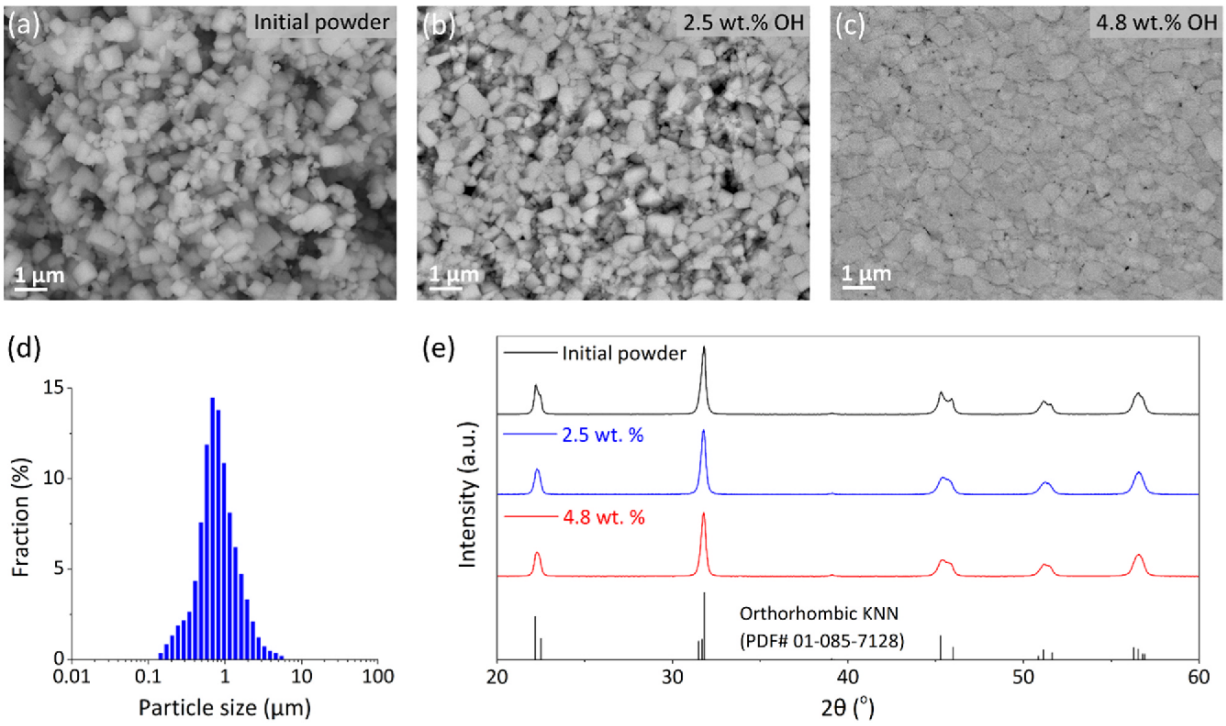

Fig. 1. SEM images of (a) KNNSr powder used for CSP. KNNSr ceramics cold-sintered at 300 °C under 675 MPa for 6 h containing (b) 2.5 wt% OH and (c) 4.8 wt% OH. (d) Particle size distribution of KNNSr powder with d_{50} 0.7 μm. (e) XRD patterns corresponding to KNNSr powder and ceramics with marked peaks of the orthorhombic symmetry in the bottom.

with CSP due to the pressure-dissolution process.

Based on the analysis of the structure and microstructure we concluded that the appropriate concentration of the added hydroxide mixture for cold sintering of KNNSr is 4.8 wt% OH. Thus, we fixed the 4.8 wt% OH amount for the following optimization of the applied pressure during the CSP. We also set the duration of the dwell time to 2 h, as we did not find any relevant difference between 6 and 2 h of cold sintered KNNSr (see Supplementary part 2 for the comparison of microstructures).

Fig. 2 shows a comparison of the microstructure, dielectric permittivity (ε') and dielectric losses (tan δ), and polarization vs. electric field (P–E) loops of KNNSr samples that were cold sintered with 4.8 wt% OH at 300 °C for 2 h at different uniaxially applied pressures, namely, 200 MPa, 340 MPa and 675 MPa. SEM images (Fig. 2(a–c)) show a strong dependence of the microstructure and relative density on the applied pressure. The sample cold sintered at 200 MPa contains up to 10 μm large non-sintered or poorly-sintered areas, which appear as evenly spread hollows (see red arrows in Fig. 2(a,b) and the inset in Fig. 2(a)). The sample cold sintered at 340 MPa (Fig. 2(b)) also exhibits similar features, uniformly distributed throughout the bulk, but smaller than at 200 MPa, up to 5 μm in diameter. Here, the matrix area between the poorly-sintered regions appears denser than in the 200 MPa sample, but exhibits some microcracks (see yellow arrows). The sample sintered at 675 MPa, however, shows a dense homogenous microstructure (Fig. 1 (c)). It is important to mention that the sample was cracked and partially delaminated when pressed out of the pressing die. Based on the microstructure analysis of the samples sintered at different pressures we can conclude, that the applied pressure has a strong influence on the microstructure, density and pore formation. Lower pressures lead to the formation of large poorly-sintered areas, which could be an effect of trapped liquid under hydrostatic pressure [31] that fails to migrate laterally, floods the grains and prevents the pressure-dissolution process at the grain contacts. Higher pressure, on the other hand, promotes better densification and results in dense ceramics.

The electrical properties of samples sintered at different pressures are shown in Fig. 2(d-f). Prior to the measurements, the samples were post-annealed in oxygen as described in the experimental part. We note that the colour of the ceramics changed from initial white-coloured powder to blue-grey only for samples that were successfully cold-sintered and resulted in a bulk pellet. Annealing then changed the colour of the pellets from blue-grey to white, from which we speculate that oxygen vacancies ($V_O^{\bullet\bullet}$) formed during cold sintering, which could further be compensated by a reduction of Nb^{5+} to Nb^{4+}. Without the annealing process the samples were too conductive for ferroelectric measurements and appeared lossy. While it is not clear how the oxygen vacancies could be formed at such low temperatures during the CSP (i.e., 300 °C), we speculate that two factors could play a role: ceramic particles during sintering are covered by liquid and do not have direct access to air when closed in a die, and potentially a chemical reaction between the perovskite and the hydroxides and/or water takes place [32], however, we could not yet confirm these argumentations.

Fig. 2d and e show that the dielectric permittivity increases and dielectric losses decrease with the increasing sintering pressure. In the lower frequency range, both permittivity and tanδ increase, with the increase more significant in the low-pressure-sintered sample; see blue curve). While it is difficult to ascertain the exact origin of this low-frequency relaxation, the large losses at lower frequencies (i.e., tanδ ~0.15 at 100 Hz in the 200 MPa sample) indicate contributions from the electrical conductivity, which diminish with the increasing sintering pressure. It is reasonable to assume that this trend is related to the microstructure evolution, where the sample with the larger poorly-sintered areas has the lowest permittivity and the highest dielectric losses, likely reflecting weaker contacts between the grains and higher porosity. While we could envisage that such a response could also result from remains of hydroxide species or their decomposition/reaction products, this seems unlikely as the samples were post-annealed. Comparison of dielectric properties of cold-sintered samples to conventionally sintered KNNSr (see Supplementary part 3 for results on

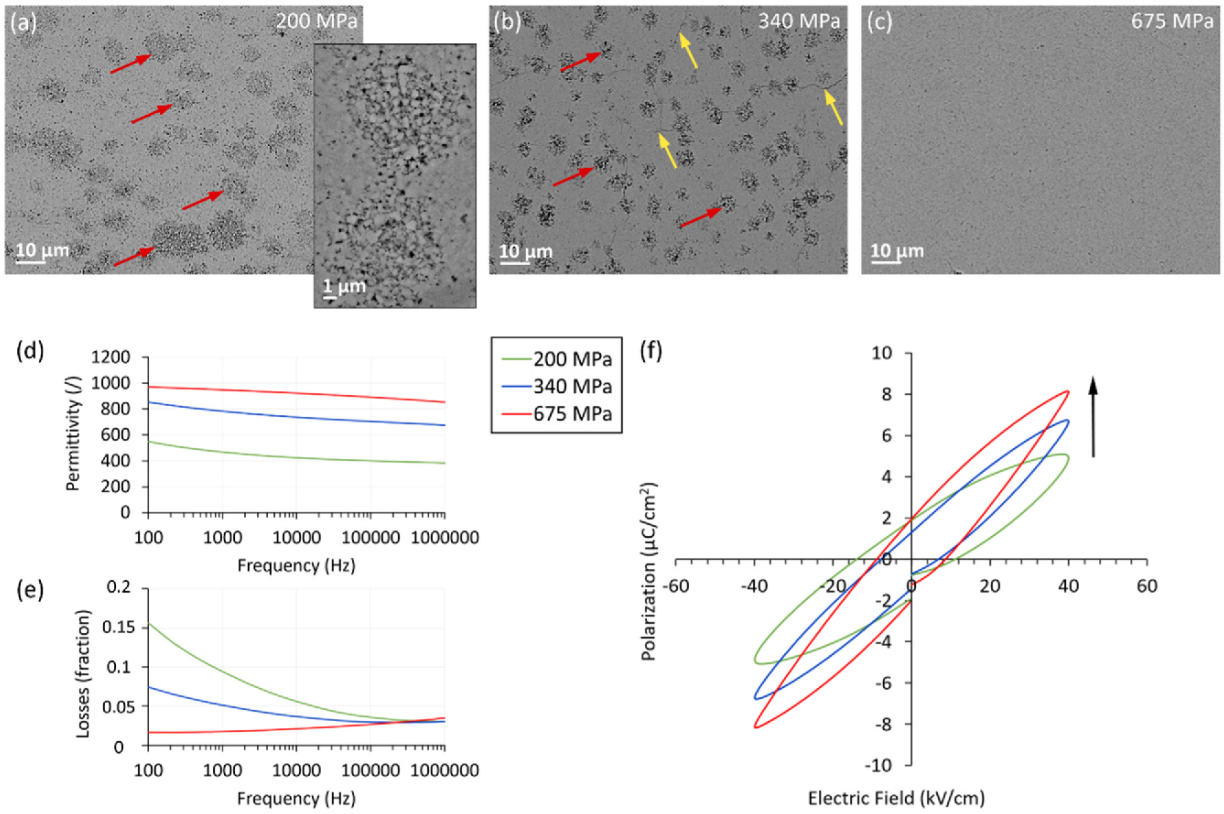

Fig. 2. Effect of pressure on microstructure, dielectric and ferroelectric properties of cold-sintered KNNSr. Microstructure of KNNSr cold-sintered at 300 °C for 2 h with 4.8 wt% OH under (a) 200 MPa, (b) 340 MPa, (c) 675 MPa. Red arrows indicate "pockets" of poorly-sintered regions (enlarged in the inset of (a)), yellow arrows indicate microcracks. (d) The dielectric permittivity and (e) dielectric losses as a function of frequency, and (f) the polarization vs. electric field loops of the same KNNSr samples; arrow in (f) marks increasing polarization as the applied pressure during sintering increased.

microstructure and dielectric properties of a sample sintered at 1120 °C for 2 h in oxygen) reveals that the samples cold-sintered at 340 and 675 MPa have a higher dielectric permittivity (2 times higher in the 675 MPa sample; $\varepsilon'_{676\,MPa}$~1000 @100 Hz) and a lower tan δ value than the conventionally sintered sample (the 676 MPa sample has up to 4 times lower losses; $\tan\delta_{676\,MPa}$~0.02 @100 Hz). The main reason for the differences in dielectric properties could be the significantly different grain size of the ceramics. The estimated grain size of cold-sintered KNNSr is around 0.7 µm, while it is 10–30 µm for the conventionally sintered KNNSr. The larger grains in the conventionally sintered KNNSr are accompanied by larger pores between the cube-shaped grains, with relative density, calculated from its theoretical density (4.51 g/cm^3 [33]) and measured geometrical density (4.15) up to 92 %, while we estimated the relative density of the cold-sintered sample at 675 MPa to above 96 %. It was previously shown that the grain size and the corresponding number of grain boundaries affect the accumulated charges and, thus, strongly influence the dielectric properties [34,35]. It was shown in the case of $BaTiO_3$ [36] that the maximum dielectric constant is reached when the average grain size is about 1 µm (our cold-sintered KNNSr has an average grain size of ~0.7 µm), which the authors assigned to the highest mobility of the domain walls.

Fig. 2f shows the polarization vs. electric field (P–E) loops of the three KNNSr samples cold sintered at different pressures, obtained at 40 kV/cm. We note that the field amplitude of 40 kV/cm, which should be sufficient for polarization saturation in conventionally sintered KNNSr samples, fails to saturate the loops of cold-sintered samples. The comparison of the unsaturated P–E loops shows that the higher the applied pressure during cold sintering, the higher the value of maximum polarization (see arrow). Also, samples cold-sintered at 675 and 340 MPa have a sharper tip of the P–E loop than the 200 MPa sintered sample, which suggests a nonlinear hysteresis in the response consistent with RL-like behaviour [37] (note that in all cases a sinusoidal voltage was applied, so the sharp tips are not related to nonlinear voltage signal, as it is usually the case when using triangular voltage waveform). The more rounded P–E loop tip and larger hysteresis area in the 200 MPa sample (blue line) is likely related to the leakage current [38] (see Supplementary part 4 for evolution of the P–E loops with increasing field for the 200 MPa vs. the 675 MPa sample). The loop of the 340 MPa sample appears slightly pinched, a feature that was generally observed on the first cold-sintered KNN samples recently [22], and was assigned to a strongly limited irreversible domain-wall motion. Combining all the results measured on samples sintered at different pressures we can again conclude that the poorer ferroelectric properties and higher dielectric losses in samples cold-sintered at lower pressures are due to microstructural inhomogeneities related to the presence of the poorly-sintered regions causing porosity (see Fig. 2(a,b)).

Fig. 3 compares the dielectric constant as a function of temperature, the P–E loops, and the strain-electric field (S–E) loops in the respective field range of saturation of the cold-sintered (at 675 MPa) and conventionally sintered samples (the latter were sintered at 1120 °C in O_2 for 2 h; see Supplementary part 3 for microstructure). The dielectric permittivity results show two peaks that correspond to the phase transitions from orthorhombic to tetragonal symmetry at about 170–180 °C and from tetragonal to cubic symmetry at ~390 °C (Fig. 3(a,b)), in accordance with the literature [28]. While the phase transition peaks are present in both samples, they are strongly suppressed in the case of the cold-sintered sample, which is likely due to the small grain size and the lower level of crystallinity (indicated from the poor peak splitting and

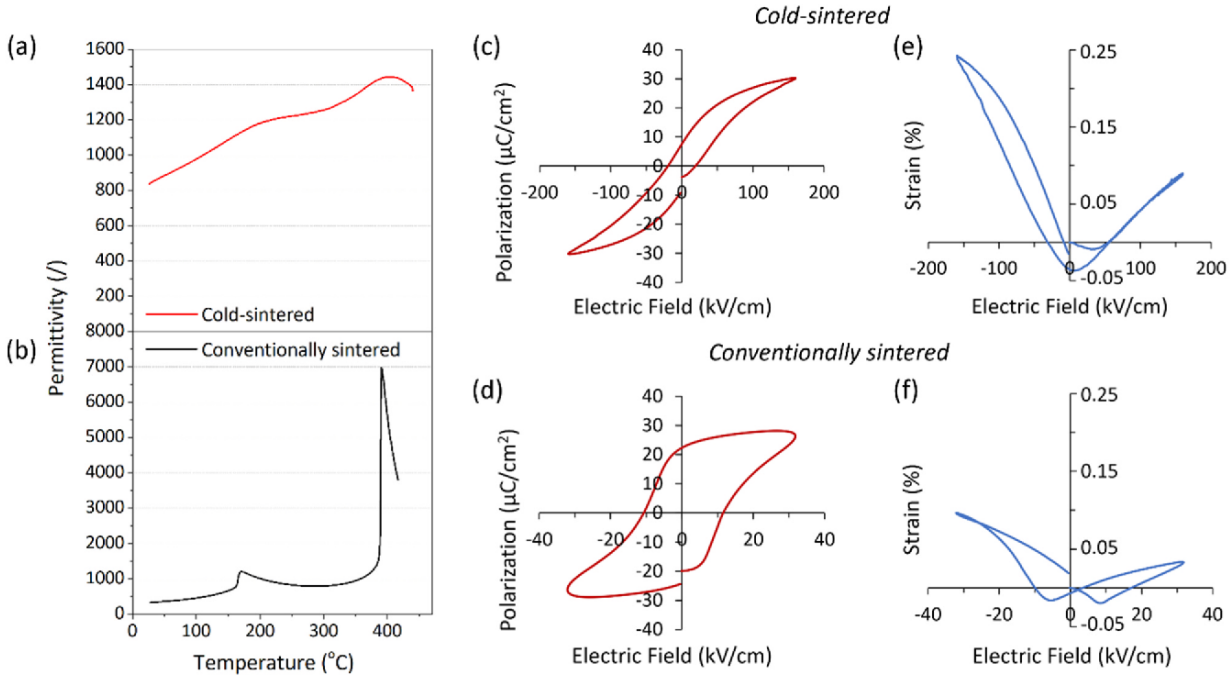

Fig. 3. Comparison of dielectric and electrical/electromechanical properties of the KNNSr cold-sintered at 675 MPa and 300 °C for 2 h, containing 4.8 wt% OH (top), and conventionally sintered KNNSr (at 1120 °C for 2 h in O_2; bottom). (a, b) Dielectric permittivity as a function of temperature, measured at 1 MHz showing two peaks associated to phase transitions. (c, d) Polarization vs. electric field (P–E) loops, and (e, f) strain vs. electric field (S–E) loops (100 Hz) of the cold-sintered and conventionally sintered KNNSr samples, respectively.

peak sharpness in XRD in the cold-sintered ceramics, see Fig. 1(e)). Note that the polarization and strain loops of cold-sintered KNNSr (Fig. 3(c, e)) were measured up to 160 kV/cm, while conventionally sintered KNNSr was measured only up to 35 kV/cm (Fig. 3(d,f)). The conventionally sintered KNNSr already approaches saturation at 35 kV/cm, followed by a dielectric breakdown, while the cold-sintered sample shows a delayed polarization saturation and requires much larger fields for the ferroelectric loop to develop. The measurements indicate that the dielectric breakdown field of cold-sintered KNNSr is significantly larger compared to conventionally sintered KNNSr, which could be due to smaller grain size and lower porosity [39]. Despite the much larger dielectric breakdown field of the cold-sintered sample, both samples achieved maximum polarization of about 30 $\mu C/cm^2$, while the remanent polarization (P_r) of cold-sintered sample was only about 8 $\mu C/cm^2$, which is more than three times lower than that of the conventionally sintered sample (compare in Fig. 3(c,d)). The loop of conventionally sintered sample, however, appears lossy, with its rounded tip, indicating an influence of electrical conductivity, which could contribute to the apparent increase of polarization. The strain loops of the cold-sintered and conventionally sintered samples (Fig. 3(e,f)) show that the conventional sample exhibits a classical butterfly-shaped loop that represents ferroelectric/ferroelastic switching, while in the case of cold-sintered sample the strain loop is less developed in terms of a butterfly shape and related domain switching. The achieved maximum strain of the cold-sintered sample is about 0.28 %, while the peak-to-peak strain of the conventionally sintered sample is 0.12 %. Both samples show a significant asymmetry in the strain loop, which was previously assigned to local regions having frozen-in domain structures, clamped by internal bias [40], but could also arise from the stress imposed by the upper contact screw during the measurement. The differences in the strain behaviour of cold-sintered and conventionally sintered samples, as well as in the polarization response with the cold-sintered sample showing a much slimmer, less hysteretic P–E loop, both point to a limited ferroelectric/ferroelastic switching in cold-sintered samples. This could be related to the grain size of ceramics with significantly smaller grains in the case of cold sintering, which results in stronger pinning of the domain walls (similarly as found in $BaTiO_3$ [41]).

As mentioned earlier, the CSP of KNNSr allows to obtain dense ceramic samples with the grain size similar to particle size of the initial KNNSr powder, which was shown to be ~0.7 μm in the studied samples. Taking into account the relatively large fraction of nanosized grains (Fig. 1d), the fact that the initial powders were produced at temperatures up to 800 °C and that XRD results show less pronounced peak splitting (Fig. 1e), as well as strongly suppressed dielectric permittivity across the phase transition temperatures (Fig. 3b) and the slim P–E and S–E loops, it is reasonable to assume that the lattice distortions are less pronounced and the ferroelectric/ferroelastic domains are likely undeveloped. While it is known that up to 70 % of the total macroscopic piezoelectric response can arise from domain wall displacements, with the domain-wall effect strongly grain-size dependent, the low induced P_r and the limited switching behaviour of the cold-sintered sample could be related to the small grains and low level of lattice distortion, with limited number of domain walls that are possibly clamped, making the cold-sintered KNNSr an underdeveloped piezoelectric.

In order to understand the influence of microstructure on the properties of cold-sintered KNNSr, we performed scanning transmission electron microscopy (STEM). Results are presented in Fig. 4. The observations lead to an additional aspect related to the intrinsic nature of the cold-sintered KNNSr samples. Firstly, all grains appeared to be heavily distorted with bent lattice planes, which is nicely observed from the dark contours and changing contrast in the bright-field image of Fig. 4a, where darker lines fully penetrate the grain and create a cunning or kneaded structure. Looking at the crystal lattice in more detail, a series of edge or screw dislocations were detected throughout the grains, likely compensating for the bending of the lattice under the applied pressure during cold sintering – see Fig. 4b-c. Fast Fourier transform (FFT) of Fig. 4b (inset; see splitting of reflections) represents the angular misorientation of the lattice of one part of the grain compared to the other part across the dislocation path, resulting in the so-called low-

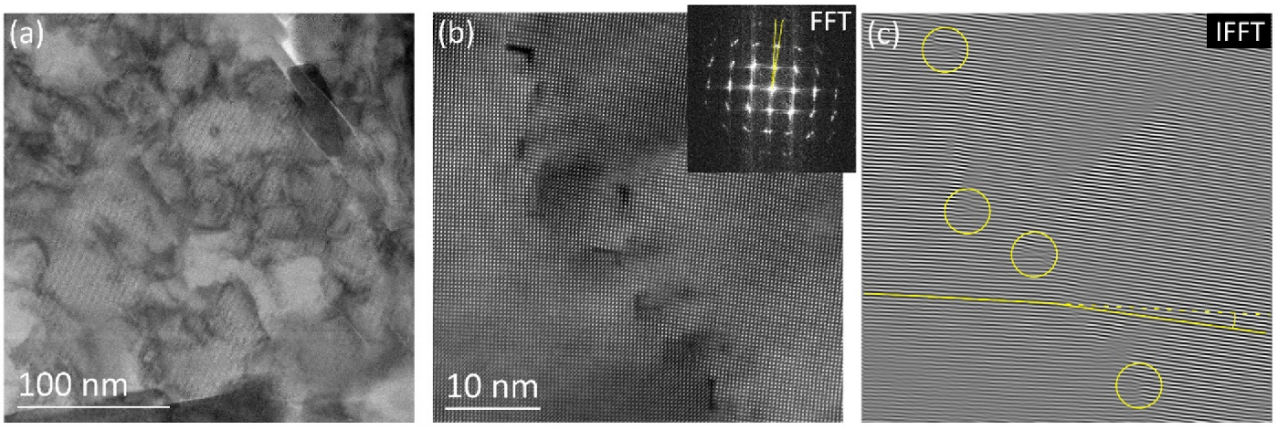

Fig. 4. STEM images of defect-structured lattice of the cold-sintered KNNSr at 675 MPa. (a) Bright-field (BF) image of a strongly distorted single grain, with contrast-dominated contours from lattice bending and dislocations. (b) High-angle annular dark-field (HAADF) image of a grain in <100> zone, showing a series of dislocations; inset shows the corresponding Fast Fourier Transform-FFT, with splitting of reflections corresponding to the obliquity angle between the two parts of the grain. (c) Inverse FFT of (b) with some dislocations circled; the misorientation of lattice planes across the dislocation path is indicated by the dashed line.

angle grain boundaries. The inverse fast Fourier transform (IFFT) in Fig. 4c, obtained from Fig. 4b, shows more clearly the points of dislocations (marked by yellow circles) and the bent lattice planes cross the dislocation path (dashed line). This result indicates that there is a substantial plastic deformation induced by the compressive stress and that the KNNSr ceramics is, unlike we would expect for oxide ceramics, highly deformable [42]. It was challenging to pinpoint any domain walls in such a strongly deformed crystal lattice, and more efforts are needed to identify them.

The described microstructure with high density of defects seems to strongly contribute to the suppressed polarization and limited domain-wall dynamics, observed from the dielectric and ferroelectric response. It is anticipated that great internal stresses are present in the material from the ferroelastic DW creation when cooled below the tetragonal-to-orthorhombic transition, which were not relieved, likely due to DW-defect interactions. Furthermore, the dislocations are likely charged which could increase conductivity by creating free electron paths. Both, accumulated internal stresses and charged dislocations can severely influence the materials' response; further studies are needed to quantify them.

Since the cold-sintered KNNSr exhibits a slimmer hysteresis loop with low remanent polarization, low dielectric/hysteresis losses, and delayed polarization saturation with a high dielectric breakdown strength, this material could be considered as an attractive capacitor for energy-storage applications. We therefore calculated the energy storage efficiency and recoverable energy density of the cold-sintered KNNSr from the P–E loop obtained at 160 kV/cm (Fig. 5):

$$\eta = U_{rec}/(U_{rec} + U_{loss}) = 47\ \%$$

$$U_{rec} = 1{\cdot}13\ J\ cm^{-3}$$

where η is the energy storage efficiency, U_{rec} is recoverable energy density and U_{loss} energy loss.

Similar values of recoverable energy and energy storage efficiency were calculated for pure KNN, however, they were obtained only when higher electric fields could be applied. For example, pure KNN prepared by the solid state method [43] was cycled at 200 kV/cm and showed $U_{rec} = 0.71\ J{\cdot}cm^{-3}$ and $\eta = 18.8\ \%$. Another research group calculated $U_{rec} \approx 0.6–0.7\ J\ cm^{-3}$ and $\eta \approx 70\ \%$ for pure KNN [44] when 170 kV/cm was applied. From this comparison it appears that cold-sintered KNNSr has a higher recoverable energy density even at lower electric fields (160 kV/cm), while the energy storage efficiency is lower due to the larger energy losses from the broader hysteresis loop. These could be tackled by cold sintering powders with even smaller grain sizes, which might improve the dielectric breakdown strength, if it does not act detrimental on the maximum polarization that could be achieved. The energy storage density could also be tweaked by thinning the cold-sintered sample and applying larger fields. With still room to improve, these results suggest that the CSP has a good potential for fabricating high-quality dense KNN-based materials as attractive capacitors for energy storage applications.

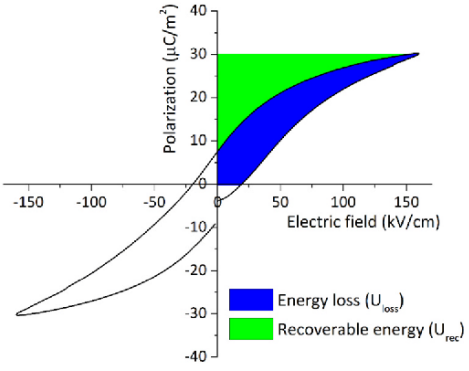

Fig. 5. Recoverable energy density (green) and energy loss (blue) obtained from the P–E loop of cold-sintered KNNSr.

4. Conclusions

The main advantage of the cold sintering process for processing ferroelectric perovskites is the possibility to obtain dense ceramics at drastically lower temperatures than by conventional sintering, but under high pressure and with addition of a transient liquid phase. In this report we establish a relationship between the cold sintering parameters and the properties of Sr-doped KNN ceramics sintered with a eutectic mixture of NaOH and KOH. In particular, we report on the effects of hydroxide concentration and sintering pressure on the microstructure and electrical properties. We demonstrate that there is a crucial amount of hydroxides for our KNNSr powder – about 4.8 wt% – below which the CSP is not effective. The higher the applied sintering pressure, the higher the relative density is, leading to higher dielectric permittivity, lower dielectric losses, and higher dielectric breakdown fields. However, applying high pressures comes with a cost: atomic-scale analysis shows that lattice bending and numerous lattice dislocations are formed. Together with limited diffusion due to the low temperature sintering

(300 °C), which also limits grain growth, these features strongly affect the ferroelectric response of the ceramics, inhibiting significant polarization switching behaviour. Nevertheless, we show that cold-sintered KNNSr with its slim P–E loop and high dielectric breakdown fields is an attractive capacitor for energy storage applications. Although cold sintering of KNNSr still leaves many questions to be explored, we believe that our results will contribute to the community and stimulate further studies on CSP of ferroelectric perovskites.

Funding

This research was funded by the Slovenian Research Agency (grant numbers J2-2508, P2-0105, J7-4637, and young researcher's programme).

Declaration of Competing Interest

The authors declare that they have no known competing financial interests or personal relationships that could have appeared to influence the work reported in this paper.

Acknowledgments

The authors would like to thank Silvo Drnovšek and Jena Cilenšek for their help with sample preparation.

Appendix A. Supporting information

Supplementary data associated with this article can be found in the online version at doi:10.1016/j.jeurceramsoc.2023.07.069.

References

[1] EU-Directive 2002/95/EC. Restriction of the use of certain hazardous substances in electrical and electronic equipment (RoHS)., Off. J. Eur. Union. 46(L37), 2003, pp. 19–23.
[2] B. Malič, J. Koruza, J. Hrešćak, J. Bernard, K. Wang, J. Fisher, A. Benčan, Sintering of lead-free piezoelectric sodium potassium niobate ceramics, Materials 8 (2015) 8117–8146, https://doi.org/10.3390/ma8125449.
[3] J.G. Fisher, S.-J.L. Kang, Microstructural changes in $(K_{0.5}Na_{0.5})NbO_3$ ceramics sintered in various atmosphere, J. Eur. Ceram. Soc. 29 (2009) 2581–2588, https://doi.org/10.1016/j.jeurceramsoc.2009.02.006.
[4] D. Kuscer, A. Kocjan, M. Majcen, A. Meden, K. Radan, J. Kovač, B. Malič, Evolution of phase composition and microstructure of sodium potassium niobate –based ceramic during pressure-less spark plasma sintering and post-annealing, Ceram. Int. 45 (2019) 10429–10437, https://doi.org/10.1016/j.ceramint.2019.02.102.
[5] M. Matsubara, T. Yamaguchi, W. Sakamoto, K. Kikuta, T. Yogo, S.I. Hirano, Processing and piezoelectric properties of lead-free (K,Na)(Nb,Ta)O_3 ceramics, J. Am. Ceram. Soc. 88 (2005) 1190–1196, https://doi.org/10.1111/J.1551-2916.2005.00229.X.
[6] J. Koruza, B. Malič, Initial stage sintering mechanism of $NaNbO_3$ and implications regarding the densification of alkaline niobates, J. Eur. Ceram. Soc. 34 (2014) 1971–1979, https://doi.org/10.1016/j.jeurceramsoc.2014.01.035.
[7] A.N. Klein, D. Hotza, Advanced ceramics with dense and fine-grained microstructures through fast firing, Rev. Adv. Mater. Sci. 30 (2012) 273–281.
[8] R. Raj, M. Cologna, J.S.C. Francis, Influence of externally imposed and internally generated electrical fields on grain growth, diffusional creep, sintering and related phenomena in ceramics, J. Am. Ceram. Soc. 94 (2011) 1941–1965, https://doi.org/10.1111/j.1551-2916.2011.04652.x.
[9] Z.-Y. Shen, J.-F. Li, K. Wang, S. Xu, W. Jiang, Q. Deng, Electrical and mechanical properties of fine-grained Li/Ta-modified (Na,K)NbO_3-based piezoceramics prepared by spark plasma sintering, J. Am. Ceram. Soc. 93 (2010) 1378–1383, https://doi.org/10.1111/j.1551-2916.2009.03542.x.
[10] M. Bah, F. Giovannelli, F. Schoenstein, G. Feuillard, E. Le Clezio, I. Monot-Laffez, High electromechanical performance with spark plasma sintering of undoped $K_{0.5}Na_{0.5}NbO_3$ ceramics, Ceram. Int. 40 (2014) 7473–7480, https://doi.org/10.1016/j.ceramint.2013.12.097.
[11] B. Jaffe, W.R. Cook, H. Jaffe, Piezoelectric Ceramics, Academic Press, London, 1971.
[12] M.D. Maeder, D. Damjanovic, N. Setter, Lead free piezoelectric materials, J. Electroceram. 13 (2004) 385–392, https://doi.org/10.1007/s10832-004-5130-y.
[13] B. Malic, J. Bernard, J. Holc, M. Kosec, Strontium doped $K_{0.5}Na_{0.5}NbO_3$ based piezoceramics, Ferroelectrics 314 (2005) 149–156, https://doi.org/10.1080/00150190590926373.
[14] J. Guo, H. Guo, A.L. Baker, M.T. Lanagan, E.R. Kupp, G.L. Messing, C.A. Randall, Cold Sintering: a paradigm shift for processing and integration of ceramics, Angew. Chem. Int. Ed. 55 (2016) 11457–11461, https://doi.org/10.1002/anie.201605443.
[15] H. Guo, A. Baker, J. Guo, C.A. Randall, Cold sintering process: a novel technique for low-temperature ceramic processing of ferroelectrics, J. Am. Ceram. Soc. 99 (2016) 3489–3507, https://doi.org/10.1111/jace.14554.
[16] T. Yu, J. Cheng, L. Li, B. Sun, X. Bao, H. Zhang, Current understanding and applications of the cold sintering process, Front. Chem. Sci. Eng. 13 (2019) 654–664, https://doi.org/10.1007/s11705-019-1832-1.
[17] A. Ndayishimiye, S.H. Bang, C.J. Spiers, C.A. Randall, Reassessing cold sintering in the framework of pressure solution theory, J. Eur. Ceram. Soc. 43 (2023) 1–13, https://doi.org/10.1016/J.JEURCERAMSOC.2022.09.053.
[18] A. Galotta, V.M. Sglavo, The cold sintering process: a review on processing features, densification mechanisms and perspectives, J. Eur. Ceram. Soc. 41 (2021) 1–17, https://doi.org/10.1016/J.JEURCERAMSOC.2021.09.024.
[19] S. Funahashi, J. Guo, H. Guo, K. Wang, A.L. Baker, K. Shiratsuyu, C.A. Randall, Demonstration of the cold sintering process study for the densification and grain growth of ZnO ceramics, J. Am. Ceram. Soc. 100 (2017) 546–553, https://doi.org/10.1111/jace.14617.
[20] X. Kang, R. Floyd, S. Lowum, D. Long, E. Dickey, J.-P. Maria, Cold sintering with dimethyl sulfoxide solutions for metal oxides, J. Mater. Sci. 54 (2019) 7438–7446, https://doi.org/10.1007/s10853-019-03410-1.
[21] K. Tsuji, A. Ndayishimiye, S. Lowum, R. Floyd, K. Wang, M. Wetherington, J.-P. Maria, C.A. Randall, Single step densification of high permittivity $BaTiO_3$ ceramics at 300 °C, J. Eur. Ceram. Soc. 40 (2020) 1280–1284, https://doi.org/10.1016/j.jeurceramsoc.2019.12.022.
[22] K. Tsuji, Z. Fan, S.H. Bang, S. Dursun, S. Trolier-McKinstry, C.A. Randall, Cold sintering of the ceramic potassium sodium niobate, $(K_{0.5}Na_{0.5})NbO_3$, and influences on piezoelectric properties, J. Eur. Ceram. Soc. 42 (2022) 105–111, https://doi.org/10.1016/j.jeurceramsoc.2021.10.002.
[23] G.J. Janz, R.P.T. Tomkins, Physical properties data compilations relevant to energy storage, Natl. Stand. Ref. Data Syst, 1981.
[24] B. Deng, Y. Ma, T. Chen, H. Wang, J. Lin, C. Lin, X. Wu, C. Zhao, T. Lin, M. Gao, X. Zheng, C. Fang, Elevating electrical properties of (K,Na)NbO3 ceramics via cold sintering process and post-annealing, J. Am. Ceram. Soc. 105 (2022) 461–468, https://doi.org/10.1111/jace.18103.
[25] J.-J. Lan, X.-M. Chen, L.-N. Liu, H.-L. Lian, Y.-R. He, Y.-C. Song, L.-J. Zhu, P. Liu, Low-temperature synthesis of $K_{0.5}Na_{0.5}NbO_3$ ceramics in a wide temperature window via cold-sintering assisted sintering method and enhanced electrical properties, J. Eur. Ceram. Soc. 43 (2023) 73–81, https://doi.org/10.1016/j.jeurceramsoc.2022.09.041.
[26] K. Nakagawa, M. Iwasaki, Z. Fan, J.I. Roscow, C.A. Randall, The unusual case of plastic deformation and high dislocation densities with the cold sintering of the piezoelectric ceramic $K_{0.5}Na_{0.5}NbO_3$, J. Eur. Ceram. Soc. 43 (2023) 4015–4020, https://doi.org/10.1016/J.JEURCERAMSOC.2023.02.057.
[27] J. Hrešćak, B. Malič, J. Cilenšek, A. Benčan, Solid-state synthesis of undoped and Sr-doped $K_{0.5}Na_{0.5}NbO_3$, J. Therm. Anal. Calorim. 127 (2017) 129–136, https://doi.org/10.1007/s10973-016-5615-3.
[28] B. Malic, J. Bernard, J. Holc, D. Jenko, M. Kosec, Alkaline-earth doping in (K,Na)NbO_3 based piezoceramics, J. Eur. Ceram. Soc. 25 (2005) 2707–2711, https://doi.org/10.1016/j.jeurceramsoc.2005.03.127.
[29] M.P.A. van den Ende, A.R. Niemeijer, C.J. Spiers, Influence of grain boundary structural evolution on pressure solution creep rates, J. Geophys. Res. Solid Earth 124 (2019) 10210–10230, https://doi.org/10.1029/2019JB017500.
[30] J.P. Gratier, D.K. Dysthe, F. Renard, The role of pressure solution creep in the ductility of the earth's upper crust, Adv. Geophys. 54 (2013) 47–179, https://doi.org/10.1016/B978-0-12-380940-7.00002-0.
[31] A.C. Fowler, X.-S. Yang, Dissolution/precipitation mechanisms for diagenesis in sedimentary basins, J. Geophys. Res. Solid Earth 108 (2003) 2509, https://doi.org/10.1029/2002JB002269.
[32] N.S. Bein, P. Machado, M. Coll, F. Chen, M. Makarovic, T. Rojac, A. Klein, Electrochemical reduction of undoped and cobalt-doped $BiFeO_3$ induced by water exposure: quantitative determination of reduction potentials and defect energy levels using photoelectron spectroscopy, J. Phys. Chem. Lett. 10 (2019) 7071–7076, https://doi.org/10.1021/acs.jpclett.9b02706.
[33] M. Kosec, D. Kolar, On activated sintering and electrical properties of $NaKNbO_3$, Mater. Res. Bull. 10 (1975) 335–339, https://doi.org/10.1016/0025-5408(75)90002-1.
[34] N.T. Taylor, F.H. Davies, S.G. Davies, C.J. Price, S.P. Hepplestone, The fundamental mechanism behind colossal permittivity in oxides, Adv. Mater. 31 (2019) 1904746, https://doi.org/10.1002/adma.201904746.
[35] J. Boonlakhorn, J. Manyam, P. Srepusharawoot, S. Krongsuk, P. Thongbai, Effects of charge compensation on colossal permittivity and electrical properties of grain boundary of $CaCu_3Ti_4O_{12}$ ceramics substituted by Al^{3+} and Ta^{5+}/Nb^{5+}, Molecules 26 (2021) 3294, https://doi.org/10.3390/molecules26113294.
[36] V. Buscaglia, C.A. Randall, Size and scaling effects in barium titanate. An overview, J. Eur. Ceram. Soc. 40 (2020) 3744–3758, https://doi.org/10.1016/j.jeurceramsoc.2020.01.021.
[37] A. Pramanick, A.D. Prewitt, J.S. Forrester, J.L. Jones, Domains, domain walls and defects in perovskite ferroelectric oxides: a review of present understanding and recent contributions, Https://Doi.Org/10.1080/10408436.2012.686891. 37, 2012, pp. 243–275. https://doi.org/10.1080/10408436.2012.686891.
[38] B. Kmet, D. Kuščer, S. Dutta, H. Uršič, A. Matavž, F. Levassort, V. Bobnar, B. Malič, A. Benčan, Screen printed copper and tantalum modified potassium sodium niobate thick films on platinized alumina substrates, Materials 14 (2021) 7137, https://doi.org/10.3390/MA14237137/S1.

[39] M. Vrabelj, H. Uršič, Z. Kutnjak, B. Rožič, S. Drnovšek, A. Benčan, V. Bobnar, L. Fulanović, B. Malič, Large electrocaloric effect in grain-size-engineered 0.9Pb($Mg_{1/3}Nb_{2/3}$)O_3–0.1$PbTiO_3$, J. Eur. Ceram. Soc. 36 (2016) 75–80, https://doi.org/10.1016/J.JEURCERAMSOC.2015.09.031.

[40] M. Ozgul, S. Trolier-Mckinstry, C.A. Randall, Fatigue induced effects on bipolar strain loops in PZN-PT piezoelectric single crystals, J. Electroceram. 20 (2008) 133–138, https://doi.org/10.1007/S10832-007-9120-8/FIGURES/8.

[41] M. Demartin, D. Damjanovic, Dependence of the direct piezoelectric effect in coarse and fine grain barium titanate ceramics on dynamic and static pressure, Appl. Phys. Lett. 68 (1998) 3046, https://doi.org/10.1063/1.115572.

[42] M. Höfling, M. Trapp, L. Porz, H. Uršič, E. Bruder, H.J. Kleebe, J. Rödel, J. Koruza, Large plastic deformability of bulk ferroelectric $KNbO_3$ single crystals, J. Eur. Ceram. Soc. 41 (2021) 4098–4107, https://doi.org/10.1016/J.JEURCERAMSOC.2021.02.023.

[43] M. Zhang, H. Yang, Y. Lin, Q. Yuan, H. Du, Significant increase in comprehensive energy storage performance of potassium sodium niobate-based ceramics via synergistic optimization strategy, Energy Storage Mater. 45 (2022) 861–868, https://doi.org/10.1016/j.ensm.2021.12.037.

[44] C. Li, Y. Huan, X. Wang, X. Wang, T. Wang, T. Wei, Amelioration on energy storage performance of KNN-based transparent ceramics by optimizing the polarization and breakdown strength, J. Am. Ceram. Soc. 105 (2022) 6158–6167, https://doi.org/10.1111/jace.18539.

Supplementary information for

Structure and electrical properties of cold-sintered strontium-doped potassium sodium niobate

Samir Salmanov,[a,b] Maja Koblar,[a,b] Brigita Kmet,[a,b] Barbara Malič, [a,b] Tadej Rojac,[a,b] Danjela Kuščer [a,b], Mojca Otoničar [a,b]

[a] Electronic Ceramics Department, Jožef Stefan Institute, Ljubljana, Slovenia,

[b] Jožef Stefan International Postgraduate School, Ljubljana, Slovenia

Corresponding author: Mojca Otoničar (mojca.otonicar@ijs.si)

Supplementary part 1

Synthesis: Ceramic powder with the nominal formula $(K_{0.5}Na_{0.5})_{0.99}Sr_{0.005}NbO_3$ (KNNSr), was prepared by solid-state synthesis from the following starting compounds: K_2CO_3 (anhydrous, 99.9+ %, ChemPur, Karlsruhe, Germany), Na_2CO_3 (anhydrous, 99.9+ %, ChemPur, Karlsruhe, Germany), $SrCO_3$ (99.994 %, Alfa Aesar, Karlsruhe, Germany) and Nb_2O_5 (325 mesh, 99.9 %, Sigma-Aldrich, Steinheim, Germany). All precursors were dried for 6 h at 200 °C, ball-milled in a planetary mill in acetone for 4 h to achieve finer particles and a uniform particle-size distribution, and dried for 1 h at 105 °C and 2 h at 200 °C. The milled and dried precursors were weighed in the desired stoichiometric ratio in a dry box with an Ar atmosphere, and their mixture was milled for homogenization in a planetary mill for 4 h in acetone and dried for 1 h at 105 °C and 2 h at 200 °C.

The homogenized mixture of precursors was calcined at 800 °C for 4 hours at a heating and cooling rate of 5 K/min. After planetary milling for 3 h at 175 rpm in acetone the mixture was dried for 1 h at 105 °C and 2 h at 200 °C. After drying, the mixture was calcined for an additional 4 hours at 750 °C with heating and cooling rates of 5 K/min and milled and dried again under the same conditions as described above. The as-prepared powders were used for cold sintering.

Supplementary part 2

Microstructure comparison: Investigation of the influence of cold-sintering dwell time on the grain size does not indicate any significant changes between 2h and 6h of sintering.

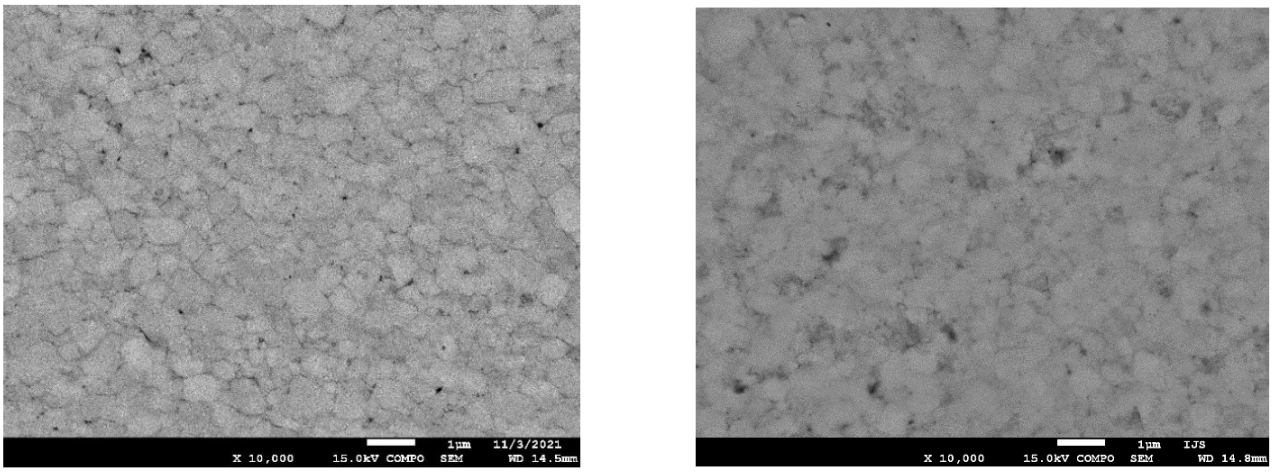

Figure S1: Microstructures of cold-sintered KNNSr samples after (a) 6h sintering and (b) 2h sintering. No significant difference is observed from porosity point of view, thus, this result was taken as proof that cold sintering under 2h is sufficient.

Supplementary part 3

Comparison to conventional sintering: Conventionally sintered KNNSr ceramic for comparison to cold sintered ceramics - see discussion in the main manuscript.

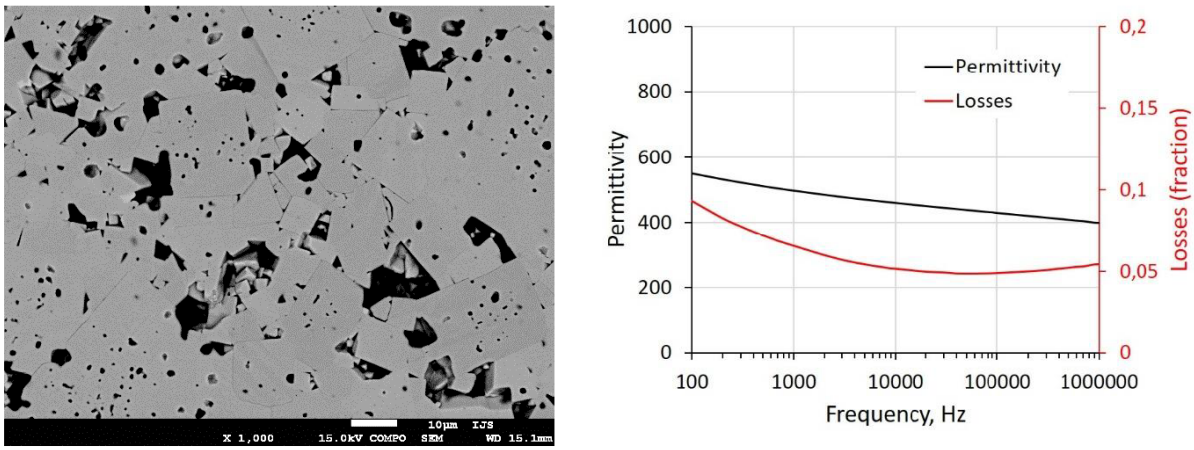

Figure S2: (a) Microstructure of conventionally sintered KNNSr sample at 1120 °C for 2h in oxygen, showing cube-shaped grains of up to 30 µm large with intragranular and intergranular porosity. (b) Dielectric permittivity and tanδ vs. frequency of the same sample.

Supplementary part 4

Polarization and strain evolution with electric field of two cold-sintered samples, first sintered at 676 MPa and the other sintered at 200 MPa. The 200 MPa sample appears much more lossy than the 676 MPa samples, which could be a result of leakage current – see discussion in the main manuscript.

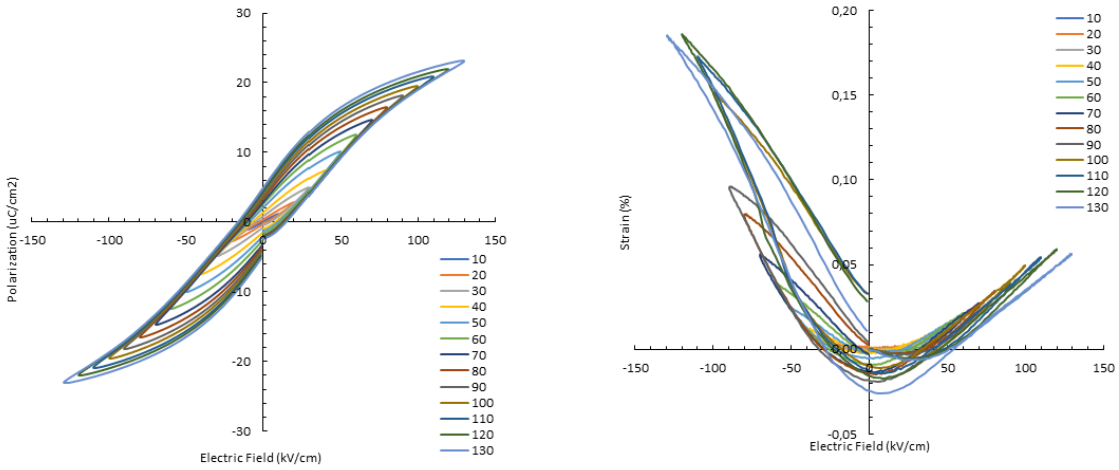

Figure S3 – The evolution of P-E (left plot) and S-E (right plot) loops. The legends indicate the value of applied electric field. The sample was cold-sintered at 300 °C under 676 MPa for 2 hours with 4.8 wt. % OH. Before measurement, the sample was annealed at 500 °C in O_2 for 1 hour and then dried at 120 °C in vacuum for 24 hours.

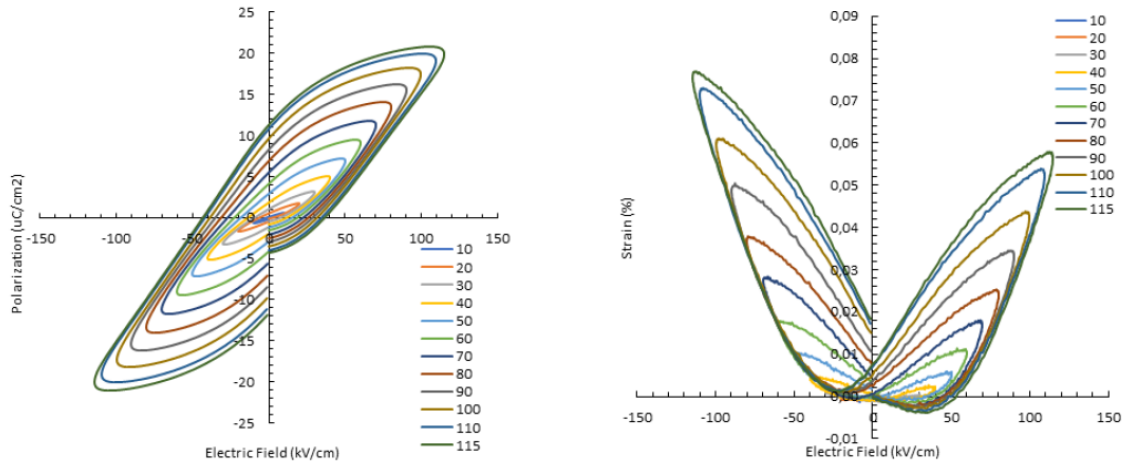

Figure S4 – The evolution of P-E (left plot) and S-E (right plot) loops. The legends indicate the value of applied electric field. The sample was cold-sintered at 300 °C under 200 MPa for 2 hours with 4.8 wt. % OH. Before measurement, the sample was annealed at 500 °C in O_2 for 2 hours and then dried at 120 °C in vacuum for 24 hours.

Chapter 4
Cold Sintering of Perovskite–Perovskite Particulate Composite Based on $K_{0.5}Na_{0.5}NbO_3$ and $BiFeO_3$

In this study, we aimed to obtain a dense perovskite-perovskite composite from BFO and KNN perovskites via the cold-sintering process, by applying similar conditions of sintering as to pure BFO and KNN in the previous two studies.

First, we cold sintered a homogeneous mixture of KNN and BFO powders with different BFO and KNN ratios. We found that the grains of KNN and BFO were homogeneously distributed in the microstructure, with good contacts between the phases. The composites had densities over 96 %.

Second, the measurements of functional properties revealed the contribution of each phase to the composite's overall performance. Specifically, we demonstrated that the KNN phase is primarily responsible for increasing the dielectric constant and remanent polarization in the composite. This influence is most noticeable at electric fields up to 150 kV/cm. However, at higher fields, the BFO phase contributes significantly to the ferroelectric properties, which was explained by the field strength sufficient for unpinning the domain walls and their contribution to the final response. Our findings further showed that BFO increases the dielectric breakdown strength but also makes the cold-sintered composite more electrically conductive and leaky.

These results demonstrate that CSP can be effectively employed to combine perovskite materials with drastically different chemical compositions and sintering temperatures without causing diffusion of one phase towards the other and the miscibility of phases, maximizing the benefits of each component.

This chapter addresses thesis objective 3.

Published in: Salmanov, S., Kuščer, D. and Otoničar, M., 2024. Cold Sintering of Perovskite–Perovskite Particu-late Composite Based on $K_{0.5}Na_{0.5}NbO_3$ and $BiFeO_3$. Informacije MIDEM, 54[3] (2024), 225-233.
https://doi.org/10.33180/InfMIDEM2024.306

My contribution: I cold-sintered all samples under different conditions, prepared samples for SEM and EDS analyses, measured densities, and performed the measurements of dielectric and ferroelectric properties. I also performed the necessary calculations, interpreted the results, and developed the manuscript together with co-authors.

Original scientific paper
https://doi.org/10.33180/InfMIDEM2024.306

Informacije MIDEM
Journal of Microelectronics, Electronic Components and Materials
Vol. 54, No. 3(2024), 225 – 233

Cold Sintering of Perovskite–Perovskite Particulate Composite Based on $K_{0.5}Na_{0.5}NbO_3$ and $BiFeO_3$

Samir Salmanov[1,2], Danjela Kuščer[1,2], Mojca Otoničar[1,2]

[1]Electronic Ceramics Department, Jožef Stefan Institute, Ljubljana, Slovenia
[2]Jožef Stefan International Postgraduate School, Ljubljana, Slovenia

Abstract: The cosintering of particulate composites often presents a challenge due to the conventionally high processing temperatures used. Inter-diffusion of species between two phases and their volatilization, formation of secondary phases, and cracking or delamination of ceramics are effects that hinder the coupling of functional properties and reduce the final responses of such composites. This is particularly relevant when producing perovskite–perovskite composites from phases that are conventionally sintered at different temperatures (Ts), such as $K_{0.5}Na_{0.5}NbO_3$ (KNN; Ts≈1100 °C) and $BiFeO_3$ (BFO; Ts≈800 °C). Obtaining high-quality KNN–BFO multifunctional composite was the goal of this study. We demonstrate herein that the low-temperature sintering technique known as the Cold Sintering Process (CSP) can be utilized for producing particulate perovskite–perovskite composites, specifically KNN–BFO. We show that cold-sintered KNN–BFO composites have a dense microstructure, good phase-to-phase contact, are crack-free and exhibit ferroelectric properties. Their dielectric and ferroelectric properties are strongly affected by the fraction of KNN, increasing polarization saturation, while BFO aids in increasing their dielectric breakdown strength.

Keywords: cold sintering process; ferroelectric; particulate composite; $BiFeO_3$; $K_{0.5}Na_{0.5}NbO_3$

Hladno sintranje prahov perovskitov na osnovi $K_{0.5}Na_{0.5}NbO_3$ in $BiFeO_3$

Izvleček: Sosintranje dveh različnih praškastih keramičnih materialov v kompozitne strukture predstavlja izziv, saj keramika zahteva pripravo pri visokih temperaturah. Pri teh pogojih, difuzija ionov med dvema fazama, sublimacija, tvorba sekundarnih faz ter nastanek razpok ali delaminacija keramike vplivajo na lastnosti kompozita in poslabšajo njegove funkcijske lastnosti. To je še posebej pomembno pri izdelavi kompozitov iz dveh perovskitnih faz, ki se običajno sintrajo pri različnih temperaturah (Ts). Tak primer so kompoziti na osnovi $K_{0.5}Na_{0.5}NbO_3$ (KNN; Ts≈1100 °C) in $BiFeO_3$ (BFO; Ts≈800 °C) feroelektričnih sestav, KNN-BFO, katerih pripravo in lastnosti obravnava ta študija. Dokazali smo, da je mogoče tehniko nizkotemperaturnega sintranja, znano kot postopek hladnega sintranja (CSP), uporabiti za izdelavo kompozitov iz prahov dveh različnih feroelektričnih perovskitnih materialov, KNN in BFO. Pokazali smo, da imajo hladno sintrani kompoziti gosto mikrostrukturo, dober stik med fazami, so brez razpok in izkazujejo feroelektrični odziv. Na povišanje dielektričnih in feroelektričnih lastnosti močno vpliva delež KNN v kompozitu, ki povečuje polarizacijsko nasičenost, medtem ko BFO pripomore k povečanju njihove dielektrične prebojne trdnosti.

Ključne besede: hladno sintranje; feroelektriki; kompozit; $BiFeO_3$; $K_{0.5}Na_{0.5}NbO_3$

** Corresponding Author's e-mail: samir.salmanov@ijs.si*

1 Introduction

Ferroelectric perovskites are widely used in a variety of electronic devices such as capacitors, sensors, actuators, and transducers [1]. Among environmentally friendly lead-free materials, $K_{0.5}Na_{0.5}NbO_3$ (KNN) is a suitable candidate to replace $Pb(Zr_{1-x}Tix)O_3$ (PZT) in piezoelectric applications, and $BiFeO_3$ (BFO) [2]–[4] is widely investigated and used for multiferroic coupling or high-temperature piezoelectric applications. Combination of the two functional materials in the form of a multiferroic composites with properties that can be fine-tuned by adjusting amounts of each individual

How to cite:
S. Salmanov et al., "Cold Sintering of Perovskite–Perovskite Particulate Composite Based on $K_{0.5}Na_{0.5}NbO_3$ and $BiFeO_3$", Inf. Midem-J. Microelectron. Electron. Compon. Mater., Vol. 54, No. 3(2024), pp. 225–233

S. Salmanov et al.; Informacije Midem, Vol. 54, No. 3(2024), 225 – 233

phase could be beneficial for use in electronic devices, integrated as a single multifunctional component [5].

However, processing of perovskite-perovskite particulate composites by a conventional cosintering route is challenging due to different sintering temperatures of materials of different composition, volatilization of elements and their diffusion coefficients. In the case of KNN and BFO ceramics, KNN densifies in a narrow temperature range at ~1100 °C, close to its melting point of 1140 °C [2], while BFO densifies at ~300 °C lower temperature of 800 °C. Above ~950 °C BFO decomposes into liquid phase and Fe-rich phase and is fully melted at 1100 °C [4], [6]–[8]. It was also reported that cosintering of KNN and $BaFe_{12}O_{19}$ at 1125 °C led to volatilization of alkalies, resulting in decreased relative density of the composite [9]. It was further demonstrated for $CoFe_2O_4$ (CFO) and PZT composite that Fe^{3+} can diffuse into PZT, and Ti^{4+} can diffuse into CFO already at 900–1000 °C [10]–[12]. This diffusion facilitates secondary phase formation, limiting functional-property coupling between the two phases, and can cause creation of oxygen vacancies, leading to enhanced conductivity of the composite [10]. In an attempt to limit such diffusion, in the case of cosintering of BFO and $BaTiO_3$ [13], as well as BFO and PZT [14], low sintering temperatures were used, but the microstructure was highly porous.

Beside the different sintering temperatures of the composite phases and with that the possible interdiffusion of species between the two phases during cosintering, forming a third solid-solution phase, producing composites is challenging also due to different thermal expansion coefficient (TEC) of individual phases. The latter may cause strains at the interfaces of different phases and microcracks [15], [16] during cooling of the composite from the processing temperature due to different shrinkage parameters of the lattices. The cracking effect due to different TEC of two composite phases is more evident in the case of a layered composite structure, e.g., cosintering CFO and PZT in a sandwiched structure resulted in cracks along the interface and delamination or the structure [17]. On the other hand, it was shown for CFO–PZT [18] and Co-doped BFO–PZT composite [12], as well as in the co-sintered BFO–$Ni_{0.5}Co_{0.5-x}Zn_xFe_2O_4$ composite [19] that interfacial strains influence the lattice distortions of individual phases, contributing to large magnetoelectric coupling. In the case of materials of our interest, BFO and KNN, BFO has TEC of 10.9 $x10^{-6}$ K^{-1} and 12.2$x10^{-6}$ K^{-1} for the temperature range 25–325 °C and 344–838 °C, respectively [20], while KNN has TEC of 2.96$x10^{-6}$ K^{-1}, 4.35$x10^{-6}$ K^{-1} and 7.52 $x10^{-6}$ K^{-1} for the temperature range 30–195 °C, 208–364 °C and 434–790 °C, respectively [21]. This implies that BFO will shrink almost twice more than KNN when cooling down from the sintering temperature, likely producing strains at the interfaces and/or cracks.

A way to severely limit thermal expansion/shrinkage, diffusion or volatilization of species during sintering of composites is to sinter at temperatures below 300 °C. Cold sintering process (CSP) is a sintering technique that allows densification of materials at temperatures even below 300 °C, under applied uniaxial pressure of a few hundreds of MPa and in the presence of a transient liquid phase, which facilitates material densification through a pressure-dissolution process [22]. The low processing temperature of the CSP provides opportunities for combining a variety of materials, i.e., ceramic with polymers or metals, as well as different types of oxides [23]–[27]. While different perovskites have been cold-sintered so far, including KNN-based compositions and BFO ceramics [28], there are no reports yet on cold sintering of perovskite-perovskite composites, which is a viable way to produce multifunctional components.

In this contribution we studied the processing of KNN–BFO perovskite-perovskite particulate composite with different ratios of phases, using the CSP. Based on our previous investigations on cold sintering of KNN [29], [30] and BFO [28], we utilized a eutectic mixture of NaOH and KOH as a transient liquid phase (TLP) to aid the sintering of the composite, which resulted in a homogeneous distribution of the two phases, no secondary phases formed at the grain boundaries, and a dense microstructure. The aim of our work is to illustrate that cold sintering can be successfully employed for combining two ferroelectric perovskite compositions to produce high-quality composites as multifunctional components.

2 Materials and methods

The initial powder compositions, $BiFeO_3$ with added 0.1 wt.% Co (named BFO hereafter), and $K_{0.5}Na_{0.5}NbO_3$ (KNN), were prepared via solid-state synthesis. Details on preparation can be found elsewhere (KNN powder was calcined at 850 °C) [31], [32]. Both powders were separately milled at 200 rpm for 0.5h (KNN) and 2h (BFO) after calcination to break the agglomerates. The mean particle of KNN was d_{50} = 0.50 µm and for BFO d_{50} = 1.39 µm. Different ratios of KNN and BFO powders were then mixed together in an agate mortar to produce (1-x)KNN–xBFO compositions with x= 0, 0.33, 0.50 and 0.66 and 1 (in weight fraction). The samples are denoted as: KNN, 33%BFO, 50%BFO, 66%BFO and BFO, respectively. Converting BFO weight % into volume %, the three compositions are 20%BFO, 35%BFO and

50%BFO, respectively. For each composition, 75 µl of NaOH-KOH aqueous equimolar mixture was added to 0.6 g of powders and manually mixed in an agate mortar. The NaOH-KOH solution was prepared by dissolving NaOH (molarity is 4.26 M) and KOH (molarity is 4.26 M) in water. The moist powders were put in the CSP instrument and pressed under 676 MPa uniaxial pressure (with a pressing rate of 13 MPa/minute) and heated to 300 °C (with heating and cooling rates of 2 K/min) and cold-sintered for 2 hours. The slow rates have previously been shown to produce reliable crack-free samples [33] and were chosen here for two reasons, one being better liquid/particle distribution in the green compact and the other being the polymorphic phase transition at about 170 °C for KNN which might cause large strains due to lattice volume changes and cracking of grains/pellet. After CSP, the obtained pellets with thickness ~1.8 mm and diameter of 8 mm were dried in vacuum drier at 80 °C overnight. Microstructure analysis of cold-sintered samples was performed on polished samples using a scanning electron microscope using backscattered electrons (SEM; JSM 7600 F, Jeol Ltd., Tokyo, Japan). Relative density of cold-sintered samples was calculated based on measured porosity from several SEM images. For dielectric and ferroelectric measurements, the samples were thinned to 0.15-0.25 mm, and gold-sputtered on both sides (using sputtering system 5Pascal, Italy). Dielectric properties were measured with an LCR meter (Hewlett Packard, Tokyo, Japan). Ferroelectric properties (polarization vs. electric field) were measured with a TF2000 analyzer (AixACCT Systems GmbH, Aachen, Germany) at a frequency of 100 Hz with a sinusoidal voltage waveform until their breakdown. Selected samples were annealed in O_2 flow at 500 °C for 2 hours, with 2 K/min heating and cooling rates for dielectric measurements.

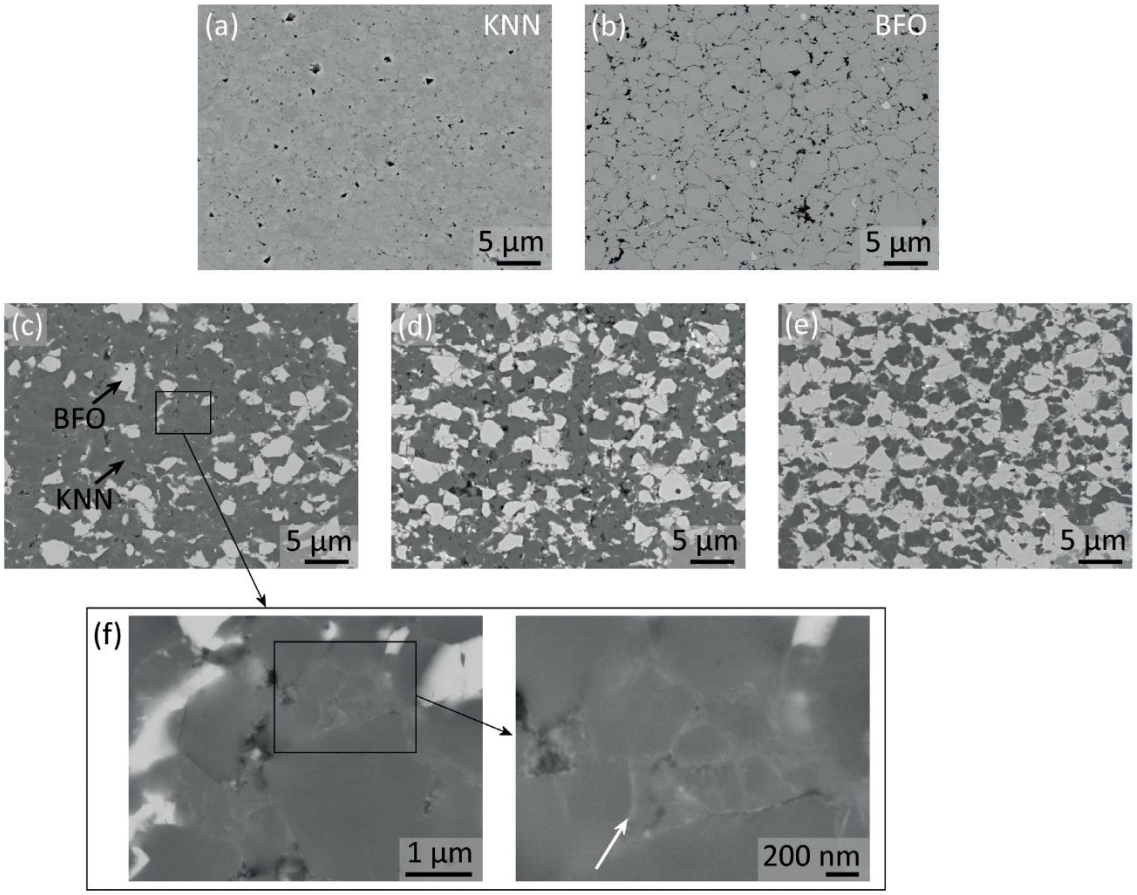

Figure 1: SEM images of ceramic samples cold sintered at 300 °C for 2 hours at 635 MPa with NaOH–KOH as a transient liquid phase: (a) KNN; (b) BFO; (c) 33%BFO; (d) 50%BFO and (e) 66%BFO (percentage given in wt.%). Light grey color of grains in the composites is BFO, and dark grey color of grains is KNN for (c), (d) and (e). Black spots are pores. (f) Enlarged area from 33%BFO composite in (c), showing grain-boundary contacts between KNN grains (white arrow in the right image).

S. Salmanov et al.; Informacije Midem, Vol. 54, No. 3(2024), 225 – 233

3 Results and discussion

The microstructures of cold-sintered KNN–BFO composites with compositions 33%BFO, 50%BFO and 66%BFO, as well as single-phase KNN and BFO for comparison, are presented in Figure 1. The average grain size of KNN is about 1 µm or less, while BFO has larger grains, ranging up to 5 µm. No secondary phases are observed at the grain boundaries in KNN and BFO from the cold sintering procedure (Figure 1a-b). KNN shows higher relative density compared to BFO, with estimated 98 % compared to 94 %, respectively. Such a difference could be related to several reasons, one being better particle packing in KNN due to smaller initial particles. On the other hand, higher density of cold-sintered KNN compared to BFO can also be explained by the different levels of solubility of each ceramic in the base solution and/or eutectic liquid phase. It was previously shown for KNN dipped in aqueous solution of NaOH that the concentration of Nb^{5+} ions starts to increase already at 50 °C [34], indicating its significant solubility. No studies were found for the solubility of BFO, however, it was shown that during its hydrothermal synthesis it was only possible to dissolve and precipitate BFO species at temperatures above 175-200 °C [35]. This may indicate that KNN is more soluble in the NaOH-KOH liquid phase compared to BFO, leading to higher densification levels of KNN during cold sintering. The third argument for better compaction of KNN could be its ability to significantly plastically deform with applied pressure that seems to exceed the yield strength of the material (e.g., for $KNbO_3$ crystal yield strength of 40 to 120 MPa was reported [36], [37]. Finally, the plastic deformation is realized through dislocation formation and lattice gliding [29], [30], [38], which may have been more efficient in KNN due to its lower density and/or weaker chemical bonding, resulting in a denser microstructure of KNN compared to BFO.

Microstructures of KNN–BFO composites (Figure 1c–e) show that KNN (dark grey phase) and BFO (bright grey phase) are homogeneously distributed, and the relative densities of 33%BFO, 50%BFO and 66%BFO, calculated from measured porosity from the microstructures, are ~96 %. Enlarged view of the 33%BFO composite in Figure 1f shows grain-boundary contacts, indicating good adhesion between the KNN grains, creating a matrix, with BFO grains well compacted between the sintered KNN grains.

These boundaries appear to be slightly curved, confirming the pressure-dissolution process [22] during

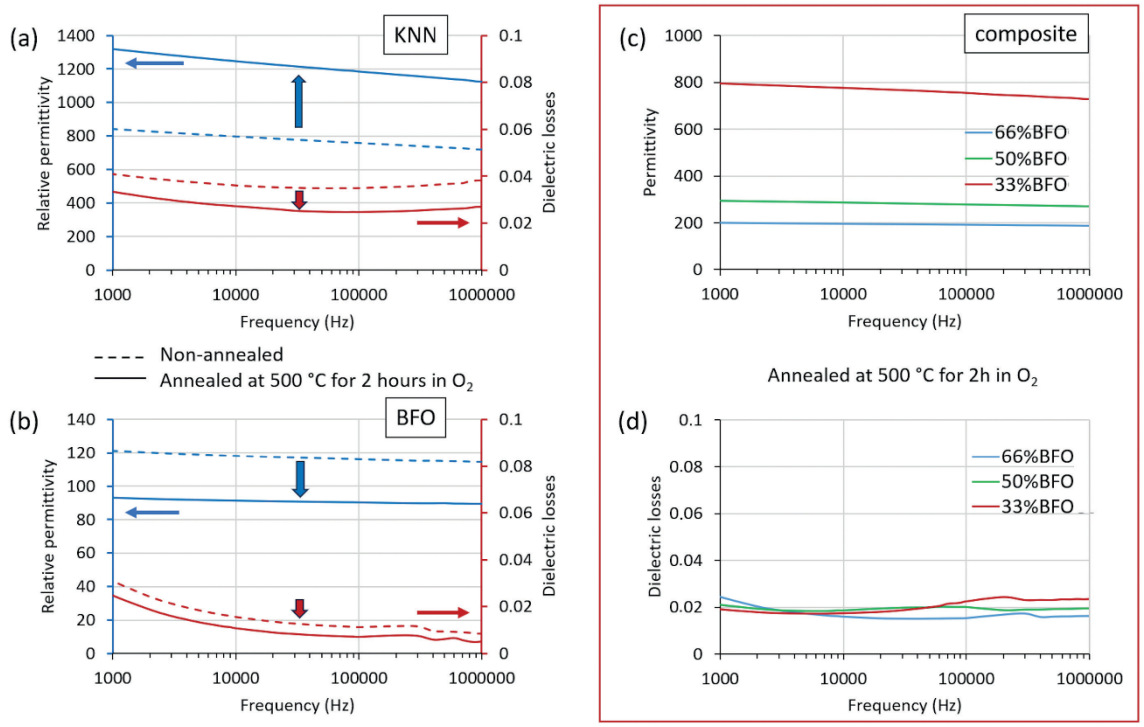

Figure 2: Comparison of dielectric permittivity and dielectric losses of as-prepared cold-sintered samples and samples annealed at 500 °C for 2 hours in O_2 (a) KNN and (b) BFO. (c) and (d) dielectric permittivity and losses of 33%BFO, 50%BFO and 66%BFO composites after annealing

cold sintering, but also appear lighter-grayish, which could indicate a Bi- or Nb-rich phase as a consequence of liquid-phase formation and precipitation of such a phase. The quantity of this phase, however, was too low to be identified by energy dispersive X-ray spectroscopy in SEM or X-ray diffraction. In 50%BFO, and especially in 66%BFO sample, contacts between BFO grains are observed that also show good contact and adhesion. No cracks are seen throughout the composites, which reflects good sintering and adhesion of grains, and minimal thermal expansion of the phases in the temperature range from sintering (300 °C) to room temperature.

The dielectric properties, presented in Figure 2, were measured on the as-prepared and dried cold-sintered KNN, BFO and composite samples, and after O_2 annealing. The as-prepared BFO exhibits the relative dielectric permittivity of ~120 and dielectric losses below 3% in a frequency range from 1 kHz to 1 MHz, and after annealing in O_2 no significant decrease in relative dielectric permittivity and dielectric losses is observed (Figure 2a). The cold-sintered KNN is characterized by a relative dielectric permittivity of ~800 and dielectric losses of 4% in a frequency range from 1 kHz to 1 MHz. However, after annealing in O_2, the dielectric permittivity increased by more than 50 %, while the dielectric losses decreased (Figure 2b). These results are consistent with previous data [30], [39]. The changes in dielectric properties after annealing in O_2 are believed to arise from the reoxidation of the perovskite and changes in the valence states of Nb atom, which was reduced from Nb^{5+} to Nb^{4+} during the CSP. For this reason, composites were also annealed in O_2.

The relative dielectric permittivity and dielectric losses of 33%BFO, 50%BFO and 66%BFO composites after annealing at 500 °C in O_2 are shown in Figure 2c and 2d, respectively. The 66%BFO composite exhibited relative dielectric permittivity of ~200, slightly higher than that of BFO. We can further follow a trend with increasing amount of KNN in the composites, resulting in an increase in the relative dielectric permittivity, with the value for the 33%BFO composite still lower than that of KNN. Especially notable is the difference in relative dielectric permittivity between 33%BFO and 50%BFO compared to the difference between 50%BFO and 33%BFO, which is minimal. This could be related to a critical amount of KNN in the composite. Since in 33%BFO there is only 20 vol. % of BFO, this suggests that the contribution to the relative dielectric permittivity of KNN dominates over BFO. On the other hand, the amount of BFO increases to 35 vol. % and 50 vol. % in 50%BFO and 66%BFO composites, respectively, increasing the contribution of BFO to the dielectric properties, decreasing the relative dielectric permittivity. Interestingly, the values of the dielectric losses of all the composites were similar in the studied frequency range, but slightly higher in the low-frequency range in 66%BFO, similar to pure BFO, which could indicate local conductivity due to defect states in the BFO phase (Figure 2d).

The P–E-loops at 150 kV/cm applied electric field of cold-sintered KNN and BFO and composites 33%BFO, 50%BFO and 66%BFO are shown in Figure 3a. The results show that the coercive field (E_c) and remanent polarization (P_r) values of the composites are between the values for KNN and BFO. 33%BFO and 50%BFO samples show a similar P_r value, while P_r of 66%BFO is smaller, which is in line with the value of the major constituent phase, BFO. The KNN loop shows polarization saturation reached at 150 kV/cm applied, with P_s=30 μC/cm^2. The P–E loop of BFO, however, remains flat at this field and only starts to open at an applied electrical field greater than 150 kV/cm (see inset in Figure 3a for the BFO loop at 200 kV/cm). This indicates defect states in the material that unpin the domains only at stronger fields applied. The effect of defects seems to be hindered in the case of composites with increasing KNN phase, increasing also the P_r value. On the other hand, dielectric breakdown strength seems to be strongly affected by the amount of BFO in the composite, increasing the maximum possible applied electric field (E_{max}) (Figure 3b). We note here that while we did not systematically measure the dielectric breakdown strength of these materials, we consistently observe for all cold-sintered perovskites that the samples withstand larger electrical fields applied without their dielectric breakdown. The final reached value of P_r of the composite seems to be affected by the strength of the grain-boundary contacts between the KNN grains (see enlarged view in Figure 1f), which are more frequent in the composite with larger KNN amount. The analysis of the evolution of P–E loops with gradually increasing electric field for composites (Figure 3c–e) shows that in 66%BFO at maximum applied field (see the loop at 170 kV/cm) the P–E loop starts to open and becomes more rounded. This indicates a major contribution to electrical properties from the BFO phase with unpinning of defects and increased conductivity [31]. Comparison of the functional properties of cold-sintered samples is summarized in Table 1.

4 Conclusions

We demonstrated that CSP can be effectively utilized for sintering of perovskite–perovskite particulate composites based on different ratios of KNN and BFO. Microstructure analysis revealed that the composites have a

S. Salmanov et al.; Informacije Midem, Vol. 54, No. 3(2024), 225 – 233

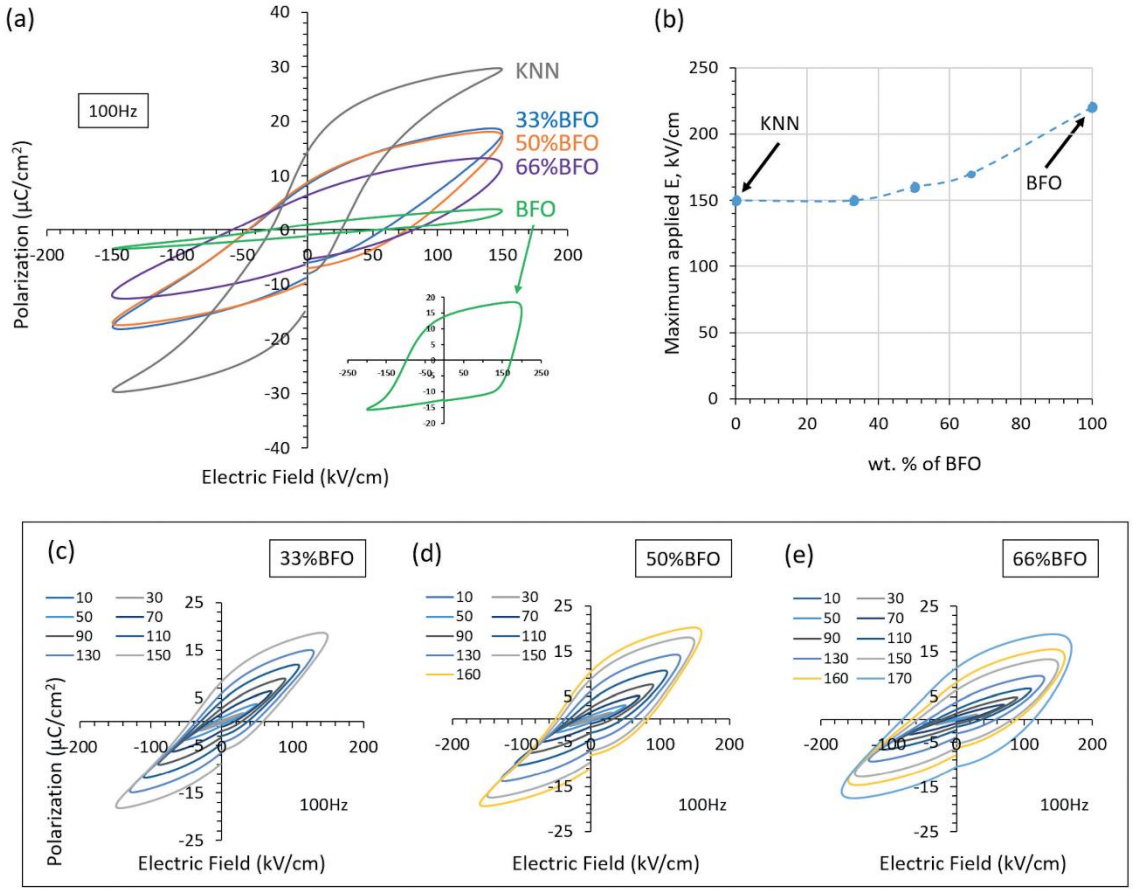

Figure 3: Comparison of ferroelectric properties cold-sintered KNN, BFO and composite ceramics after annealing 500 °C for 2 hours in O2. (a) Polarization–electric-field (P–E) loops at 150 kV/cm. Inset shows the P–E loop of BFO at 200 kV/cm. (b) Maximum applied electric field during measurement of P–E loops for all samples before breakdown. (c)–(e) Evolution of P–E loops with increasing E for (c) 33%BFO, (d) 50%BFO and (e) 66%BFO composites. All measurements were done at 100 Hz

dense structure and homogeneously distributed KNN and BFO grains. Moreover, the contact regions between KNN and BFO grains did not exhibit any cracks or large pores, nor significant secondary phases. After annealing in O_2, the dielectric losses were below 3% across the entire frequency range of 1 kHz to 1 MHz and the values of relative dielectric permittivity were in line with ~~KNN~~ amount of KNN, increasing with increasing KNN fraction. Nevertheless, the composite with 66 wt. % of BFO, where the contacts between KNN grains are rare, demonstrated approximately two times higher permittivity that single-phase cold-sintered BFO, and similar dielectric loss values. The composites showed decent ferroelectric properties and increasing polarization saturation with KNN content, while dielectric breakdown strength appeared higher with increasing BFO content. Remanent polarization is also enhanced by larger KNN fraction when up to 150 kV/cm field is applied, while

Table 1: Comparison of functional properties of cold-sintered samples

	Permittivity at 1kHz	Dielectric losses at 1kHz	Pr at 150 kV/cm	Pr at 200 kV/cm	Emax, kV/cm
KNN	~1300	~0.03	~14	-	150
33%BFO	~800	~0.02	~8	-	150
50%BFO	~300	~0.02	~8	-	160
66%BFO	~200	~0.02	~6	-	170
BFO	~100	~0.02	~2	~14	220

larger fraction of BFO in the composite allows to apply fields above 150 kV/cm, apparently increasing the breakdown strength of the composite.

5 Acknowledgments

The authors acknowledge the help of Brigita Kmet for KNN powder synthesis, Electronic Ceramics Department, Jožef Stefan Institute. The authors acknowledge the financial support of the Slovenian Research and Innovation Agency (core funding J2-2508, J2-50077, program P2-0105).

6 Conflict of Interest

The authors declare no conflict of interest.

7 References

1. G. H. Haertling, "Ferroelectric ceramics: history and technology," *J. Am. Ceram. Soc.*, vol. 82, no. 4, pp. 797–818, Apr. 1999, https://doi.org/10.1111/j.1151-2916.1999.tb01840.x.
2. B. Malič *et al.*, "Sintering of lead-free piezoelectric sodium potassium niobate ceramics," *Materials (Basel).*, vol. 8, no. 12, pp. 8117–8146, Dec. 2015, https://doi.org/10.3390/ma8125449.
3. K. Hui *et al.*, "KNN based high dielectric constant X9R ceramics with fine grain structure and energy storage ability," *J. Am. Ceram. Soc.*, vol. 104, no. 11, pp. 5815–5825, Nov. 2021, https://doi.org/10.1111/jace.17970.
4. T. Rojac *et al.*, "BiFeO 3 Ceramics: Processing, Electrical, and Electromechanical Properties," *J. Am. Ceram. Soc.*, vol. 97, no. 7, pp. 1993–2011, Jul. 2014, https://doi.org/10.1111/jace.12982.
5. N. Ortega, A. Kumar, J. F. Scott, and R. S. Katiyar, "Multifunctional magnetoelectric materials for device applications," *J. Phys. Condens. Matter*, vol. 27, no. 50, p. 504002, Dec. 2015, https://doi.org/10.1088/0953-8984/27/50/504002.
6. M. I. Morozov, N. A. Lomanova, and V. V. Gusarov, "Specific features of BiFeO3 formation in a mixture of bismuth(III) and iron(III) oxides," *Russ. J. Gen. Chem.*, vol. 73, no. 11, pp. 1676–1680, Nov. 2003, https://doi.org/10.1023/B:RUGC.0000018640.30953.70.
7. R. Palai *et al.*, "β phase and γ–β metal-insulator transition in multiferroic BiFeO3," *Phys. Rev. B*, vol. 77, no. 1, p. 014110, Jan. 2008, https://doi.org/10.1103/PhysRevB.77.014110.
8. M. S. Bernardo, "Synthesis, microstructure and properties of BiFeO3-based multiferroic materials: A review," *Boletín la Soc. Española Cerámica y Vidr.*, vol. 53, no. 1, pp. 1–14, Feb. 2014, https://doi.org/10.3989/cyv.12014.
9. P. Kasaeipoor Naeini, T. Delshad Chermahin, M. Shayegh Boroujeny, B. Ebadzadeh, M. Nilforoushan, and M. Abdollahi, "Study of dielectric properties of lead-free multiferroic KNN/22.5 BaFe12O19 composites," *Adv. Ceram. Prog.*, vol. 7, no. 3, pp. 23–28, 2021, https://doi.org/10.30501/ACP.2021.298611.1071.
10. S. Basu, K. R. Babu, and R. N. P. Choudhary, "Studies on the piezoelectric and magnetostrictive phase distribution in lead zirconate titanate–cobalt iron oxide composites," *Mater. Chem. Phys.*, vol. 132, no. 2–3, pp. 570–580, Feb. 2012, https://doi.org/10.1016/j.matchemphys.2011.11.071.
11. P. Jenus, D. Lisjak, D. Kuscer, D. Makovec, and M. Drofenik, "The low-temperature cosintering of cobalt ferrite and lead zirconate titanate ceramic composites," *J. Am. Ceram. Soc.*, vol. 97, no. 1, pp. 74–80, Jan. 2014, https://doi.org/10.1111/jace.12600.
12. A. Marzouki *et al.*, "New approach for designing bulk multiferroic composites made of two perovskite oxides with enhanced direct magnetoelectric coupling," *Scr. Mater.*, vol. 194, pp. 5–7, Mar. 2021, https://doi.org/10.1016/j.scriptamat.2020.113673.
13. M. Yao *et al.*, "Great multiferroic properties in BiFeO3/BaTiO3 system with composite-like structure," *Appl. Phys. Lett.*, vol. 122, no. 15, Apr. 2023, https://doi.org/10.1063/5.0139017.
14. M. Yao *et al.*, "Grain size and piezoelectric effect on magnetoelectric coupling in BFO/PZT perovskite-perovskite composites," *J. Alloys Compd.*, vol. 948, p. 169731, Jul. 2023, https://doi.org/10.1016/j.jallcom.2023.169731.
15. J. Chen, L. Hu, J. Deng, and X. Xing, "Negative thermal expansion in functional materials: controllable thermal expansion by chemical modifications," *Chem. Soc. Rev.*, vol. 44, no. 11, pp. 3522–3567, 2015, https://doi.org/10.1039/C4CS00461B.
16. T. C. Lu, J. Yang, Z. Suo, A. G. Evans, R. Hecht, and R. Mehrabian, "Matrix cracking in intermetallic composites caused by thermal expansion mismatch," *Acta Metall. Mater.*, vol. 39, no. 8, pp. 1883–1890, Aug. 1991, https://doi.org/10.1016/0956-7151(91)90157-V.
17. J. Zhou, H. He, Z. Shi, G. Liu, and C.-W. Nan, "Dielectric, magnetic, and magnetoelectric properties of laminated PbZr0.52Ti0.48O3/CoFe2O4 composite ceramics," *J. Appl. Phys.*, vol. 100, no. 9, Nov. 2006, https://doi.org/10.1063/1.2358191.

18. L. K. Pradhan, R. Pandey, R. Kumar, and M. Kar, "Lattice strain induced multiferroicity in PZT-CFO particulate composite," *J. Appl. Phys.*, vol. 123, no. 7, Feb. 2018, doi: 10.1063/1.5008607.
19. Z. Manzoor, A. Khalid, G. M. Mustafa, S. M. Ramay, S. Naseem, and S. Atiq, "Magnetoelectric coupling caused by strain mediation in hetero-structured spinel-perovskite multiferroic composites," *J. Magn. Magn. Mater.*, vol. 500, p. 166409, Apr. 2020, https://doi.org/10.1016/J.JMMM.2020.166409.
20. J. D. Bucci, B. K. Robertson, and W. J. James, "The precision determination of the lattice parameters and the coefficients of thermal expansion of BiFeO 3," *J. Appl. Crystallogr.*, vol. 5, no. 3, pp. 187–191, Jun. 1972, https://doi.org/10.1107/S0021889872009173.
21. B. Malič, H. Razpotnik, J. Koruza, S. Kokalj, J. Cilenšek, and M. Kosec, "Linear thermal expansion of lead-free piezoelectric K0.5Na0.5NbO3 ceramics in a wide temperature range," *J. Am. Ceram. Soc.*, vol. 94, no. 8, pp. 2273–2275, Aug. 2011, https://doi.org/10.1111/j.1551-2916.2011.04628.x.
22. A. Ndayishimiye, S. H. Bang, C. J. Spiers, and C. A. Randall, "Reassessing cold sintering in the framework of pressure solution theory," *J. Eur. Ceram. Soc.*, vol. 43, no. 1, pp. 1–13, Jan. 2023, https://doi.org/10.1016/JJEURCERAMSOC.2022.09.053.
23. Y. Ji *et al.*, "Cold sintered, temperature-stable CaSnSiO5-K2MoO4 composite microwave ceramics and its prototype microstrip patch antenna," *J. Eur. Ceram. Soc.*, vol. 41, no. 1, pp. 424–429, Jan. 2021, https://doi.org/10.1016/JJEURCERAMSOC.2020.08.053.
24. D. Wang *et al.*, "Direct Integration of Cold Sintered, Temperature-Stable Bi2Mo2O9-K2MoO4 Ceramics on Printed Circuit Boards for Satellite Navigation Antennas," *J. Eur. Ceram. Soc.*, vol. 40, no. 12, pp. 4029–4034, Sep. 2020, https://doi.org/10.1016/JJEURCERAMSOC.2020.04.025.
25. J. Guo, S. S. Berbano, H. Guo, A. L. Baker, M. T. Lanagan, and C. A. Randall, "Cold Sintering Process of Composites: Bridging the Processing Temperature Gap of Ceramic and Polymer Materials," *Adv. Funct. Mater.*, vol. 26, no. 39, pp. 7115–7121, 2016, https://doi.org/10.1002/adfm.201602489.
26. X. Zhao, J. Guo, K. Wang, T. Herisson De Beauvoir, B. Li, and C. A. Randall, "Introducing a ZnO-PTFE (Polymer) Nanocomposite Varistor via the Cold Sintering Process," *Adv. Eng. Mater.*, vol. 20, no. 7, p. 1700902, Jul. 2018, https://doi.org/10.1002/adem.201700902.
27. H. Zubairi, F. Hussain, S. Sheikh, A. A. Shaikh, D. Wang, and I. M. Reaney, "Comparative study of cold assisted and conventional sintering of (1-2x) K0.5Na0.5NbO3-xBaTiO3-xBiFeO3 multiferroic ceramics," *Mater. Sci. Eng. B*, vol. 296, p. 116632, Oct. 2023, https://doi.org/10.1016/j.mseb.2023.116632.
28. S. Salmanov *et al.*, "Impact of transient liquid phase on the cold sintering of multiferroic $BiFeO_3$," *UNDER Rev. J. - Eur. Ceram. Soc.*, 2024.
29. K. Tsuji, Z. Fan, S. H. Bang, S. Dursun, S. Trolier-McKinstry, and C. A. Randall, "Cold sintering of the ceramic potassium sodium niobate, (K0.5Na0.5) NbO3, and influences on piezoelectric properties," *J. Eur. Ceram. Soc.*, vol. 42, no. 1, pp. 105–111, Jan. 2022, https://doi.org/10.1016/j.jeurceramsoc.2021.10.002.
30. S. Salmanov *et al.*, "Structure and electrical properties of cold-sintered strontium-doped potassium sodium niobate," *J. Eur. Ceram. Soc.*, vol. 43, no. 16, pp. 7516–7523, Dec. 2023, https://doi.org/10.1016/JJEURCERAMSOC.2023.07.069.
31. M. Makarovic *et al.*, "Tailoring the electrical conductivity and hardening in BiFeO3 ceramics," *J. Eur. Ceram. Soc.*, vol. 40, no. 15, pp. 5483–5493, Dec. 2020, https://doi.org/10.1016/j.jeurceramsoc.2020.06.037.
32. J. Hreščak, B. Malič, J. Cilenšek, and A. Benčan, "Solid-state synthesis of undoped and Sr-doped K0.5Na0.5NbO3," *J. Therm. Anal. Calorim.*, vol. 127, no. 1, pp. 129–136, Jan. 2017, https://doi.org/10.1007/s10973-016-5615-3.
33. A. Jabr, J. Fanghanel, Z. Fan, R. Bermejo, and C. Randall, "The effect of liquid phase chemistry on the densification and strength of cold sintered ZnO," *J. Eur. Ceram. Soc.*, vol. 43, 2023, https://doi.org/10.1016/j.jeurceramsoc.2022.11.071.
34. A. Włódarkiewicz, M. E. Costa, and P. M. Vilarinho, "The dissolution of potassium sodium niobate (KNN) in aqueous media towards sustainable electroceramics sintering," *Mater. Des.*, vol. 233, p. 112169, Sep. 2023, https://doi.org/10.1016/J.MATDES.2023.112169.
35. S. H. Han *et al.*, "Synthesis and characterization of multiferroic BiFeO3 powders fabricated by hydrothermal method," *Ceram. Int.*, vol. 36, no. 4, pp. 1365–1372, May 2010, https://doi.org/10.1016/j.ceramint.2010.01.020.
36. A. F. Mark, M. Castillo-Rodriguez, and W. Sigle, "Unexpected plasticity of potassium niobate during compression between room temperature and 900°C," *J. Eur. Ceram. Soc.*, vol. 36, no. 11, pp. 2781–2793, Sep. 2016, https://doi.org/10.1016/j.jeurceramsoc.2016.04.032.
37. M. Höfling *et al.*, "Large plastic deformability of bulk ferroelectric KNbO3 single crystals," *J. Eur. Ceram. Soc.*, vol. 41, no. 7, pp. 4098–4107, Jul. 2021, https://doi.org/10.1016/JJEURCERAMSOC.2021.02.023.

38. K. Nakagawa, M. Iwasaki, Z. Fan, J. I. Roscow, and C. A. Randall, "The unusual case of plastic deformation and high dislocation densities with the cold sintering of the piezoelectric ceramic K0.5Na0.5NbO3," *J. Eur. Ceram. Soc.*, vol. 43, no. 9, pp. 4015–4020, Aug. 2023, https://doi.org/10.1016/J.JEURCERAMSOC.2023.02.057.
39. D. Kuscer *et al.*, "Evolution of phase composition and microstructure of sodium potassium niobate –based ceramic during pressure-less spark plasma sintering and post-annealing," *Ceram. Int.*, vol. 45, no. 8, pp. 10429–10437, 2019, https://doi.org/10.1016/j.ceramint.2019.02.102.

Arrived: 29. 04. 2024
Accepted: 06. 08. 2024

Chapter 5
Summary and Conclusions

This thesis describes the processing of ferroelectric ceramics, bismuth ferrite (BFO) and potassium sodium niobate (KNN), and BFO-KNN composite by the cold sintering process (CSP). CSP is an advanced sintering process that enables the processing of dense ceramics from micro- or nano-meter-sized ceramic powders at extremely low temperatures for ceramics, below 300 °C, through particle-fluid interface control and external pressure. CSP utilizes a transient liquid to achieve densification by a mediated pressure-dissolution-precipitation process. With the aim to obtain dense ferroelectric perovskite ceramics and composites with homogeneous microstructure, low electrical conductivity and high remanent polarization, we optimized the processing parameters: chemical composition and amount of the transient liquid phase used, strength of applied uniaxial pressure, temperature and time of sintering. The thesis consists of three parts, described in Chapters 2-4, while the following subchapters summarize the main findings for each study.

5.1 Cold Sintering of $BiFeO_3$

The first part of this dissertation examines the cold sintering of bismuth ferrite (BFO), focusing in particular on the formation of secondary phases by various additives used as sintering aids. It is the first successful demonstration of cold sintering of BFO without post-annealing. The most important results include the following:

The formation of secondary phases is highly dependent on the nature of the transient liquid phase compounds, with organic materials such as urea and ethanol leading to the formation of bismuth carbonate and iron oxide secondary phases. These phases form from the dissolved parts of BFO during the pressure-dissolution-precipitation process, suggesting that the source of bismuth and iron comes from this decomposition.

The use of organic-free additives, in particular an aqueous solution of sodium and potassium hydroxide in equimolar ratio, effectively prevents the formation of secondary phases via congruent dissolution of the matrix and extrusion of the dissolved species with the liquid out of the system. Cold sintering was possible with a minimal concentrations of 1-3 wt% of the NaOH/KOH mixture.

Observations showed etched grain boundaries between neighboring BFO grains, confirming pressure-dissolution as the main mechanism of sintering. The average relative density of the resulting ceramics was between 93-96 %, with cold sintering causing slight grain shrinkage rather than growth. No driving force for grain growth was detected.

Cold sintered BFO samples containing secondary phases exhibited high electrical conductivity, which decreased when these phases were removed and the density was increased.

Samples with higher levels of porosity were sensitive to moisture as hydroxide residues were trapped in their porous structure, so they had to be dried in a vacuum prior to dielectric and electrical property measurements.

The polarization-electric field (P-E) loops of the cold-sintered BFO showed a clearly suppressed polarization response up to about 150 kV/cm, with the hysteresis loops starting to open at higher fields. The suppression is attributed to small grain sizes and lattice dislocations that hinder the movement of the domain walls. Above the threshold, domain walls become unpinned and the extrinsic response becomes relevant, significantly increasing

the remanent polarization. The maximum applied electric field reached 220 kV/cm, exceeding the limits of conventionally sintered BFO (<150 kV/cm).

5.2 Cold Sintering of Strontium - Doped Potassium Sodium Niobate

The second part of the dissertation examines the cold sintering of KNN and focuses on how key processing parameters such as hydroxide solution concentration and uniaxial pressure affect the properties of the cold-sintered material. Key findings include the following:

An equimolar solution of NaOH and KOH facilitates cold sintering of KNN, with an optimal hydroxide concentration of 5 wt.%, leading to relative densities of ceramics above 96 %.

The applied uniaxial pressure has a major influence on pore size, dislocation formation and cracking. Higher pressures reduce porosity and eliminate poorly sintered areas but increase dislocations; at 676 MPa the unsintered areas are completely eliminated.

Microstructural analysis shows that the grain size corresponds to the original particle size, indicating no grain growth, with etched and curved grain surfaces suggesting an effective pressure-dissolution mechanism for densification.

Annealing at 500 °C in an O_2 atmosphere is required to reduce the electrical conductivity of the cold sintered KNN as the Nb ions are reduced from Nb^{5+} to Nb^{4+} during the sintering process.

The dielectric properties improve with higher relative density and higher pressure. The densest cold-sintered KNN has a dielectric constant twice as high as that of conventionally sintered KNN, whereby the dielectric losses are similarly high.

Temperature-dependent measurements of the dielectric constant show broader phase transition temperatures and strongly suppressed dielectric peaks in cold-sintered KNN, which can be attributed to the smaller grain size and the lattice stresses caused by applied pressure.

The difference in grain size between cold and conventionally sintered KNN affects the polarization-electric field (P-E) loops. The result is a lower remanent polarization in the cold sintered samples, but a higher maximum electric field of 170 kV/cm applied, indicating a higher dielectric breakdown strength of cold-sintered material.

The strain response to electric fields in cold sintered KNN shows an asymmetry between positive and negative part of electric field applied that is probably due to dislocation pinning. The strain difference is 2-3 times larger than in conventionally sintered KNN.

The calculated recoverable energy density and energy storage efficiency are 1.13 J/cm^3 and 47 %, respectively, highlighting the potential of these materials for energy storage applications and opportunities for further improvement.

Atomic level analysis shows numerous dislocations, supporting the assumption that pressure-dissolution creep contributes to densification.

5.3 Cold Sintering of $K_{0.5}Na_{0.5}NbO_3$ - $BiFeO_3$ Composite

The third part of this thesis investigated the viability of the cold sintering process for the production of KNN-BFO composites. Building on the knowledge of cold sintering the KNN and BFO perovskites individually, similar conditions were applied to produce the composites. The main conclusions here are:

The use of an equimolar KOH and NaOH solution facilitates the formation of dense KNN-BFO composites at mass ratios of 1:2, 1:1 and 2:1.

Microstructural analysis confirms that there is no diffusion between KNN and BFO grains, resulting in a 0-3 composite structure with the dominant phase forming a matrix.

The KNN phase mainly influences the dielectric properties, with a higher KNN content contributing to a higher dielectric constant, while the dielectric losses remain largely unaffected at all ratios of phases.

Higher KNN volume fractions also improve remanent polarization, while the BFO phase enhances the dielectric breakdown field. Conversely, samples with a higher BFO content exhibit a rounded shape tip of the P-E loop, which indicates a higher conductivity.

5.4 Future Work and Perspectives

Possible directions for future research related to the study of cold sintering process of perovskite electroceramics that I have identified are as follows:

Exploration of additives: investigation of additives that could serve as a transient liquid phase promoting the cold sintering was thus-far adopted from the hydrothermal synthesis. The aim is to identify more compounds that interact effectively with or dissolve the matrix material to promote sintering, bearing in mind that these additives could introduce undesirable secondary phases.

Thermally reactive compounds as sintering aids: This refers to compounds whose structure changes when heated to 300 °C. Hydrates in particular, which release water molecules when heated, could activate the grain surfaces and thus improve the cold sintering process.

Development of composites: Explore the use of perovskites with different compositions that are problematic for cold sintering and have different ferroelectric properties as fillers in combination with successfully cold-sintered perovskites. This approach could lead to the development of a network of sintered grains that allows better control of the functional properties of the composites.

Investigate dislocation hardening: Explore the effects of dislocation hardening by the cold sintering process in the context of tailoring the functional properties through extrinsic contribution to the response by adjusting the initial powders particle size and crystallinity and applied pressure during sintering.

References

[1] G. H. Haertling, "Ferroelectric ceramics: history and technology," *J. Am. Ceram. Soc.*, vol. 82, no. 4, pp. 797–818, Apr. 1999, doi: 10.1111/j.1151-2916.1999.tb01840.x.

[2] M. Biesuz, S. Grasso, and V. M. Sglavo, "What's new in ceramics sintering? A short report on the latest trends and future prospects," *Curr. Opin. Solid State Mater. Sci.*, vol. 24, no. 5, p. 100868, Oct. 2020, doi: 10.1016/j.cossms.2020.100868.

[3] M. T. Sebastian and H. Jantunen, "Low loss dielectric materials for LTCC applications: a review," *Int. Mater. Rev.*, vol. 53, no. 2, pp. 57–90, Mar. 2008, doi: 10.1179/174328008X277524.

[4] "EU-Directive 2002/95/EC. Restriction of the use of certain hazardous substances in electrical and electronic equipment (RoHS).," *Off. J. Eur. Union*, vol. 46(L37), pp. 19–23, 2003.

[5] "EU-Directive 2002/96/EC. Waste electrical and electronic equipment (WEEE)," *Off. J. Eur. Union*, vol. 46(L37), pp. 24–38, 2003.

[6] D. Damjanovic, "Ferroelectric, dielectric and piezoelectric properties of ferroelectric thin films and ceramics," *Reports Prog. Phys.*, vol. 61, no. 9, pp. 1267–1324, Sep. 1998, doi: 10.1088/0034-4885/61/9/002.

[7] M. Trainer, "Ferroelectrics and the Curie-Weiss law," *Eur. J. Phys.*, vol. 21, no. 5, pp. 459–464, Sep. 2000, doi: 10.1088/0143-0807/21/5/312.

[8] H. JAFFE, "Piezoelectric Ceramics," *J. Am. Ceram. Soc.*, vol. 41, no. 11, pp. 494–498, Nov. 1958, doi: 10.1111/j.1151-2916.1958.tb12903.x.

[9] D. M. Smyth, *The defect chemistry of metal oxides*. Oxford University Press, 2000.

[10] P. Potnis, N.-T. Tsou, and J. Huber, "A review of domain modelling and domain imaging techniques in ferroelectric crystals," *Materials (Basel).*, vol. 4, no. 2, pp. 417–447, Feb. 2011, doi: 10.3390/ma4020417.

[11] M. Makarovic *et al.*, "Tailoring the electrical conductivity and hardening in BiFeO3 ceramics," *J. Eur. Ceram. Soc.*, vol. 40, no. 15, pp. 5483–5493, Dec. 2020, doi: 10.1016/j.jeurceramsoc.2020.06.037.

[12] W. Cao and C. A. Randall, "Grain size and domain size relations in bulk ceramic ferroelectric materials," *J. Phys. Chem. Solids*, vol. 57, no. 10, pp. 1499–1505, Oct. 1996, doi: 10.1016/0022-3697(96)00019-4.

[13] A. Gruverman and A. Kholkin, "Nanoscale ferroelectrics: processing, characterization and future trends," *Reports Prog. Phys.*, vol. 69, no. 8, pp. 2443–2474, Aug. 2006, doi: 10.1088/0034-4885/69/8/R04.

[14] T. M. Shaw, S. Trolier-McKinstry, and P. C. McIntyre, "The properties of ferroelectric films at small dimensions," *Annu. Rev. Mater. Sci.*, vol. 30, no. 1, pp. 263–298, Aug. 2000, doi: 10.1146/annurev.matsci.30.1.263.

[15] Y. Su, H. Kang, Y. Wang, J. Li, and G. J. Weng, "Intrinsic versus extrinsic effects of the grain boundary on the properties of ferroelectric nanoceramics," *Phys. Rev. B*, vol. 95, no. 5, p. 054121, Feb. 2017, doi: 10.1103/PhysRevB.95.054121.

[16] X. L. Zhang, Z. X. Chen, L. E. Cross, and W. A. Schulze, "Dielectric and piezoelectric properties of modified lead titanate zirconate ceramics from 4.2 to 300 K," *J. Mater. Sci.*, vol. 18, no. 4, pp. 968–972, Apr. 1983, doi:

10.1007/BF00551962/METRICS.

[17] Q. M. Zhang, H. Wang, N. Kim, and L. E. Cross, "Direct evaluation of domain-wall and intrinsic contributions to the dielectric and piezoelectric response and their temperature dependence on lead zirconate-titanate ceramics," *J. Appl. Phys.*, vol. 75, no. 1, pp. 454–459, Jan. 1994, doi: 10.1063/1.355874.

[18] D. Damjanovic, M. Demartin, F. Chu, and N. Setter, "Practical consequences of the extrinsic contributions to the properties of piezoelectric sensors and actuators," *IEEE Int. Symp. Appl. Ferroelectr.*, vol. 1, pp. 251–257, 1996, doi: 10.1109/ISAF.1996.602744.

[19] G. Arlt, "The influence of microstructure on the properties of ferroelectric ceramics," *Ferroelectrics*, vol. 104, no. 1, pp. 217–227, Apr. 1990, doi: 10.1080/00150199008223825.

[20] T. Hoshina, Y. Kigoshi, S. Hatta, H. Takeda, and T. Tsurumi, "Domain contribution to dielectric properties of fine-grained BaTiO3 ceramics," *Jpn. J. Appl. Phys.*, vol. 48, no. 9, p. 09KC01, Sep. 2009, doi: 10.1143/JJAP.48.09KC01.

[21] D. Ghosh *et al.*, "Domain wall displacement is the origin of superior permittivity and piezoelectricity in BaTiO3 at intermediate grain sizes," *Adv. Funct. Mater.*, vol. 24, no. 7, pp. 885–896, Feb. 2014, doi: 10.1002/adfm.201301913.

[22] W. Känzig, "Space charge layer near the surface of a ferroelectric," *Phys. Rev.*, vol. 98, no. 2, pp. 549–550, Apr. 1955, doi: 10.1103/PhysRev.98.549.

[23] R. Bachmann and K. Bärner, "Stable suspensions of ferroelectric BaTiO3-particles," *Solid State Commun.*, vol. 68, no. 9, pp. 865–869, Dec. 1988, doi: 10.1016/0038-1098(88)91033-2.

[24] M. Schoijet, "On the anomalous crystallographic properties of small barium titanate particles," *Br. J. Appl. Phys.*, vol. 15, no. 6, pp. 719–723, Jun. 1964, doi: 10.1088/0508-3443/15/6/316.

[25] K. Ishikawa, T. Nomura, N. Okada, K. Takada, N. O. Nagaya Okada, and K. T. Kazumasa Takada, "Size effect on the phase transition in PbTiO3 Fine particles," *Jpn. J. Appl. Phys.*, vol. 35, no. 9S, p. 5196, Sep. 1996, doi: 10.1143/JJAP.35.5196.

[26] S. Chattopadhyay, P. Ayyub, V. R. Palkar, and M. Multani, "Size-induced diffuse phase transition in the nanocrystalline ferroelectric PbTiO3," *Phys. Rev. B*, vol. 52, no. 18, pp. 13177–13183, Nov. 1995, doi: 10.1103/PhysRevB.52.13177.

[27] M. H. Frey, Z. Xu, P. Han, and D. A. Payne, "The role of interfaces on an apparent grain size effect on the dielectric properties for ferroelectric barium titanate ceramics," *Ferroelectrics*, vol. 206–207, no. 1–4; 1–2, pp. 337–353, 1998, doi: 10.1080/00150199808009168.

[28] D. McCauley, R. E. Newnham, and C. A. Randall, "Intrinsic size effects in a barium titanate glass-ceramic," *J. Am. Ceram. Soc.*, vol. 81, no. 4, pp. 979–987, Apr. 1998, doi: 10.1111/J.1151-2916.1998.TB02435.X.

[29] K. Kinoshita and A. Yamaji, "Grain-size effects on dielectric properties in barium titanate ceramics," *J. Appl. Phys.*, vol. 47, no. 1, pp. 371–373, Jan. 1976, doi: 10.1063/1.322330.

[30] G. Arlt, D. Hennings, and G. de With, "Dielectric properties of fine-grained barium titanate ceramics," *J. Appl. Phys.*, vol. 58, no. 4, pp. 1619–1625, Aug. 1985, doi:

10.1063/1.336051.

[31] M. H. Frey, Z. Xu, P. Han, and D. A. Payne, "The role of interfaces on an apparent grain size effect on the dielectric properties for ferroelectric barium titanate ceramics," *Ferroelectrics*, vol. 206, no. 1, pp. 337–353, Feb. 1998, doi: 10.1080/00150199808009168.

[32] J. F. Ihlefeld, D. T. Harris, R. Keech, J. L. Jones, J. Maria, and S. Trolier-McKinstry, "Scaling effects in perovskite ferroelectrics: fundamental limits and process-structure-property relations," *J. Am. Ceram. Soc.*, vol. 99, no. 8, pp. 2537–2557, Aug. 2016, doi: 10.1111/jace.14387.

[33] J. E. Spanier *et al.*, "Ferroelectric phase transition in individual single-crystalline BaTiO3 nanowires," *Nano Lett.*, vol. 6, no. 4, pp. 735–739, Apr. 2006, doi: 10.1021/nl052538e.

[34] V. Buscaglia and C. A. Randall, "Size and scaling effects in barium titanate. An overview," *J. Eur. Ceram. Soc.*, vol. 40, no. 11, pp. 3744–3758, Sep. 2020, doi: 10.1016/j.jeurceramsoc.2020.01.021.

[35] M. Morozov, "Softening and hardening transitions in ferroelectric Pb(Zr,Ti)O3 ceramics," EPFL, 2005.

[36] M. Tyunina *et al.*, "Oxygen vacancy dipoles in strained epitaxial BaTi□O3 films," *Phys. Rev. Res.*, vol. 2, no. 2, p. 023056, Apr. 2020, doi: 10.1103/PhysRevResearch.2.023056.

[37] T. Rojac *et al.*, "Domain-wall conduction in ferroelectric BiFeO3 controlled by accumulation of charged defects," *Nat. Mater. 2016 163*, vol. 16, no. 3, pp. 322–327, Nov. 2016, doi: 10.1038/nmat4799.

[38] T. Rojac, H. Ursic, A. Bencan, B. Malic, and D. Damjanovic, "Mobile Domain Walls as a Bridge between Nanoscale Conductivity and Macroscopic Electromechanical Response," *Adv. Funct. Mater.*, vol. 25, no. 14, pp. 2099–2108, Apr. 2015, doi: 10.1002/ADFM.201402963.

[39] X. Qi, J. Dho, R. Tomov, M. G. Blamire, and J. L. MacManus-Driscoll, "Greatly reduced leakage current and conduction mechanism in aliovalent-ion-doped BiFeO3," *Appl. Phys. Lett.*, vol. 86, no. 6, pp. 1–3, Feb. 2005, doi: 10.1063/1.1862336/117600.

[40] S. J. Kim, S. H. Han, H. G. Kim, A. Y. Kim, J. S. Kim, and C. I. Cheon, "Multiferroic properties of Ti-doped BiFeO3 ceramics," *J. Korean Phys. Soc.*, vol. 56, no. 1, pp. 439–442, Jan. 2010, doi: 10.3938/JKPS.56.439.

[41] M. Kumar and K. L. Yadav, "Study of room temperature magnetoelectric coupling in Ti substituted bismuth ferrite system," *J. Appl. Phys.*, vol. 100, no. 7, p. 74111, Oct. 2006, doi: 10.1063/1.2349491/342845.

[42] N. Masó and A. R. West, "Electrical properties of Ca-doped BiFeO3 ceramics: From p-type semiconduction to oxide-ion conduction," *Chem. Mater.*, vol. 24, no. 11, pp. 2127–2132, Jun. 2012, doi: 10.1021/cm300683e.

[43] N. S. Bein *et al.*, "Electrochemical reduction of undoped and cobalt-doped BiFeO3 induced by water exposure: quantitative determination of reduction potentials and defect energy levels using photoelectron spectroscopy," *J. Phys. Chem. Lett.*, vol. 10, no. 22, pp. 7071–7076, Nov. 2019, doi: 10.1021/acs.jpclett.9b02706.

[44] R. W. Whitworth, "Charged dislocations in ionic crystals," *Adv. Phys.*, vol. 24, no. 2, pp. 203–304, Mar. 1975, doi: 10.1080/00018737500101401.

[45] K. W. Böer and U. W. Pohl, "Crystal defects," in *Semiconductor Physics*, Cham: Springer International Publishing, 2015, pp. 1–51.

[46] A. F. Mark, M. Castillo-Rodriguez, and W. Sigle, "Unexpected plasticity of potassium niobate during compression between room temperature and 900°C," *J. Eur. Ceram. Soc.*, vol. 36, no. 11, pp. 2781–2793, Sep. 2016, doi: 10.1016/j.jeurceramsoc.2016.04.032.

[47] P. Hirel, A. F. Mark, M. Castillo-Rodriguez, W. Sigle, M. Mrovec, and C. Elsässer, "Theoretical and experimental study of the core structure and mobility of dislocations and their influence on the ferroelectric polarization in perovskite KNbO3," *Phys. Rev. B*, vol. 92, no. 21, p. 214101, Dec. 2015, doi: 10.1103/PhysRevB.92.214101.

[48] J. Rösler, H. Harders, and M. Baeker, *Mechanical behaviour of engineering materials. Metals, ceramics, polymers, and composites*. Springer-Verlag Berlin Heidelberg, 2007.

[49] X. Fang *et al.*, "Room-temperature bulk plasticity and tunable dislocation densities in KTaO3," *J. Am. Ceram. Soc.*, vol. 107, no. 11, pp. 7054–7061, Nov. 2024, doi: 10.1111/jace.20040.

[50] Z.-C. Wang, C. Dupas-Bruzek, and S. Karato, "High temperature creep of an orthorhombic perovskite—YAlO3," *Phys. Earth Planet. Inter.*, vol. 110, no. 1–2, pp. 51–69, Jan. 1999, doi: 10.1016/S0031-9201(98)00130-7.

[51] A. J. Klomp, L. Porz, and K. Albe, "The nature and motion of deformation-induced dislocations in SrTiO3: Insights from atomistic simulations," *Acta Mater.*, vol. 242, p. 118404, Jan. 2023, doi: 10.1016/j.actamat.2022.118404.

[52] S. Y. Hu, Y. L. Li, and L. Q. Chen, "Effect of interfacial dislocations on ferroelectric phase stability and domain morphology in a thin film—a phase-field model," *J. Appl. Phys.*, vol. 94, no. 4, pp. 2542–2547, Aug. 2003, doi: 10.1063/1.1590416.

[53] M.-W. Chu *et al.*, "Impact of misfit dislocations on the polarization instability of epitaxial nanostructured ferroelectric perovskites," *Nat. Mater.*, vol. 3, no. 2, pp. 87–90, Feb. 2004, doi: 10.1038/nmat1057.

[54] Y. M. Chiang, D. P. Birnie, and W. D. Kingery, "Physical ceramics," J.Wiley, Ed. New York, 1997.

[55] R. M. German, *Sintering theory and practice*. Wiley, 1996.

[56] M. N. Rahaman, *Sintering of ceramics*. CRC press, 2007.

[57] R. M. German, P. Suri, and S. J. Park, "Review: Liquid phase sintering," *J. Mater. Sci.*, vol. 44, no. 1, pp. 1–39, Jan. 2009, doi: 10.1007/s10853-008-3008-0.

[58] R. Orrù, R. Licheri, A. M. Locci, A. Cincotti, and G. Cao, "Consolidation/synthesis of materials by electric current activated/assisted sintering," *Mater. Sci. Eng. R Reports*, vol. 63, no. 4–6, pp. 127–287, Feb. 2009, doi: 10.1016/j.mser.2008.09.003.

[59] D. F. K. HENNINGS, R. JANSSEN, and P. J. L. REYNEN, "Control of liquid-phase-enhanced discontinuous grain growth in barium titanate," *J. Am. Ceram. Soc.*, vol. 70, no. 1, pp. 23–27, Jan. 1987, doi: 10.1111/j.1151-2916.1987.tb04847.x.

[60] O. Guillon *et al.*, "Field-assisted sintering technology/spark plasma sintering:

Mechanisms, materials, and technology developments," *Adv. Eng. Mater.*, vol. 16, no. 7, pp. 830–849, 2014, doi: 10.1002/ADEM.201300409.

[61] R. K. M Suárez, A Fernández, JL Menéndez, R Torrecillas, HU Kessel, J Hennicke, "Challenges and opportunities for spark plasma sintering: a key technology for a new generation of materials," in *Sintering Applications*, Croatia: InTech, 2013, pp. 319–342.

[62] D. Kuscer *et al.*, "Evolution of phase composition and microstructure of sodium potassium niobate –based ceramic during pressure-less spark plasma sintering and post-annealing," *Ceram. Int.*, vol. 45, no. 8, pp. 10429–10437, 2019, doi: 10.1016/j.ceramint.2019.02.102.

[63] Jaffe B., Cook W.R., Jaffe H., *Piezoelectric ceramics*. London: Academic Press, 1971.

[64] J.-F. Li, K. Wang, F.-Y. Zhu, L.-Q. Cheng, and F.-Z. Yao, "(K,Na)NbO3 -based lead-free piezoceramics: fundamental aspects, processing technologies, and remaining challenges," *J. Am. Ceram. Soc.*, vol. 96, no. 12, pp. 3677–3696, Dec. 2013, doi: 10.1111/jace.12715.

[65] J. Tellier, B. Malic, B. Dkhil, D. Jenko, J. Cilensek, and M. Kosec, "Crystal structure and phase transitions of sodium potassium niobate perovskites," *Solid State Sci.*, vol. 11, no. 2, pp. 320–324, Feb. 2009, doi: 10.1016/j.solidstatesciences.2008.07.011.

[66] J. M. Moreau, C. Michel, R. Gerson, and W. J. James, "Ferroelectric BiFeO3 X-ray and neutron diffraction study," *J. Phys. Chem. Solids*, vol. 32, no. 6, pp. 1315–1320, Jan. 1971, doi: 10.1016/S0022-3697(71)80189-0.

[67] G. Catalan and J. F. Scott, "Physics and applications of bismuth ferrite," *Adv. Mater.*, vol. 21, no. 24, pp. 2463–2485, Jun. 2009, doi: 10.1002/adma.200802849.

[68] J. Wang *et al.*, "Epitaxial BiFeO3 multiferroic thin film heterostructures," *Science (80-.).*, vol. 299, no. 5613, pp. 1719–1722, Mar. 2003, doi: 10.1126/science.1080615.

[69] D. Lebeugle, D. Colson, A. Forget, and M. Viret, "Very large spontaneous electric polarization in BiFeO3 single crystals at room temperature and its evolution under cycling fields," *Appl. Phys. Lett.*, vol. 91, no. 2, p. 022907, Jul. 2007, doi: 10.1063/1.2753390.

[70] M. Kosec, B. Malič, A. Benčan, and T. Rojac, "KNN-based piezoelectric ceramics," in *Piezoelectric and Acoustic Materials for Transducer Applications*, Boston, MA: Springer US, 2008, pp. 81–102.

[71] B. Malič *et al.*, "Sintering of lead-free piezoelectric sodium potassium niobate ceramics," *Materials (Basel).*, vol. 8, no. 12, pp. 8117–8146, Dec. 2015, doi: 10.3390/ma8125449.

[72] A. N. Klein and D. Hotza, "Advanced ceramics with dense and fine-grained microstructures through fast firing," *Rev. Adv. Mater. Sci*, vol. 30, pp. 273–281, 2012.

[73] M. Bah, F. Giovannelli, F. Schoenstein, G. Feuillard, E. Le Clezio, and I. Monot-Laffez, "High electromechanical performance with spark plasma sintering of undoped K0.5Na0.5NbO3 ceramics," *Ceram. Int.*, vol. 40, no. 5, pp. 7473–7480, Jun. 2014, doi: 10.1016/j.ceramint.2013.12.097.

[74] R. Raj, M. Cologna, and J. S. C. Francis, "Influence of externally imposed and internally generated electrical fields on grain growth, diffusional creep, sintering and related phenomena in ceramics," *J. Am. Ceram. Soc.*, vol. 94, no. 7, pp. 1941–1965, Jul. 2011, doi: 10.1111/j.1551-2916.2011.04652.x.

[75] M. D. Maeder, D. Damjanovic, and N. Setter, "Lead free piezoelectric materials," *J. Electroceramics*, vol. 13, no. 1–3, pp. 385–392, Jul. 2004, doi: 10.1007/s10832-004-5130-y.

[76] B. Malic, J. Bernard, J. Holc, and M. Kosec, "Strontium doped K0.5Na0.5NbO3 based piezoceramics," *Ferroelectrics*, vol. 314, no. 1, pp. 149–156, Jun. 2005, doi: 10.1080/00150190590926373.

[77] J. Hreščak *et al.*, "Donor doping of K0.5Na0.5 NbO3 ceramics with strontium and its implications to grain size, phase composition and crystal structure," *J. Eur. Ceram. Soc.*, vol. 37, no. 5, pp. 2073–2082, May 2017, doi: 10.1016/j.jeurceramsoc.2016.12.053.

[78] J. G. Fisher and S.-J. L. Kang, "Microstructural changes in (K0.5Na0.5)NbO3 ceramics sintered in various atmosphere," *J. Eur. Ceram. Soc.*, vol. 29, no. 12, pp. 2581–2588, Sep. 2009, doi: 10.1016/j.jeurceramsoc.2009.02.006.

[79] T. Rojac *et al.*, "BiFeO 3 Ceramics: Processing, Electrical, and Electromechanical Properties," *J. Am. Ceram. Soc.*, vol. 97, no. 7, pp. 1993–2011, Jul. 2014, doi: 10.1111/jace.12982.

[80] M. I. Morozov, N. A. Lomanova, and V. V. Gusarov, "Specific features of BiFeO3 formation in a mixture of bismuth(III) and iron(III) oxides," *Russ. J. Gen. Chem.*, vol. 73, no. 11, pp. 1676–1680, Nov. 2003, doi: 10.1023/B:RUGC.0000018640.30953.70.

[81] M. Thrall, R. Freer, C. Martin, F. Azough, B. Patterson, and R. J. Cernik, "An in situ study of the formation of multiferroic bismuth ferrite using high resolution synchrotron X-ray powder diffraction," *J. Eur. Ceram. Soc.*, vol. 28, no. 13, pp. 2567–2572, Sep. 2008, doi: 10.1016/j.jeurceramsoc.2008.03.029.

[82] M. S. Bernardo, T. Jardiel, M. Peiteado, A. C. Caballero, and M. Villegas, "Reaction pathways in the solid state synthesis of multiferroic BiFeO3," *J. Eur. Ceram. Soc.*, vol. 31, no. 16, pp. 3047–3053, Dec. 2011, doi: 10.1016/j.jeurceramsoc.2011.03.018.

[83] A. Maître, M. François, and J. C. Gachon, "Experimental study of the Bi2O3-Fe2O3 pseudo-binary system," *J. Phase Equilibria Diffus.*, vol. 25, no. 1, pp. 59–67, Feb. 2004, doi: 10.1007/s11669-004-0171-0.

[84] R. Palai *et al.*, "β phase and γ-β metal-insulator transition in multiferroic BiFeO3," *Phys. Rev. B*, vol. 77, no. 1, p. 014110, Jan. 2008, doi: 10.1103/PhysRevB.77.014110.

[85] T. Rojac, M. Kosec, B. Budic, N. Setter, and D. Damjanovic, "Strong ferroelectric domain-wall pinning in BiFeO3 ceramics," *J. Appl. Phys.*, vol. 108, no. 7, Oct. 2010, doi: 10.1063/1.3490249.

[86] S.-H. Song, Q.-S. Zhu, L.-Q. Weng, and V. R. Mudinepalli, "A comparative study of dielectric, ferroelectric and magnetic properties of BiFeO3 multiferroic ceramics synthesized by conventional and spark plasma sintering techniques," *J. Eur. Ceram. Soc.*, vol. 35, no. 1, pp. 131–138, Jan. 2015, doi: 10.1016/j.jeurceramsoc.2014.08.016.

[87] Z.-H. Dai and Y. Akishige, "BiFeO3 ceramics synthesized by spark plasma

sintering," *Ceram. Int.*, vol. 38, pp. S403–S406, Jan. 2012, doi: 10.1016/j.ceramint.2011.05.020.

[88] N. Jeon, D. Rout, I. W. Kim, and S.-J. L. Kang, "Enhanced multiferroic properties of single-phase BiFeO3 bulk ceramics by Ho doping," *Appl. Phys. Lett.*, vol. 98, no. 7, Feb. 2011, doi: 10.1063/1.3552682.

[89] C. Ponzoni *et al.*, "Effect of low-temperature high-pressure sintering on BiFeO3 density, electrical magnetic and structural properties," *Phase Transitions*, vol. 86, no. 11, pp. 1104–1114, Nov. 2013, doi: 10.1080/01411594.2013.771738.

[90] T. Ibn-Mohammed *et al.*, "Decarbonising ceramic manufacturing: A techno-economic analysis of energy efficient sintering technologies in the functional materials sector," *J. Eur. Ceram. Soc.*, vol. 39, no. 16, pp. 5213–5235, Dec. 2019, doi: 10.1016/j.jeurceramsoc.2019.08.011.

[91] E. Y. Gutmanas and A. Lawley, "Cold sintering - a new powder consolidation process.," *Prog. Powder Metall.*, vol. 39, pp. 653–667, 1983, Accessed: Dec. 12, 2023. [Online]. Available: https://apps.dtic.mil/sti/citations/ADA131687.

[92] J. Guo *et al.*, "Cold Sintering: a paradigm shift for processing and integration of ceramics," *Angew. Chemie - Int. Ed.*, vol. 55, no. 38, pp. 11457–11461, 2016, doi: 10.1002/anie.201605443.

[93] F. Bouville and A. R. Studart, "Geologically-inspired strong bulk ceramics made with water at room temperature," *Nat. Commun.*, vol. 8, 2017, doi: 10.1038/ncomms14655.

[94] A. Ndayishimiye, S. H. Bang, C. J. Spiers, and C. A. Randall, "Reassessing cold sintering in the framework of pressure solution theory," *J. Eur. Ceram. Soc.*, vol. 43, no. 1, pp. 1–13, Jan. 2023, doi: 10.1016/J.JEURCERAMSOC.2022.09.053.

[95] P. K. Weyl, "Pressure solution and the force of crystallization: a phenomenological theory," *J. Geophys. Res.*, vol. 64, no. 11, pp. 2001–2025, Nov. 1959, doi: 10.1029/JZ064i011p02001.

[96] D. W. DURNEY, "Solution-transfer, an important geological deformation mechanism," *Nature*, vol. 235, no. 5337, pp. 315–317, Feb. 1972, doi: 10.1038/235315a0.

[97] E. H. Rutter, "The influence of interstitial water on the rheological behaviour of calcite rocks," *Tectonophysics*, vol. 14, no. 1, pp. 13–33, May 1972, doi: 10.1016/0040-1951(72)90003-0.

[98] P.-Y. F. Robin, "Pressure solution at grain-to-grain contacts," *Geochim. Cosmochim. Acta*, vol. 42, no. 9, pp. 1383–1389, Sep. 1978, doi: 10.1016/0016-7037(78)90043-1.

[99] J.-P. P. Gratier, D. K. Dysthe, and F. Renard, "The role of pressure solution creep in the ductility of the Earth's upper crust," in *Advances in Geophysics*, vol. 54, Elsevier, 2013, pp. 47–179.

[100] B. Jamtveit and P. Meakin, "Growth, dissolution and pattern Formation in geosystems," in *Growth, Dissolution and Pattern Formation in Geosystems*, Dordrecht: Springer Netherlands, 1999, pp. 1–19.

[101] A. Ndayishimiye *et al.*, "Roadmap for densification in cold sintering: Chemical pathways," 2020, doi: 10.1016/j.oceram.2020.100019.

[102] J. Hao *et al.*, "Grain size effect on microwave dielectric properties of Na2WO4 ceramics prepared by cold sintering process," *Ceram. Int.*, vol. 46, no. 17, pp. 27193–27198, Dec. 2020, doi: 10.1016/j.ceramint.2020.07.200.

[103] H. Guo, A. Baker, J. Guo, and C. A. Randall, "Cold Sintering Process: a novel technique for low-temperature ceramic processing of ferroelectrics," *J. Am. Ceram. Soc.*, vol. 99, no. 11, pp. 3489–3507, 2016, doi: 10.1111/jace.14554.

[104] A. Baker, H. Guo, J. Guo, C. Randall, and D. J. Green, "Utilizing the Cold Sintering Process for Flexible–Printable Electroceramic Device Fabrication," *J. Am. Ceram. Soc.*, vol. 99, no. 10, pp. 3202–3204, 2016, doi: 10.1111/jace.14467.

[105] K. Yamaguchi and S. Hashimoto, "Mechanism of densification of calcium carbonate by cold sintering process," *J. Eur. Ceram. Soc.*, vol. 42, no. 13, pp. 6048–6055, Oct. 2022, doi: 10.1016/j.jeurceramsoc.2022.06.034.

[106] X. Kang, R. Floyd, S. Lowum, D. Long, E. Dickey, and J.-P. Maria, "Cold sintering with dimethyl sulfoxide solutions for metal oxides," *J. Mater. Sci.*, vol. 54, no. 10, pp. 7438–7446, May 2019, doi: 10.1007/s10853-019-03410-1.

[107] S. Funahashi *et al.*, "Demonstration of the cold sintering process study for the densification and grain growth of ZnO ceramics," *J. Am. Ceram. Soc.*, vol. 100, no. 2, pp. 546–553, Feb. 2017, doi: 10.1111/jace.14617.

[108] X. Kang, R. Floyd, S. Lowum, M. Cabral, E. Dickey, and J. Maria, "Mechanism studies of hydrothermal cold sintering of zinc oxide at near room temperature," *J. Am. Ceram. Soc.*, vol. 102, no. 8, pp. 4459–4469, Aug. 2019, doi: 10.1111/jace.16340.

[109] H. Guo, J. Guo, A. Baker, and C. A. Randall, "Hydrothermal-Assisted Cold Sintering Process: A New Guidance for Low-Temperature Ceramic Sintering," *ACS Appl. Mater. Interfaces*, vol. 8, no. 32, pp. 20909–20915, 2016, doi: 10.1021/acsami.6b07481.

[110] H. Q. Huang, J. Tang, and J. Liu, "Preparation of Na 0.5 Bi 0.5 TiO 3 ceramics by hydrothermal-assisted cold sintering," *Ceram. Int.*, vol. 45, no. 6, pp. 6753–6758, 2019, doi: 10.1016/j.ceramint.2018.12.166.

[111] R. Boston, J. Guo, S. Funahashi, A. L. Baker, I. M. Reaney, and C. A. Randall, "Reactive intermediate phase cold sintering in strontium titanate," *RSC Adv.*, vol. 8, no. 36, pp. 20372–20378, 2018, doi: 10.1039/C8RA03072C.

[112] D. Wang, H. Guo, C. S. Morandi, C. A. Randall, and S. Trolier-McKinstry, "Cold sintering and electrical characterization of lead zirconate titanate piezoelectric ceramics," *APL Mater.*, vol. 6, no. 1, Jan. 2018, doi: 10.1063/1.5004420.

[113] W. Zhou *et al.*, "Cold sintering of perovskite-based mixed conducting membrane for oxygen separation," *AIChE J.*, Feb. 2024, doi: 10.1002/aic.18378.

[114] A. M. dos Santos, D. Thomazini, and M. V. Gelfuso, "Cold sintering and thermoelectric properties of Ca3Co4O9 ceramics," *Ceram. Int.*, vol. 46, no. 9, pp. 14064–14070, Jun. 2020, doi: 10.1016/j.ceramint.2020.02.206.

[115] S. Yang, C. Zuo, F. Du, L. Chen, W. Jie, and X. Wei, "Submicron Sr0.7Bi0.2TiO3 dielectric ceramics for energy storage via a two-step method aided by cold sintering process," *Mater. Des.*, vol. 225, p. 111447, Jan. 2023, doi: 10.1016/j.matdes.2022.111447.

[116] X. Tang, N. Luo, Q. Feng, X. Chen, and Y. Wei, "Microstructure and electrical

property of NaNbO3 ceramics prepared by cold sintering process assisted post-heat-treatment," *J. Alloys Compd.*, vol. 877, p. 160284, Oct. 2021, doi: 10.1016/j.jallcom.2021.160284.

[117] J. Ma *et al.*, "Composition, microstructure and electrical properties of K0.5Na0.5NbO3 ceramics fabricated by cold sintering assisted sintering," *J. Eur. Ceram. Soc.*, vol. 39, no. 4, pp. 986–993, Apr. 2019, doi: 10.1016/j.jeurceramsoc.2018.11.044.

[118] J.-J. Lan *et al.*, "Low-temperature synthesis of K0.5Na0.5NbO3 ceramics in a wide temperature window via cold-sintering assisted sintering method and enhanced electrical properties," *J. Eur. Ceram. Soc.*, vol. 43, no. 1, pp. 73–81, Jan. 2023, doi: 10.1016/j.jeurceramsoc.2022.09.041.

[119] J. Lan, X. Chen, M. Liu, L. Liu, and H. Lian, "K0.5Na0.5NbO3 ceramics fabricated by combining cold sintering with annealing in air atmosphere or low pO2 atmosphere," *J. Am. Ceram. Soc.*, vol. 106, no. 11, pp. 6826–6836, Nov. 2023, doi: 10.1111/jace.19316.

[120] L. Cong *et al.*, "Effect of dwell time on cold sintering assisted sintering based highly transparent 0.9K0.5Na0.5NbO3-0.1LiBiO3 ceramics," *J. Alloys Compd.*, vol. 826, p. 154249, Jun. 2020, doi: 10.1016/j.jallcom.2020.154249.

[121] N. Guo, H.-Z. Shen, and P. Shen, "One-step synthesis and densification of BaTiO3 by reactive cold sintering," *Scr. Mater.*, vol. 213, p. 114628, May 2022, doi: 10.1016/j.scriptamat.2022.114628.

[122] H.-Z. Shen, N. Guo, and P. Shen, "Synthesis and densification of BaZrO3 ceramics by reactive cold sintering of Ba(OH)2·8H2O-Zr(OH)4 powders," *J. Eur. Ceram. Soc.*, vol. 43, no. 2, pp. 392–400, Feb. 2023, doi: 10.1016/j.jeurceramsoc.2022.10.016.

[123] M. Kindelmann *et al.*, "Highly conductive grain boundaries in cold-sintered barium zirconate-based proton conductors," *J. Mater. Chem. A*, vol. 12, no. 7, pp. 3977–3988, 2024, doi: 10.1039/D3TA07076J.

[124] K. Tsuji *et al.*, "Single step densification of high permittivity BaTiO3 ceramics at 300 °C," *J. Eur. Ceram. Soc.*, vol. 40, no. 4, pp. 1280–1284, Apr. 2020, doi: 10.1016/j.jeurceramsoc.2019.12.022.

[125] G. J. Janz and R. P. T. Tomkins, "Physical properties data compilations relevant to energy storage," *Natl. Stand. Ref. Data Syst.*, 1981.

[126] Z. Shen *et al.*, "Ferroelectric ceramics with enhanced remnant polarization by ordered coalescence of nano-crystals," *J. Mater. Chem.*, vol. 22, no. 44, p. 23547, 2012, doi: 10.1039/c2jm32191b.

[127] M. B. Smith *et al.*, "Crystal Structure and the Paraelectric-to-Ferroelectric Phase Transition of Nanoscale BaTiO 3," *J. Am. Chem. Soc.*, vol. 130, no. 22, pp. 6955–6963, Jun. 2008, doi: 10.1021/ja0758436.

[128] Z. Fu, Y. Liu, B. Zhang, and A. Chang, "Highly dense 0.3CaCeNbWO8 -0.7LaMnO3 composite ceramics fabricated by cold sintering process," *J. Am. Ceram. Soc.*, vol. 103, no. 11, pp. 6586–6593, Nov. 2020, doi: 10.1111/jace.17353.

[129] H. Zubairi, F. Hussain, S. Sheikh, A. A. Shaikh, D. Wang, and I. M. Reaney, "Comparative study of cold assisted and conventional sintering of (1-2x) K0.5Na0.5NbO3-xBaTiO3-xBiFeO3 multiferroic ceramics," *Mater. Sci. Eng. B*, vol.

296, p. 116632, Oct. 2023, doi: 10.1016/j.mseb.2023.116632.

[130] L. Coutinho, R. G. Aredes, and E. Antonelli, "Cold sintering and electric characterization of ZnO-BaTiO3 composites," *Cerâmica*, vol. 67, no. 381, pp. 105–110, Mar. 2021, doi: 10.1590/0366-69132021673813061.

[131] P. Kasaeipoor Naeini, T. Delshad Chermahin, M. Shayegh Boroujeny, B. Ebadzadeh, M. Nilforoushan, and M. Abdollahi, "Study of dielectric properties of lead-free multiferroic KNN/22.5 BaFe12O19 composites," *Adv. Ceram. Prog.*, vol. 7, no. 3, pp. 23–28, 2021, doi: 10.30501/ACP.2021.298611.1071.

[132] S. Basu, K. R. Babu, and R. N. P. Choudhary, "Studies on the piezoelectric and magnetostrictive phase distribution in lead zirconate titanate–cobalt iron oxide composites," *Mater. Chem. Phys.*, vol. 132, no. 2–3, pp. 570–580, Feb. 2012, doi: 10.1016/j.matchemphys.2011.11.071.

[133] P. Jenus, D. Lisjak, D. Kuscer, D. Makovec, and M. Drofenik, "The low-temperature cosintering of cobalt ferrite and lead zirconate titanate ceramic composites," *J. Am. Ceram. Soc.*, vol. 97, no. 1, pp. 74–80, Jan. 2014, doi: 10.1111/jace.12600.

[134] A. Marzouki *et al.*, "New approach for designing bulk multiferroic composites made of two perovskite oxides with enhanced direct magnetoelectric coupling," *Scr. Mater.*, vol. 194, pp. 5–7, Mar. 2021, doi: 10.1016/j.scriptamat.2020.113673.

[135] L. K. Pradhan, R. Pandey, R. Kumar, and M. Kar, "Lattice strain induced multiferroicity in PZT-CFO particulate composite," *J. Appl. Phys.*, vol. 123, no. 7, Feb. 2018, doi: 10.1063/1.5008607.

[136] J. Zhou, H. He, Z. Shi, G. Liu, and C.-W. Nan, "Dielectric, magnetic, and magnetoelectric properties of laminated PbZr0.52Ti0.48O3CoFe2O4 composite ceramics," *J. Appl. Phys.*, vol. 100, no. 9, Nov. 2006, doi: 10.1063/1.2358191.

[137] Z. Manzoor, A. Khalid, G. M. Mustafa, S. M. Ramay, S. Naseem, and S. Atiq, "Magnetoelectric coupling caused by strain mediation in hetero-structured spinel-perovskite multiferroic composites," *J. Magn. Magn. Mater.*, vol. 500, p. 166409, Apr. 2020, doi: 10.1016/J.JMMM.2020.166409.

[138] J. Guo *et al.*, "Cold Sintering Process of Composites: Bridging the Processing Temperature Gap of Ceramic and Polymer Materials," *Adv. Funct. Mater.*, vol. 99, no. 39, pp. 3489–3507, 2016, doi: 10.1002/adfm.201602489.

[139] X. Zhao, J. Guo, K. Wang, T. Herisson De Beauvoir, B. Li, and C. A. Randall, "Introducing a ZnO–PTFE (polymer) nanocomposite varistor via the cold sintering process," *Adv. Eng. Mater.*, vol. 20, no. 7, Jul. 2018, doi: 10.1002/adem.201700902.

[140] J. Guo *et al.*, "Cold Sintering Process of Composites: Bridging the Processing Temperature Gap of Ceramic and Polymer Materials," *Adv. Funct. Mater.*, vol. 99, no. 39, pp. 3489–3507, Oct. 2016, doi: 10.1002/adfm.201602489.

[141] S. S. Berbano, J. Guo, H. Guo, M. T. Lanagan, and C. A. Randall, "Cold sintering process of Li1.5 Al0.5Ge1.5(PO4)3 solid electrolyte," *J. Am. Ceram. Soc.*, vol. 100, no. 5, pp. 2123–2135, May 2017, doi: 10.1111/jace.14727.

[142] J. Guo *et al.*, "Cold sintering Na2Mo2O7 ceramic with poly(ether imide) (PEI) polymer to realize high-performance composites and integrated multilayer circuits," *ACS Appl. Nano Mater.*, vol. 1, no. 8, pp. 3837–3844, Aug. 2018, doi: 10.1021/acsanm.8b00609.

[143] J. Guo *et al.*, "Recent Progress in Applications of the Cold Sintering Process for Ceramic–Polymer Composites," *Adv. Funct. Mater.*, vol. 28, no. 39, pp. 1–15, 2018, doi: 10.1002/adfm.201801724.

[144] A. Jabr, H. N. Jones, A. P. Argüelles, S. Trolier-McKinstry, C. Randall, and R. Bermejo, "Scaling up the cold sintering process of ceramics," *J. Eur. Ceram. Soc.*, vol. 43, no. 12, pp. 5319–5329, Sep. 2023, doi: 10.1016/j.jeurceramsoc.2023.04.061.

Bibliography

Scientific Articles Related to the Thesis

Samir Salmanov, Danjela Kuščer, Mojca Otoničar. Cold Sintering of Perovskite–Perovskite Particu-late Composite Based on K0. 5Na0. 5NbO3 and BiFeO3. Informacije MIDEM. 2024 Aug 26;54(3).

Samir Salmanov, Minghai Yao, Katarina Žiberna, Meryem Lachhab, Brahim Dkhil, Barbara Malič, Tadej Rojac, Danjela Kuščer, Mojca Otoničar. Impact of transient liquid phase on the cold sintering of multiferroic BiFeO3. Journal of the European Ceramic Society. 2025 Jan 1;45(1):116846.

Samir Salmanov, Maja Koblar, Brigita Kmet, Barbara Malič, Tadej Rojac, Danjela Kuščer, Mojca Otoničar. Structure and electrical properties of cold-sintered strontium-doped potassium sodium niobate. Journal of the European Ceramic Society. 2023 Dec 1;43(16):7516-23.

Other Scientific Articles

Minghai Yao, Long Cheng, Shenglan Hao, Samir Salmanov, Mojca Otoničar, Frédéric Mazaleyrat, Brahim Dkhil. Great multiferroic properties in BiFeO3/BaTiO3 system with composite-like structure. Applied Physics Letters. 2023 Apr 10;122(15).

Minghai Yao, Arij Marzouki, Shenglan Hao, Samir Salmanov, Mojca Otoničar, Vincent Loyau, Brahim Dkhil. Grain size and piezoelectric effect on magnetoelectric coupling in BFO/PZT perovskite-perovskite composites. Journal of Alloys and Compounds. 2023 Jul 5;948:169731.

Matthieu Fricaudet, Katarina Žiberna, Samir Salmanov, Jens Kreisel, Delong He, Brahim Dkhil, Tadej Rojac, Mojca Otoničar, Pierre-Eymeric Janolin, Andraž Bradeško. Multifunctional Properties of Polyvinylidene-Fluoride-Based Materials: From Energy Harvesting to Energy Storage. ACS Applied Electronic Materials. 2022 Nov 14;4(11):5429-36.

Mojca Otoničar, Andraž Bradeško, Samir Salmanov, C. C. Chung, Jacob L. Jones, Tadej Rojac. Effects of poling on the electrical and electromechanical response of PMN–PT relaxor ferroelectric ceramics. Open Ceramics. 2021 Sep 1;7:100140.

Arij Marzouki, Minghai Yao, Samir Salmanov, V. Loyau, V. Megriche, Brahim Dkhil, Mojca Otoničar. New approach for designing bulk multiferroic composites made of two perovskite oxides with enhanced direct magnetoelectric coupling. Scripta Materialia. 2021 Mar 15;194:113673.

Published Scientific Conference Contributions – Abstracts (Invited Lecture)

Mojca Otoničar, Samir Salmanov, Katarina Žiberna, Meryem Lachhab, Andreja Benčan, Tadej Rojac, Danjela Kuščer, "Pressure-dissolution-induced structural defects in ferroelectric perovskites", In: 20th DSL2024 : Barcelona, Spain, 24-28 June 2024

Mojca Otoničar, Samir Salmanov, Minghai Yao, Brahim Dkhil, Danjela Kuščer, Tadej Rojac, Clive A. Randall, "Influence of the cold sintering process on the microstructure and properties of perovskite ferroelectrics : BiFeO3 case study", In: ISAF 2022 : ISAF-PFM-ECAPD [joint conference] : June 27-July 1, 2022, Tours, France, Piscataway: IEEE = Institute of Electrical and Electronics Engineers

Mojca Otoničar, Andraž Bradeško, Samir Salmanov, Ching-Chang Chung, Alexandra Henriques, Jacob L. Jones, Tadej Rojac, "Poling-induced effects in Pb(Mg1/3Nb2/3O3−PbTiO3 ceramics", In: IEEE ISAF 2021 joint ISAF ISIF-PMF virtual Conference, IEEE International Symposium on Applications of Feeroelectric, (ISAF) [and] International Symposium on Integrated Functionalities, (ISIF) [and] Piezoresponse Force Microscopy Workshop, (PFM), M ay 16-21, 2021, Danvers: IEEE = Institute of Electrical and Electronics Engineers, 2020

Published Scientific Conference Contributions – Abstracts

Meryem Lachhab, Samir Salmanov, Katarina Žiberna, Maja Koblar, Brahim Dkhil, Mojca Otoničar, "Crystallographic defects in cold-sintered ferroelectric ceramics", In: 16th Jožef Stefan International Postgraduate School Students' Conference, 29th – 31st May, Piran, Slovenia: Book of abstracts: Two decades of discovery: advancing science and solutions, Alnilan Cristina Barros Lobato (ed.), et al., Ljubljana: Jožef Stefan Institute: Jožef Stefan International Postgraduate School, 2024

Maja Koblar, Katarina Žiberna, Samir Salmanov, Mojca Otoničar, Goran Dražić, Andreja Benčan, "TEM sample preparation of perovskite ferroelectrics using a combination of ion-beam-milling techniques", In: 5. slovensko posvetovanje mikroskopistov: knjiga povzetkov: 16.-17. maj 2024, Rogla, Blaž Belec (ed.), et al., 1. izd., Ljubljana: Slovensko društvo za mikroskopijo: = Slovene Society for Microscopy, 2024

Meryem Lachhab, Katarina Žiberna, Samir Salmanov, Maja Koblar, Mojca Otoničar, "Lattice strain analysis of cold-sintered perovskites", In: 5. slovensko posvetovanje mikroskopistov: knjiga povzetkov: 16.-17. maj 2024, Rogla, Blaž Belec (ed.), et al., 1. izd., Ljubljana: Slovensko društvo za mikroskopijo: = Slovene Society for Microscopy, 2024

Mojca Otoničar, Meryem Lachhab, Maja Koblar, Samir Salmanov, Katarina Žiberna, Goran Dražić, Andreja Benčan, "Electron-microscopy study of pressure-dissolution process in perovskites", In: 5. slovensko posvetovanje mikroskopistov: knjiga povzetkov: 16.-17. maj 2024, Rogla, Blaž Belec (ed.), et al., 1. izd., Ljubljana: Slovensko društvo za mikroskopijo: = Slovene Society for Microscopy, 2024

Mojca Otoničar, Meryem Lachhab, Samir Salmanov, Aadil Abass Shah, Katarina Žiberna, Andreja Benčan, Tadej Rojac, Danjela Kuščer, "Pressure-induced dissolution and plastic deformation of perovskite ferroelectric", In: IEEE UFFC-JS 2024: September 22 - 26, 2024, Taipei, Taiwan

Samir Salmanov, Danjela Kuščer, Mojca Otoničar, "Cold sintering of lead-free perovskites", In: 15th Jožef Stefan International Postgraduate School Students' Conference, 31st May - 2nd June 2023, Kamnik, Slovenia: Book of abstracts, Nina Kuzmić (ed.), et al., Ljubljana: Jožef Stefan Institute: Jožef Stefan International Postgraduate School, 2023

Samir Salmanov, Danjela Kuščer, Mojca Otoničar, et al., "Investigation of the influence of various parameters of (K0.5Na0.5)NbO3 cold sintering", In: XVIIIth ECerS conference : Conference & Exhibition of the European Ceramic Society : Lyon-France, 2/6 July 2023, Lyon: ECerS, 2023

Matthieu Fricaudet, Samir Salmanov, Maja Koblar, Tadej Rojac, Katarina Žiberna, Mojca Otoničar, Andraž Bradeško, et al., "Optimizing PVDF-based materials for multiphysic energy harvesting", In: XVIIIth ECerS conference: Conference & Exhibition of the European Ceramic Society: Lyon-France, 2/6 July 2023, Lyon: ECerS, 2023

Samir Salmanov, Maja Koblar, Danjela Kuščer, Tadej Rojac, Mojca Otoničar, "Pressure-induced defects in cold-sintered perovskites", In: 4. slovensko posvetovanje mikroskopistov: knjiga povzetkov: 12.-13. maj, Ankaran, Blaž Belec (ed.), et al., 1. izd., Ljubljana: Slovensko društvo za mikroskopijo, 2022

Samir Salmanov, Tadej Rojac, Danjela Kuščer, Mojca Otoničar, "Cold sintering as an alternative way to obtain lead-free ceramics", In: 57th International Conference on Microelectronics, Devices and Materials & The Workshop on Energy Harvesting: Materials and Applications: conference 2022: proceedings: September 14 - September 16 2022, Maribor, Slovenia, Tadej Rojac (ed.), Mojca Otoničar (ed.), Ljubljana: MIDEM - Society for Microelectronics, Electronic Components and Materials, 2022

Samir Salmanov, Minghai Yao, Katarina Žiberna, Tadej Rojac, Danjela Kuščer, Barbara Malič, Brahim Dkhil, Clive A. Randall, Mojca Otoničar, "Optimization of cold-sintering of bismuth ferrite", In: IEEE ISAF 2021 joint ISAF ISIF-PMF virtual Conference, IEEE International Symposium on Applications of Feeroelectric, (ISAF) [and] International Symposium on Integrated Functionalities, (ISIF) [and] Piezoresponse Force Microscopy Workshop, (PFM), M ay 16-21, 2021

Samir Salmanov, Danjela Kuščer, Mojca Otoničar, et al., "Cold sintering of Sr-modified (K0.5Na0.5)NbO3", In: ISAF 2022 : ISAF-PFM-ECAPD [joint conference] : June 27-July 1, 2022, Tours, France

Samir Salmanov, Mojca Otoničar, "Cold sintering: an efficient strategy to produce functional materials", In: Throughout knowledge towards a green new world: 13. Študentska konferenca Mednarodne podiplomske šole Jožefa Stefana in 15. dan mladih raziskovalcev (Konferenca KMBO), 27-28 maj 2021, Ljubljana, Slovenija: knjiga povzetkov = 13th Jožef Stefan International Postgraduate School Students' Conference and 15th Young Researchers' Day of Chemistry, material science, biochemistry and environment, (CMBE day), 27th-28th May 2021, online: book of abstracts, 13. študentska konferenca Mednarodne podiplomske šole Jožefa Stefana in 15. dan mladih raziskovalcev (Konferenca KMBO), 27-28 maj 2021, Ljubljana, Slovenija = 13th Jožef Stefan International Postgraduate School Students' Conference and 15th Young Researchers' Day, 27th-28th May 2021

Samir Salmanov, Danjela Kuščer, Barbara Malič, Tadej Rojac, Mojca Otoničar, "Cold sintering process for high-quality functional materials", In: Zbornik povzetkov = Book of abstracts: Slovenski kemijski dnevi 2021 = 27th Annual Meeting of the Slovenian Chemical Society: 22.-24. september 2021, Portorož, Portorose, Slovenija

Samir Salmanov, Minghai Yao, Katarina Žiberna, Brahim Dkhil, Tadej Rojac, Mojca Otoničar, "Dense bismuth ferrite ceramic using cold sintering process", In: Electroceramics XVII, International Conference: virtual Darmstadt: book of abstracts, 2020

Unpublished Scientific Conference Contributions

Samir Salmanov, Cold sintering of lead-free perovskites: 3rd YCN Workshop, Aveiro, 19th-21st April 2023

Samir Salmanov, Minghai Yao, Maja Koblar, Katarina Žiberna, Andreja Benčan, Brahim Dkhil, Andraž Kocjan, Barbara Malič, Tadej Rojac, Danjela Kuščer, Mojca Otoničar, Pressure-solution-induced features in selected cold-sintered perovskites: IEEE International Symposium on Applications of Ferroelectrics (ISAF), International Symposium on Integrated Functionalities (ISIF) & Piezoresponse Force Microscopy Workshop (PFM), ISAF-ISIF-PFM 2023, Cleveland, July 23-27, 2023

Biography

The author of this work was born on April 16, 1995, in Ganja, Azerbaijan. After graduating from Gymnasium in Naberezhnye Chelny, Russia, in 2013, he enrolled in a Chemical Engineering program at the Faculty of Chemical and Environmental Engineering, Gubkin Russian State University of Oil and Gas in Moscow, Russia. At this university, he obtained BSc (2017, Diploma with honors) and MSc (2019, Diploma with honors) degrees in Chemical Engineering. During his BSc and MSc studies, he was a member of the university's national chess team and actively participated in various tournaments. He also participated in various student Olympiads in chemistry and chemical engineering at the national and international levels, securing 1st to 3rd places. Throughout his six years of study in Moscow, he received various scholarships at the university and state levels.

Since November 2019, he has been employed at Jožef Stefan Institute, Electronic Ceramics Department. Simultaneously, he also enrolled in a PhD program (2019-present) in the Nanoscience and Nanotechnologies program at Jožef Stefan International Postgraduate School under the supervision of Asst. Prof. Dr. Mojca Otoničar and Assoc. Prof. Dr. Danjela Kuščer Hrovatin. His research area covers the processing and characterization of bulk functional ceramics, particularly focusing on the cold sintering of lead-free perovskites, $BiFeO_3$ (BFO), and $K_{0.5}Na_{0.5}NbO_3$ (KNN)-based materials.

During his PhD studies, he participated in various international conferences with poster presentations and/or oral talks. Additionally, he volunteered for the organization of the international conference ECerS2023 in July 2023 in Lyon, France, which was attended by approximately 1200 participants. As a member of the organizing committee and editorial board, he also co-organized the 15th Jožef Stefan International Postgraduate School Students' Conference (2023).